VILNIUS UNIVERSITY
THE INSTITUTE OF PHYSICS

Martynas Peckus

# SPATIAL LIGHT STRUCTURES IN LINEAR AND NONLINEAR MINI-RESONATORS

Doctoral dissertation

Physical sciences, Physics (02P)

Vilnius, 2009

The research was performed in 2003-2008 at Vilnius University

**Scientific supervisor:**

*Prof. Habil. Dr.* Valdas Sirutkaitis

(*Vilnius University*, Physical sciences, Physics - 02P)

**Consultant:**

*Prof. Habil. Dr.* Kęstutis Staliūnas

(*Institució Catalana de Reserca i Estudis Avançats (ICREA), Spain*, Physical sciences, Physics - 02P)

VILNIAUS UNIVERSITETAS
FIZIKOS INSTITUTAS

Martynas Peckus

# ERDVINIAI ŠVIESOS DARINIAI TIESINIUOSE IR NETIESINIUOSE MINI REZONATORIUOSE

Daktaro disertacija
Fiziniai mokslai, fizika (02P)

Vilnius, 2009

Disertacija rengta 2003-2008 Vilniaus universiteto Lazerinių tyrimų centre

**Mokslinis vadovas:**

*Prof. habil. dr.* Valdas Sirutkaitis
(*Vilniaus universitetas*, fiziniai mokslai, fizika - 02P)

**Konsultantas:**

*Prof. habil. dr.* Kęstutis Staliūnas
(*Katalonijos tyrimų ir aukštųjų studijų institutas (ICREA), Ispanija*, fiziniai mokslai, fizika - 02P)

## Contents

# Padėka

Pirmiausia noriu padėkoti vadovui prof. Valdui Sirutkaičiui už puikų vadovavimą, idėjas, kantrybę ir supratimą. Kartu noriu pasidžiaugti jo sukurtomis puikiomis darbo sąlygomis ir suburtu nuostabiu Lazerinio tyrimų centro kolektyvu.

Ypač esu dėkingas konsultantui prof. Kęstučiui Staliūnui už idėjas, kurios padėjo pagrindą šiam darbui. Taip pat už itin vaisingą bendradarbiavimą ir pagalbą sprendžiant teorinius klausimus.

Taip pat dėkoju kolegoms ir straipsnių bendrautoriams: prof. Valerijui Smilgevičiui, dr. Rimantui Grigoniui ir dr. Gintui Šlekiui už patarimus ir paramą sprendžiant iškilusius klausimus.

Dėkoju už malonų ir sėkmingą bendradarbiavimą Kauno technologijos universiteto, Fizikinės elektronikos instituto mokslininkams: dr. Mindaugui Andrulevičiui, Tomui Tamulevičiui ir dr. Astai Guobienei.

Džiaugiuosi galėdamas padėkoti studentams Robertui Rogalskiui ir Živilei Nižauskaitei už jų indėlį atliekant eksperimentinius tyrimus.

Esu labai dėkingas už redakcines pastabas ir sugaištą laiką Vytautui Petrauskui, Juliui Janušoniui, Giedrei Nainytei ir Zitai Manstavičienei.

Dėkoju kolegai Andriui Melninkaičiui už kūrybinį procesą skatinančių priemonių diegimą.

Dėkoju UAB Altechna ir Lietuvos Mokslo ir studijų fondui, parėmusiems mano vykdytus tyrimus.

Esu labai dėkingas prof. Algiui Petrui Piskarskui ir visiems Kvantinės elektronikos katedros darbuotojams už puikią lazerių fizikos mokyklą, kurioje man buvo didelė garbė studijuoti ir dirbti.

Nuoširdžiausiai dėkoju tėvams, draugams ir artimiems žmonėms už didelę kantrybę palaikymą ir supratimą šiuo ilgu ir nelengvu disertacijos rašymo metu.

*Ačiū Jums visiems!*

Martynas Peckus
Vilnius, 2009

## List of abbreviations

**1D** – one dimensional

**2D** – two dimensional

**3D** – three dimensional

**AFM –** atomic force microscopy

**AR –** anti-reflection

**CSHE -** complex Swift-Hohenberg equation

**D4WM -** degenerate four-wave mixing

**DOPO -** degenerate optical parametric oscillators

**EM –** electromagnetic

**FDTD –** finite difference time-domain

**HR –** high reflectivity

**NC -** nonlinear crystal

**OPE -** order parameter equation

**OPO -** optical parametric oscillators

**PhC –** photonic crystal

**SEM -** scanning electron microscope

**SHE -** Swift-Hohenberg equation

**SHG -** second harmonic generation

**SPOPO -** synchronously pumped degenerate optical parametric oscillators

**TE-** transverse electric

**TM –** transverse magnetic

# Introduction

## Motivation

The interest on the pattern formation in optical resonator is essentially twofold. First, the broad aperture optical resonator is a transverse pattern forming system – the one of many patterns forming system of the Nature. The spontaneous pattern formation, the spontaneous emergence of the spatial order from the randomness, is a fascinating subject which always interested the philosophers and scientists over the centuries. Why the spatial symmetries break, why the entropy decreases, why something regular emerges from irregular noise? The Nature in fact is patterns of patterns, and unveiling the secret of the pattern formation allows us to understand better the Nature. Patterns are encountered in almost every field of science – the laser physics is no exception. Therefore the studying of patterns in nonlinear optics, helps us to understand the pattern formation in general, thus it is of a fundamental significance. It is a tool to understand the pattern formation in general.

Another reason for studying the pattern formation in nonlinear optical resonators is the practical one – the hope of their possible applications in digital and analog image processing. The light in lasers, being fast, and simultaneously being well controllable by external means offers a good possibility for efficient applications (image and object recognition with the optical "neuron networks", creation of logic gates with the cavity solitons and vortices: some references). From the application point of view the compact optical systems, like mini- or micro nonlinear resonators are of extreme interest. Just imagine the mini optical pattern processing device in a small photo camera, or in a chip.

Although the theory of the pattern formation (in general, as well as in lasers) has been advanced strongly during the last decades, the experimental progress in optics is clearly lying behind. In spite of recent attempts [1-3] the pattern formation in mini and in micro resonators is still in a very initial stage.

Typically the technological limitations were a most serious obstacle preventing the experimental studies of pattern formation in mini and micro – resonators.

Presently the advent of the recent micro- and nano technologies is also rapidly accelerating the progress in the field of the pattern formation in micro resonators. The appearance of new, artificial materials, both linear and nonlinear, gives a hope on in the quick progress of this field. Nonlinear materials allow the low threshold lasing or low threshold soliton and nonlinear pattern formation. The spatially modulated materials (so called photonic crystals) on the other hand allow the modifying of the temporal and spatial characteristics of light (appearance of the band gaps in frequency domain, self collimation, super refraction in propagation domain, references). Therefore there appears a lot of space for the engineering of mini-resonators, with different nonlinear, and different diffraction properties. On the one hand allow finally to realize experimentally the theoretically predicted patterns, like solitons, rolls, and similar. On the other hand, it leads to novel phenomena absent in the conventional pattern forming theory (like hyperbolic patterns, sub diffractive solitons). Building such nonlinear micro-devices, understanding the behavior of light there, experimenting with them, discovering the new phenomena specific in such devices, are mayor challenges in the field of optical pattern formation in general, and in particulary in this doctoral dissertation.

The initial task of the dissertation was to demonstrate the pattern formation in miniresonators, which simultaneously are: 1) nonlinear and, 2) with the manipulated diffraction. The nonlinear character of patterns is achieved by putting a nonlinear (Kerr, $\chi^2$, amplifying) material inside of the resonator. The manipulation of diffraction is achieved by placing a material with the spatially modulated refraction index (Photonic crystal) inside of the resonator. The initial purpose of the dissertation work was to observe some exotic nonlinear patterns in such diffraction-manipulated resonator, like those predicted at that time (hyperbolic patterns [4]).

However, during the years of work, it comes out, that these two ingradients (the nonlinearity, and the index modulation) of the micro resonators, even taken separately, lead to a lot of different novel effects. It comes out, that even the observation of elementary nonlinear patterns (rolls) in parametric miniresonators was never done before, and its observation brought us to novel effects (like the experimental proof of 1/f noises of rolls, like the spatial tunability of the generated beams in micro-OPO). In this way these observations in nonlinear resonator WITHOUT the modulation of index were sufficiently challenging and novel. On the other hand – the linear miniresonator with photonic crystal inside also showed itself as a novel and completely unexplored device, investigation of which lead to discovery of novel effects, like sub diffractive patterns, spatial filtering hyperbolic patterns). Therefore the Photonic crystal resonators WITHOUT the nonlinearity has shown itself sufficiently challenging and novel.

## Main objectives

1. To demonstrate optical parametrical generation in monolithic broad aperture mini or micro cavities. To investigate transverse light patterns formation in mini-cavity OPO. To develop a model describing the system.

2. To obtain experimentally the previously theoretically predicted nonlinear light structures in degenerate optical parametrical resonators.

3. To build up and investigate experimentally and theoretically pattern formation in plane-mirror Fabry-Perot resonators filled by **two** and **three** dimensional photonic crystals

## Scientific novelty

1. Emission in monolithic mini-cavity OPO based on BBO type I crystal, pumped by nanosecond pulses was demonstrated experimentally for the first time. It was found, that OPO emission in a monolithic mini-cavity is conical and multiconical and emission direction can be controlled by changing the mini-cavity orientation, by temperature changes or by laser frequency change. This phenomenon was well explained by developed phenomenological model.
2. Stripe (roll) patterns in broad aperture plane mirror mini-cavities DOPOs was demonstrated experimentally for the first time. Stabilization of the stripes pattern was achieved by a week injection at sub-harmonic frequency. Absence of the intrinsic locking-to-degeneracy mechanism for the spatially dependent systems was highlighted. Temporal 1/f – like spectra of the stripe pattern DOPO emission was demonstrated experimentally in qualitative accordance with the theories of the noise-spectra in the spatially extended systems.
3. Plane-mirror Fabry-Pérot resonators with the intracavity modulation of refraction index, i.e., the resonators containing one longitudinal period of the photonic crystal were proposed and realized for the first time.
4. Calculation method, based on the scattering matrix theory, was developed for study and prediction of photonic crystal resonators diffraction properties. Analysis predicted that diffraction properties of photonic crystal resonators can be manipulated, resulting in sub- and superdiffractive dynamics of light in the resonator.
5. Basic properties of photonic crystal were demonstrated experimentally: hyperbolic shape transmission patterns in case of 1D modulation of the mirror surfaces, and square shape patterns in case of 2D modulation of the mirror surfaces.

## Practical significance

First purpose of this work was to demonstrate experimentally pattern forming phenomena in nonlinear resonators, i.e. broad aperture, plane mirrors OPOs. At that time a significant number of theoretical works in this field was already published. Most of them were without experimental approve due to a high OPO threshold and relatively low cavity coatings damage threshold. Experiments of this thesis, carries first successful results in this field. Conical and multi-conical OPO emission of monolithic cavity, stripe (roll) patterns formation with a presence of weak seed injection and 1/f-like temporal spectrum were demonstrated. These results first of all are fundamentally interesting and extend the knowledge about pattern formation of doubly resonant, mini-cavity OPOs. However, some results of OPO experiments can be also practically interesting. OPO emission direction can be controlled changing the mini-cavity orientation, temperature or laser frequency.

Second part of this thesis contains new theoretical and experimental results on intracavity photonic crystal devices, a topic which is expected to become more and more important in the future. Photonic crystal resonator is a new type device, which is obtained by using a Fabry-Perot resonator filled with a photonic crystal. Spatial dispersion of this resonator can be manipulated resulting in sub- and super-diffractive dynamics. Results show, that PhC resonator can be used as alternative device for beam shaping or filtering. As it is shown, PhC resonators have a very close relation with bulk PhC crystal spatial dispersion properties, especially diffraction less light propagation in the PhC media. Moreover, the results are highly relevant to all physicists working on pattern formation in optical systems.

As a future prospective those two parts of the thesis might be conducted together creating a new line of nonlinear PhC resonators.

## Thesis statements

1. Directions of signal and idler waves in a monolithic mini-cavity type I optical parametrical oscillator (OPO) depends on the cavity optical axes orientation with respect to the pump beam (in phase matching and perpendicular direction) and on cavity detuning to laser frequency and in general can be described as conical and multiconical emission.
2. The stabilization of stripe (or roll-) patterns in large Fresnel nuber ($N > 100$) plane-mirror mini-cavity degenerate optical parametric oscillator can be achieved by a week seed injection at subharmonic frequency. Temporal spectra of the stripe pattern DOPO emission is 1/f – like noise spectra.
3. Plane-mirror Fabry-Pérot resonators filled with a single period of photonic crystal (PhC) is a new type of PhC resonators with a PhC-like spatial properties. PhC resonators can be conveniently realized by adding periodical refraction index modulation on a resonator mirror surfaces (i.e. fabricating 1D or 2D phase diffraction grating)
4. Diffraction properties of photonic crystal resonators can be decribed as subdiffractive and superdiffractive dynamics of light in the PhC resonator. PhC resonators in case of 1D modulation of the mirror surfaces has a hyperbolic angular transmission profiles and in case of 2D modulation of the mirror surfaces - square shape angular transmission profiles.
5. The developed calculation method, based on the scattering matrix theory, enables to study and predict diffraction properties of photonic crystal resonators.

## Validation of thesis results

The main results of this thesis were published in the following scientific journals: *Optics Communications* (1 article), *Optics Letters* (1 article), *Physical Review* A (2 articles), *Proceedings of SPIE* (1 article), *Lithuanian Journal of Physics* (1 article)

Thesis results were also presented in 8 international conferences.

## Personal input of the author

Author contributions and responsibilities consist of the most part of experimental work, technical solutions and results preparation for publications, also part of numerical analysis and theoretical result comparison with experiments.

The main coauthors of the work described in this thesis were Prof. *V. Sirutkaitis* and Prof. *K. Staliūnas*.

Professor *Valdas Sirutkaitis* created good and friendly conditions for ongoing research. He also participated in formulation of tasks and discussions.

Professor *Kęstutis Staliūnas* is the author of most ideas and theory presented in the articles and in this thesis as well.

Prof. *Valerijus Smilgevičius*, dr. *Rimantas Grigonis* and dr.*Gintas Šlekys* contributed with consultations on OPO experiment set up development and provided with some instruments and crystals. Prof. *Mark Saffman* participated in discussion on OPO experimental results ant theoretical interpretation.

Students *Valdemaras Rukavičius* and *Živilė Nižauskaitė* participated in OPO experimets with seed injection. *Robertas Rogalskis* did some photonic crystal resonators research experiments, especialy in single modulated mirror experiments.

Dr. *Mindaugas Andrulevičius*, dr. *Asta Guobienė* and *Tomas Tamulevičius* developed modulated mirrors for PhC resonators in Kaunas University of Technology, Institute of Physical Electronics.

Dr. *Vygandas Jaru*tis made valulable contribution to Lithuanian State Science and Studies Foundation suported PhC Resontors Research project coordination.

## List of publications

[A1] M. Peckus, K. Staliunas, M. Saffman, G. Slekys, V. Sirutkaitis, V..Smilgevicius, and R. Grigonis, Multiconical emission of a monolithic mini-cavity optical parametric oscillator, Opt. Commun. **251**(1-3), 165-171 (2005).

[A2] M. Peckus, K. Staliunas, M. Saffman, G. Slekys, V. Sirutkaitis, V. Smilgevicius, and R. Grigonis, Multiconical transverse patterns of monolithic mini-cavity optical parametric oscillator, Lithuanian J. Phys. **45**(81-87), (2005).

[A3] M. Peckus, K. Staliunas, V. Smilgevicius, G. Slekys, V. Rukavicius, and V. Sirutkaitis, Transverse patterns of mini-cavity optical parametric oscillator with seed injection, Proc. SPIE **6596**, 659606 (2006).

[A4] M. Peckus, K. Staliunas, Z. Nizauskaite, and V. Sirutkaitis Stripe patterns in degenerate optical parametric oscillators, Opt. Lett. **32**, 3014-3016 (2007).

[A5] K. Staliunas, M. Peckus, and V. Sirutkaitis, Sub- and superdiffractive resonators with intracavity photonic crystals, Phys. Rev. A **76**, 051803(R) (2007).

[A6] M. Peckus, R. Rogalskis, M. Andrulevicius, T. Tamulevicius, A. Guobiene, V. Jarutis, V. Sirutkaitis, and K. Staliunas, Resonators with manipulated diffraction due to two- and three dimensional intracavity photonic crystals, Phys. Rev. A **79**, 033806 (2009).

## List of conferences

1. M. Peckus, K. Staliunas, M. Saffman, G. Slekys, V. Sirutkaitis, V. Smilgevicius, and R. Grigonis, *Multiconical emission of micro-cavity optical parametric oscillator,* International Workshop On Optical Parametric Processes And Periodical Structures, Vilnius, 26-29 September, 2004.

2. M. Peckus, K. Staliunas, M. Saffman, G. Slekys, V. Sirutkaitis, V. Smilgevicius, and R. Grigonis *Multiconical emission of micro-cavity optical parametric oscillator,* XVI Lithuanian-Belarussion seminar „Lasers and optical nonlinearity“, Vilnius, 27-29 October 2004.

3. M. Peckus, K. Staliunas, M. Saffman, G. Slekys, V. Sirutkaitis, V. Smilgevicius, and R. Grigonis, *Multiconical transverse patterns of monolithic mini-cavity optical parametric oscillator*, CLEO/EQEC-2005, Munich, 12-17 June 2005.

4. M. Peckus, K. Staliunas, M. Saffman, G. Slekys, V. Sirutkaitis, V. Smilgevicius, and R. Grigonis, *Multiconical transverse patterns of monolithic mini-cavity optical parametric oscillator*, IQEC/CLEO-PR 2005, Tokyo, 11-15 July 2005.

5. M. Peckus, K. Staliunas, V. Sirutkaitis, V. Smilgevicius and G. Slekys, *Transverse patterns of monolithic mini-cavity optical parametric oscillator*, LOYS 2006, St. Petersburg, Russia, 26-30 June 2006 (WeS2-P06).

6. M. Peckus, K. Staliunas, V. Smilgevicius, G. Slekys, V. Rukavicius, and V. Sirutkaitis *Multi-conical transverse patterns of monolithic mini-cavity optical parametric oscillator*, AOMD-5, Vilnius, 27-30 August 2006 (oral).

7. M. Peckus, K. Staliunas, M. Andrulevicius, T. Tamulevicius, and R. Rogalskis, *Diffraction manipulated resonators with intracavity photonic crystals*, Advanced Materials and Technologies, Palanga, Lithuania, 27-31August 2008.

8. M. Peckus, R. Rogalskis, M. Andrulevicius, T. Tamulevicius, A. Guobiene, V. Sirutkaitis, and K. Staliunas, *Diffraction manipulated resonators with intracavity photonic crystals*, CLEO/Europe-EQEC, Munich, 14-19 June 2009.

## Other presentations:

9. M. Peckus, T. Balciunas, J. Duda, and V. Vaicaitis, *Fabrication of volume phase gratings in fused silica using ultra-short laser pulses*, Advanced Materials and Technologies Palanga, Lithuania, 27-31 August, 2006.

10. E. Gaizauskas, V. Vaicaitis, V. Kudriasov, M. Peckus, T. Balciunas, and V. Sirutkaitis, *Fabrication of refractive index graitings in optical glasses by the filamentary propagation of femtosecond laser pulses*, Boulder Damage Symposium XXXVIII, Boulder, Colorado USA, 25-27 September 2006.

# 1. Transverse light patterns in nonlinear optical resonators

## 1.1 Dissipative patterns in nature

Many different pattern-forming systems are known to exist in the Nature, also in controllable laboratory experiments. A common feature of pattern forming systems is their openness, or dissipativity; this is why the spontaneously appearing patterns are also called by “dissipative patterns“ [5]. Openness also means, that a system is out of the thermal equilibrium, in contrary to conservative systems, where no patterns spontaneously appear, but instead the energy equipartition occurs, leading to most symmetrical, maximum entropy states.

Formation of rolls and hexagons in Rayleigh-Benard convection [6] is a seminal example of patterns formation in controllable laboratory experiment. Self-sustained oscillations in chemical reactions illustrate the symmetry breaking of space and time [7]. These elementary laboratory patterns and elementary evolution processes (the transients) can be considered as building bricks of more complicated patterns, and more complicated evolution processes observed in the nature. One can consider the complicated patterns in the nature as elementary patterns multiply nested within the other elementary patterns.

Some universal pattern formation principles are now understood and mathematically described. It is known, that the necessary condition for the occurrence of Turing patterns is the existence of unstable modes with nonzero characteristic spatial (temporal) scale of modulation [8]. The responsible physical mechanisms can be different: well known is the mechanism of “local activation and lateral inhibition“ being at the root for patterns in many biological and chemical systems [9]. The other universal mechanism is also known to be responsible for the appearance of patterns in parametrically excited (Faraday type [10]) systems: when the system is (parametrically) excited at a frequency different than its internal resonance frequency [11].

Turing mechanism can be considered as a primary stage of pattern formation. The next stage would mean the secondary instabilities of ideal Turing patterns. Some universal principles are also known governing the pattern formation in this second stage: the ideal Turing patterns can show Eckhause, Zig-zag, or other instabilities, or defects, universally described e.g. by means of amplitude and phase equations [12].

### 1.2 Transverse patterns in nonlinear resonators

A brief review of transverse patterns formation in nonlinear optical resonators is given in this section. According to [13] order parameter equations derived for different systems makes it possible to distinguish several large groups of nonlinear resonators:

1) laser-like nonlinear resonators, such as lasers of class A and C, photorefractive oscillators, and nondegenerate optical parametric oscillators. They are described by complex Swift-Hohenberg equation, and show the optical vortices as the basic localized structures, and tilted waves and square vortex lattices as the basic extended patterns.

2) resonators with squeezed phase, such as degenerate optical parametric oscillators, and degenerate four wave mixers. They are described by real Swift-Hohenberg equation, and show the phase domains and phase solitons as basic localized structures, and stripes and hexagons as basic extended patterns.

3) lasers with slow population inversion (class-B lasers). They can not be described by single order parameter equation, but at least by two coupled equations. Their basic features are self-sustained dynamics, in particular the "restless vortex".

4) subcritical nonlinear resonators, such as lasers with intracavity saturable absorbers, or optical parametric oscillators with detuned pump. They show bistability, and as consequence of that - they support bistable spatial solitons.

### 1.2.1. Order parameter equations

One possibility to study the patterns in nonlinear optical systems (or in nonlinear distributed systems in general) is based on corresponding microscopic models. The exact microscopic models contain "all information" about the system, and their solution can give absolutely precise results. However, solution of microscopic equations is often related with difficulties: the microscopic equations (usually a system of coupled nonlinear partial differential equations) are too complicated to obtain analytical results. The numerical study is often complicated too: different field components (e.g. the light field, polarization, and population inversion in lasers) may have very different relaxation rates. This leads to different time scales, which makes numerical calculations time consuming. A natural way to solve the above difficulties is to simplify the microscopic model as much as possible. Such a simplified equation (or sometimes an equation system) is called the Order Parameter Equation (OPE). OPEs simplify analytical and numerical treatment, as described above, since the OPEs are structurally more simpler than the microscopic equations. Secondly, the OPEs allow to consider patterns in a particular system from a general point of view. Thus the derivation of OPEs allows to show the analogy between nonlinear optics and hydrodynamics in one limit, or between nonlinear optics and oscillatory chemical systems in the other limit. One can thus learn apriori about dynamics of the systems without solving the equations, but just knowing the analogies with other systems. E.g. the knowledge of the existence of vortices in fluids and superfluids allows to predict and interpret the vortices in nonlinear optics thanks to the optics-hydrodynamic analogy.

OPEs for class-A and class-C lasers was derived in [14, 15] and are named Complex Swift-Hohenberg Equation (CSHE):

$$\partial_t A = pA + ia(\Delta + a\vec{\nabla}^2)A - \frac{(\Delta + a\vec{\nabla}^2)^2}{\Delta\omega^2} A - A|A|^2 \qquad (1.2.1)$$

The CSHE (1.2.1) describes spatio-temporal dynamics of the complex-valued order parameter $A(\vec{r},t)$, which is proportional to the envelope of the optical field. The parameter $p$ is the net gain parameter, $\Delta$ is the resonator detuning from the gain line frequency, $a$ is the diffraction coefficient depending on the total resonator length, and on finesse, $\Delta\omega$ is the width of the gain line.

The CSHE is a central equation for broad aperture (pattern forming) systems in nonlinear optics. First derived for lasers, the same equation was later derived as the OPE for Photorefractive Oscillators, and nondegenerate Optical Parametric Oscillators (OPOs), as shown in [16-20]. CSHE describes pattern formation not in a particular system, but in a class of nonlinear optical system characterized by:

1) Phase invariance. The CSHE is invariant with respect to the phase of the order parameter $A(\vec{r},t)$. It is the consequence of well known fact that in lasers (and laser-like systems) the phase of the optical field is arbitrary;

2) Diffraction. The nonlocality in lasers and laser-like systems is predominantly of diffractive type, which is different from e.g. the chemical systems, where diffusion is a dominating nonlocality.

3) Supercritical Hopf bifurcation. The order parameter changes continuously from zero when the gain parameter crosses zero. This is typical for type II (continuous) phase transition. Some systems in nonlinear optics (e.g. lasers with saturable absorber) are subcritical, and show hysteresis [21-23]

4) Spatial frequency selection. The third right hand term is responsible for spatial frequency selection. The laser, with a narrow gain line can be tuned not only over the longitudinal, but also over the transverse modes (transverse wave numbers). This tuning, or the spatial frequency selection, is mathematically described by the corresponding term.

OPE for Degenerate Optical Parametric Oscillators (DOPOs) is derived in [13, 19] and is so named Real Swift-Hohenberg Equation (SHE):

$$\partial_t A = pA - \frac{(\Delta + a\vec{\nabla}^2)^2}{\Delta\omega^2} A - A^3 . \qquad (1.2.2)$$

There the order parameter $A(\vec{r},t)$ is a real-valued field. $\Delta$ is also the resonator detuning for the signal wave, like in case of lasers (1.1). The parameter $\Delta\omega$, the analog of the width of the gain line is equal to $\sqrt{2}$ for the DOPO case.

The SHE (1.2.2) is encountered in many pattern forming problems, including the seminal ones: in Rayleigh-Benar convection, and formation of Turing patterns in morphogenesis. The derivation of SHE (2) for DOPOs allows to introduce another class of pattern forming systems in nonlinear optics which are characterized by following ingredients:

1) Squeezed phase. The phase of the order parameter is not invariant as in CSHE, but restricted to two values *0* and $\pi$, due to real-valuedness of the order parameter.

2) Suppressed diffraction. The diffraction in DOPOs (and in some other degenerate optical systems, like degenerate four wave mixers) is suppressed due to the phase-sensitive coupling of its components (e.g. of signal and idler waves of DOPOs);

3) Supercritical pitchfork bifurcation. In some limits (in particular for nonzero detuning of pump wave) the pitchfork bifurcation may be subcritical, and show hysteresis [21, 23].

4) Spatial frequency selection. The frequency of subharmonics of DOPO, being fixed by frequency of the pumping laser may be tuned with respect to the resonance of the cavity, thus the tuning over both longitudinal and transverse modes is possible.

Most pattern forming systems in nonlinear optics fell into one of these two classes defined by the OPEs (1.2.1) and (1.2.2). There are however systems beyond description by real and complex GLE. Such are subcritical systems, and they can be described by extensions of (1.2.1) and (1.2.2).

### 1.2.2. Vortex motion in moderate Fresnel number lasers

A normal laser has a resonator composed of two curved mirrors. If the gain line of the medium is narrower than the longitudinal mode separation, selected transverse modes may be excited by choice of resonator length. The frequency spacing of the transverse modes (of transverse order $N$) depends on the mirror radii $R_1$, $R_2$, and their distance $d$ as:

$$\Delta f = \frac{c}{2\pi l} \arccos \sqrt{g_1 g_2} \qquad (1.2.3)$$

where $g_i$ are $1 - l/(R_i)$ ($R_i$ : mirror curvature radii, $l$: resonator length, $c$: velocity of light). The transverse order $N$ is $m+n$ for Hermite modes in rectangular geometry, where $m$ and $n$ are the numbers of nodes along the two orthogonal directions in the transverse plane.

For circular geometry (Laguerre modes) $N = 2p+l$ where $p$ and $l$ are the numbers of nodes along the azimuthal and radial direction in the transverse plane.

With a narrow gain line several modes can be excited simultaneously if they are roughly not further apart in frequency than their resonance widths.

To excite modes with arbitrary indices simultaneously we have often utilised the fact that two transverse modes from *different* longitudinal orders can be made degenerate by a proper choice of resonator length and mirror curvature radii.

The resonator typically used in the experiments [24] is shown in Fig. 1.1. For the active medium photorefractive materials were used, mostly BSO. The amplification results from scattering of light out of the pump wave into the signal wave (resonator field) by a refractive index grating produced by the interference of the pump field with the signal (resonator) field. A “gain line” of width 0.1–10 Hz(!) results, which evidently means an enormous frequency pulling of a photorefractive oscillator, slowing down dynamics by a factor of $10^6$–$10^8$(!)[24].

Although this light amplification mechanism is completely different from the mechanism of light amplification of lasers, it can be shown that a laser of class A and a photorefractive oscillator as used here are described by the same equation [17]. Thus we can use the photorefractive oscillator with its characteristic time of 10–1000 ms as a "slow-motion laser" permitting recording of 2D dynamics, which is impossible with normal lasers, which have 1–100 ns characteristic times.

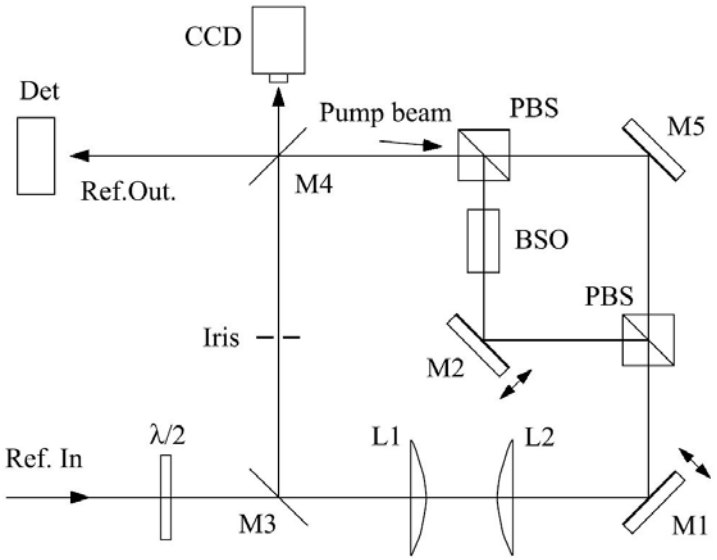


Fig. 1.1. Optical arrangement for observing laser dynamics on a two-wavemixing photorefractive oscillator. The active ring is formed by M1–M4, with BSO as the amplifying material. The resonator length is controlled actively using the bypass which is formed by PBSs and M5 [24].

Since the active medium amplifies in one direction, but absorbs in the opposite direction, a ring resonator is used. The spacing between transverse modes or degeneracies of those is controlled by the spacing of the two lenses. The tuning of the resonator has to be constant within a few hundred kHz, given a typical mode width of a few MHz. This is accomplished by active resonator length control. The resonator field can differ in frequency from the pump field at most by a few Hz. Consequently the resonator length is controlled with respect to the pump frequency. The photorefractive active material has a sizeable linear loss, thus the bypass formed by PBS and M5, which is distinguished from the active resonator by polarization forms a resonator of

high finesse, providing a sharp resonance for length stabilization. The difference between the active and the bypass resonator lengths is kept small by symmetric arrangement of the bypass elements on an Invar plate. It was found that stabilizing the bypass resonator resulted in a stability of the active resonator of a few 100 kHz for times of 10 minutes. Given the time scale of the photorefractive oscillator between 0.01 and 1 s, this stability is sufficient to ensure constant tuning of the active resonator for recordings of adequate length.

The simplest emission form of a field with a vortex is the emission called "$TEM_{01}$x hybridmode" in the laser literature (a $TEM_{01}$ Laguerre mode) which is bistable with respect to
helicity [24].

Figure 1.2 shows the intensity of such a field and by an interferogram proves its vortex character (i.e. the helicity of the wave fronts). Tuning the resonator to higher transverse mode families (order *N*) we noted a strong preference for emitting fields with a central *N*-fold phase singularity

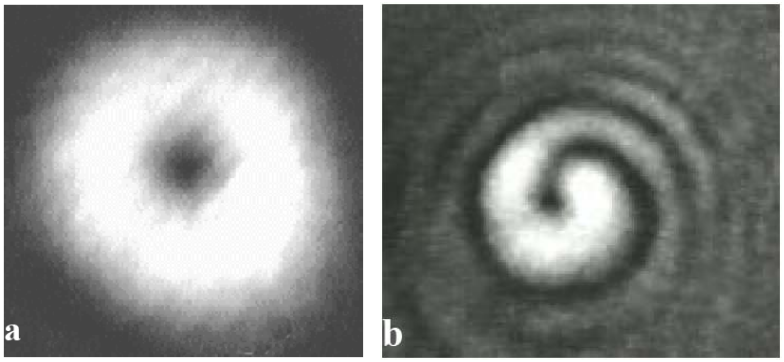


Fig. 1.2. Intensity (a) and interferogram (b) of a Gaussian field with a central phase singularity ("Doughnut-mode" field) as recorded from a BSO photorefractive oscillator [24].

Superposition of such fields with other fields splits the *N*-fold charged vortex into *N* singly charged vortices. If the two fields have different optical frequencies, periodic motion of the structure of the total field at the difference frequency results. For an added field symmetrical with respect to the optical axis vortices circle about the optical axis. The radial position of the vortices

depends on the intensity ratio of the two fields. The angular position of the vortices is given by the phase difference between the mode fields, as in a helical wave (vortex) spatial angle and phase obviously correspond. Different frequencies (i.e. linear increase of phase difference in time), consequently, lead to circling vortices. Fig. 1.3(a) shows a single vortex circling about the optical axis. Fig. 1.3(b) shows 3 and 8 vortices moving on concentric circles.

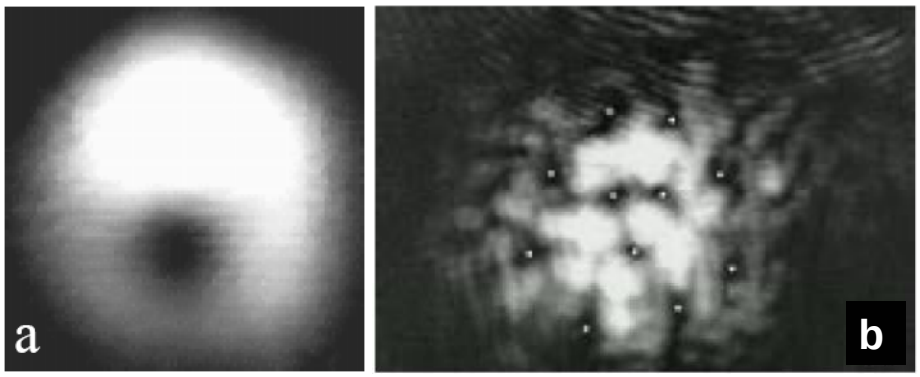


Fig. 1.3. (a) A vortex off the center of a Gaussian field (snapshot). The vortex circles with the frequency difference between the $TEM_{00}$ and $TEM_{01}$ field around the optical axis**.** (b) 8 vortices and 3 vortices counter circling on concentric trajectories [24].

### 1.2.3 Large Fresnel number lasers

Fresnel number first was introduced in the context of diffraction theory for beam propagation. Later Fresnel number has also been applied to optical resonators, in particular to laser resonators. Fresnel number is determined by formula:

$$N_F = \frac{a^2}{L\lambda} \qquad (1.2.4)$$

where $a$ is the radius of the end mirrors, $L$ is the resonator length and $\lambda$ is the wavelength.

In large-Fresnel-number resonators conversely the effects of the boundaries are unimportant and the dynamics is determined by the nonlinearities of the medium alone. Experiments under such conditions allow one therefore to test predictions of the fundamental equations describing the system, without the constraints of boundary conditions.

For such a resonator, in addition to large Fresnel number, the transverse modes must be degenerate in frequency to permit arbitrary images to be resonant.

The simplest cases of such degenerate resonators are the two-mirror-plane or -concentric resonators. Both, however, are very lossy and require exceedingly high gain to be excited. More complicated resonator structures [25], on the other hand, allow one to fulfill simultaneously the conditions of low loss and degeneracy. These can be described as consisting of "thick" mirrors (i.e. mirrors whose principal planes do not coincide with the mirror plane). It appears that the stability diagram of such resonators is a 3D continuation of the familiar 2D stability diagram of thin-mirror resonators. A resonator version, in which points representing stability and degeneracy simultaneously exist, as was used in the experiments, is the 4-f resonator and its equivalent 8-f ring [26-28]. With such resonators infinite Fresnel numbers are formally possible (within the frame of the paraxial wave approximation). Such resonators are equivalent to a plane resonator of length $d$ if their length differs by $+d$ from the degeneracy length. $d = 0$ corresponds to infinite Fresnel number. For finite $d$ the Fresnel number is reduced. Fresnel numbers of $10^4$ are easily achieved. This is to be contrasted with only $\approx 10$ for stable two-mirror resonators[24].

For these high-Fresnel-number resonators, where boundaries and frequency non-degeneracies can be disregarded, the complex Swift–Hohenberg equation, which describes a class A laser [29], predicts the following pattern formation:

For zero detuning of the resonator from the gain line the emission is a homogeneous plane wave with wave fronts perpendicular to the optical axis.

For detuning, the emission breaks up by way of a Turing instability into a regular square lattice of vortices of alternating charge (reminiscent of an alkali-halide crystal). The lattice constant is proportional to detuning. The

orientation of the lattice is arbitrary, i.e. it is determined by a spontaneous breaking of the rotational symmetry (Fig. 1.4(a)).

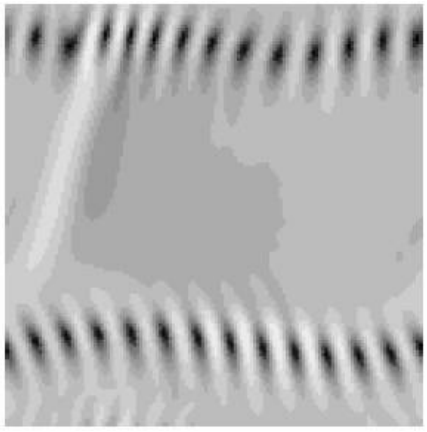

Fig. 1.5. 3-wave domains of opposite tilt (flow) separated by rows of vortices of equal charge [24].

If the pump is increased, defects appear in the lattice (Fig. 9(b)) in a manner reminiscent of the melting of a solidstate crystal. The defects are mobile and become more numerous and more mobile with increasing pump (Fig. 1.4(b, c)).

At some pump the crystal lattice is "molten", i.e. we have an irregular space–time dynamics with pair creation/anihiliation of oppositely charged vortices. This state one may call a "vortex fluid".[24]

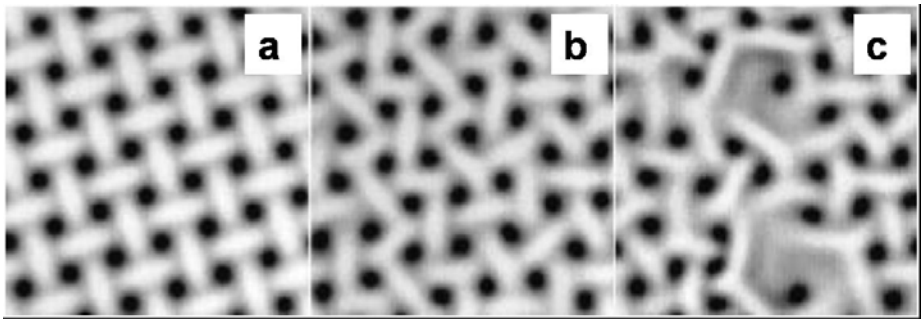


Fig. 1.4. Numerical solution of the laser GLE with detuning. The vortex lattice, which is stable near threshold, develops more numerous and more mobile defects as the pump is increased (near field) [24].

Increasing the pump further leads to a more ordered state: domains of differently oriented wave tilt (the latter corresponding in magnitude to the detuning chosen) appear, often separated by rows of vortices of equal charge (Fig. 1.5). Such state of the field can be described by a negative temperature [30], suggesting that an *amplification* of certain wave structures could occur under these conditions. It would therefore seem that the "vortex fluid" corresponds to a high positive (in the limit, infinite) temperature.

Further increase of pump then leads to a growth of certain domains (of "flow" or tilt) until the whole laser cross section is filled with a uniform wave of constant tilt [30]. Evidently under these conditions the wave has to show a "source" and a "sink" [31] at boundaries, without which a tilted ("travelling") wave or "flow" can not be sustained continuously in a finite cross section. More detailed predictions of the CSHE which describes a class A laser are reviewed in [24].

Experiments on these predictions was experimentally verified in [32]. An 8f ring resonator with $BaTiO_3$ as the active medium was used. (gain in two wave mixing is unidirectional: thus a ring resonator was used). Pump was a single-mode Ar laser at 514 nm. The near and far field was simultaneously recorded [32]. Figure 1.6 shows the square vortex lattice observed at small pump power and with detuning.

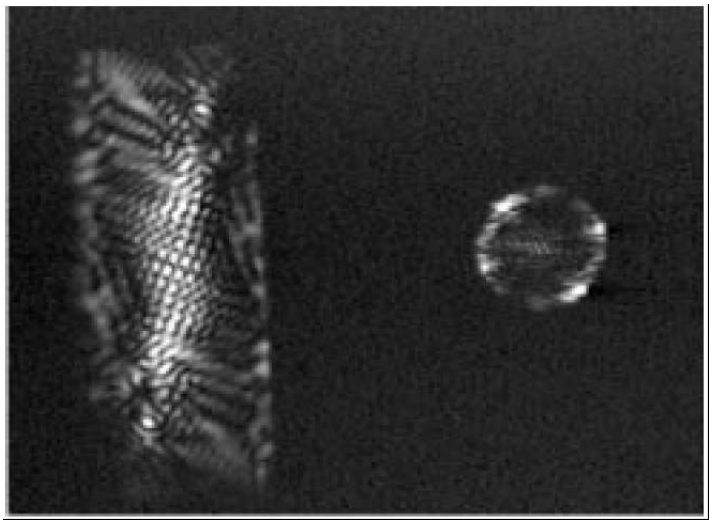

Fig. 1.6. A vortex lattice observed experimentally. The four tilted waves (coupled at a phase angle of $\pi/2$) forming the lattice are visible in the far field (Compare with Fig. 1.4) [32].

Figure 1.7 shows two domains of tilted waves (tilt is apparent in the far field), separated by a row of vortices, (compare with the theoretical calculation Fig. 1.5). The vortex row is plausible, considering that the domains have opposite tilt, and "shear flow" occurs therefore.

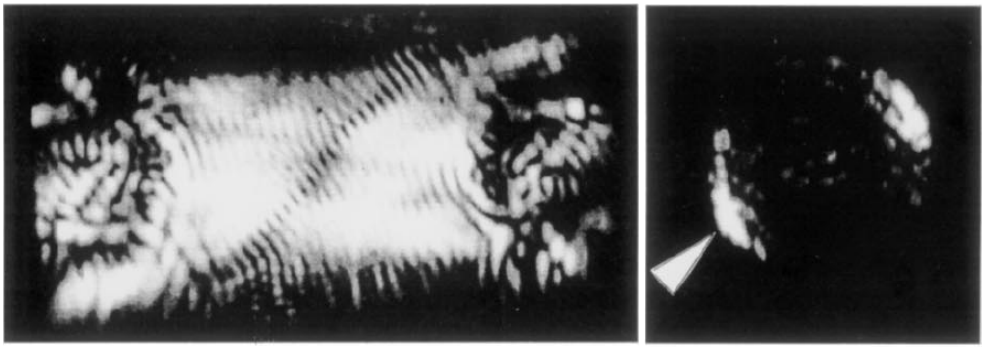

Fig. 1.7. Two domains of opposite tilt (flow) observed experimentally [32]. Compare with Fig. 1.5.

### 1.2.4. Solitons in DOPO and parametric mixing

Whereas the phase of the optical field of lasers is free – the laser can choose any phase value – in wave mixing the phase of the generated field(s) is coupled to the phase(s) of the pump field(s). For degenerate mixing such as degenerate four-wave mixing (D4WMO) or degenerate parametric mixing (DOPO) the generated field is thus a real quantity with respect to the pump field.

The order parameter of many non-optical pattern forming systems is also real. Such systems are for example a periodically forced Belousov–Zhabotinsky reaction or driven space charge wave fields. Another prominent system is Rayleigh–Benard convection, for which Turing patterns (rolls, hexagons) are characteristic. The spatio-temporal dynamics of these systems can be described by a real Swift–Hohenberg equation (SHE) (1.2.2) [33, 34].

Turing patterns occur for large positive detuning $\Delta$, for example in the form of stripes $A(r) \approx \sqrt{4/3}\cos(\vec{k}\vec{r})$ with a resonant wave-number $\left|\vec{k}\right| = \sqrt{\Delta}$. This limit of large detuning is characteristic for Rayleigh–Benard convection, where convective rolls have a defined size. SHE (1.2.2) with zero detuning describes parametrically excited systems, for which solutions of homogeneous amplitude and phase of $\varphi_0 = 0$ or $\pi$ are preferred. As opposed to non-optical systems the optical parametric resonators allow one to realize pattern formation for the whole detuning range, in particular, the intermediate patterns. Such patterns are contracting or expanding domains, and spatial localized structures.

There are only two possible values of the field phase: the optical field is bistable in its phase. As opposed to lasers where the continuously variable phase admits vortices (around whose core the phase varies continuously) in degenerate mixing vortices are consequently impossible. Allowed are lines of field zero between domains of opposite sign of the real field, i.e. of opposite phase.

Such dark lines in presence of nonlinearity become 1D continuations of "kink" solitons [35]. These dark lines or "fronts" [36] move in relation to their curvature [34]. They expand with a rate that is a growing function of the resonator detuning. For tuning close to zero the rate is negative (i.e. the fronts contract). It grows with detuning and becomes positive at a certain detuning, further growing with further detuning [34].

Figure 1.8 shows the front expansion rate as a function of the detuning as calculated from the real Swift–Hohenberg equation which describes these systems [34].

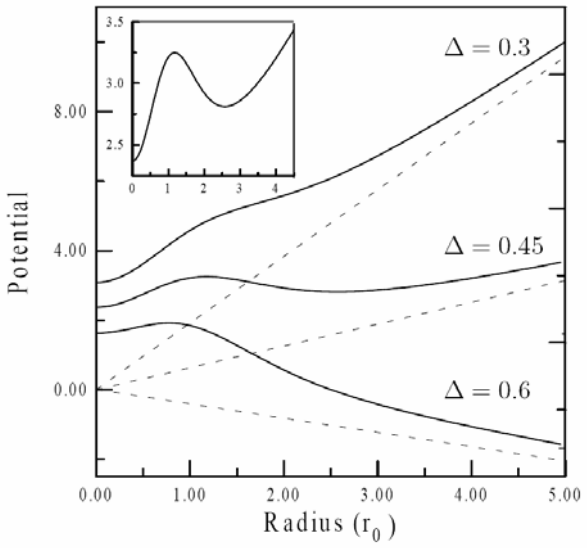


Fig. 1.8. The potential of a ring-shaped phase domain as a function of domain radius for different detunings Δ. For Δ around 0.45 a potential minimum indicates a stable structure, i.e. a spatial soliton. Inset: curve for Δ = 0.45 with vertical axis magnification [34].

For detuning corresponding to shrinking, dark fronts, initially curved, will in time straighten. For detuning corresponding to expanding lines the final

pattern will be a labyrinth structure that fills the whole available area [16]. The spacing of dark lines of this labyrinth pattern is given by the detuning (Turing pattern).

Although these dark fronts have soliton properties, they are not localized (particle-like) structures, as are the vortices and bright solitons in lasers.

However, a closer investigation shows that localized structures ("Ising structures") do exist [34]. Within the detuning range of dark front contraction, a front forming a closed loop will shrink. For small enough detunings its area goes to zero and the loop disappears. For larger detunings (where the expansion rate of dark fronts is still negative, however) such closed loops cannot shrink to zero because – simply speaking – two fronts repel, and the repelling of every two pieces of front on opposite sides of the loop can counterbalance the contraction of the front.

Thus detuning range closed loop fronts contract to a stable circle of finite radius. As the contraction strength of the front depends on the detuning, the stable circles have radii weakly dependent on the detuning.

These structures can again be pictured in a fluid analogy: the contraction of a closed loop front corresponds to the surface tension of a bubble. If it is large enough, (detuning close to zero) it can annihilate the bubble. For larger detuning the surface tension is counterbalanced by the pressure inside the bubble and for still larger detunings the internal pressure exceeds the surface tension. This analogy is nicely observed in the calculation and in experiments: inside the front loops the light intensity (= fluid density = pressure) is higher than outside. Clearly the light inside is "compressed" (See Fig. 1.9)[24].

These stable closed circular front loops (or the region inside the circle, which has opposite phase to the light outside) are clearly localized structures. In fact, analogously to the bright spatial solitons of lasers or non-linearly absorbing resonators, they are bistable.

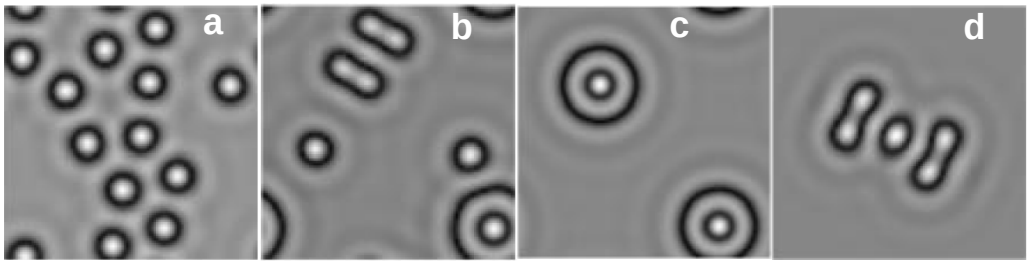


Fig. 1. 9. Different stable localized structures for a DOPO as calculated ("molecules"). (a) - Fundamental solitons. (b) - Bound states between fundamental and higher order solitons. (c) - 2 second-order solitons. (d) - A complicated bound state [24].

Quite obviously at the location of such a localized structure, which is distinguished from its surrounding by the phase, the phase could as well be the same as that of the surrounding; in which case there would be no localized structure. Consequently, the localized structure described here is equally bistable and free to move around, to be "written" and "erased", as are the bright spatial solitons of nonlinear (laser-) resonators. Figure 1.9 shows such localized structures as calculated for the DOPO equation.

As a larger number of theoretical investigations about the dark fronts in DOPOs exists [16], experiments were conducted to prove the theoretical predictions experimentally [37].

For the experimental system degenerate four-wavemixing was chosen, which permits (using again photorefractive nonlinear material) observation on a convenient time scale. It is described by the same real SH equation as DOPOs [19]. The experimental setup is given in Fig. 1.10. Two pump waves with two generated waves form an index grating in the nonlinear material from which light is scattered from the pump waves into the generated waves. The generated fields combined form the resonator field of a linear resonator. The resonator for the generated field is again laid out as a 4f self-imaging resonator to permit realization of a low-loss resonator with degenerate transverse modes and very large Fresnel number allowing resonance of complex patterns.

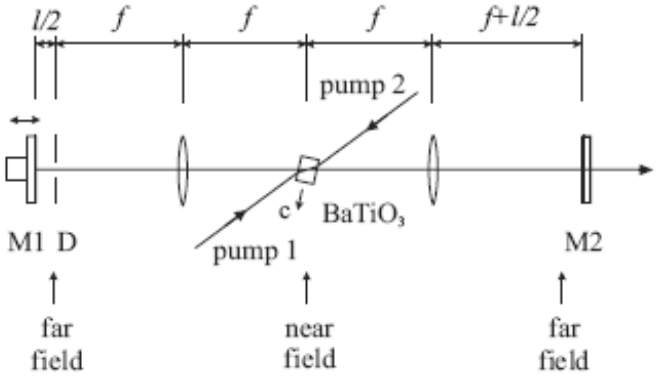


Fig. 1.10. Optical arrangement for observing structures in four-wave mixing (or DOPO) is a self-imaging linear 4f resonator with photorefractive $BaTiO_3$ as mixing medium and 2 pumps [24].

The fields generated were found experimentally to show all predicted features. Typically, domains separated by black lines of irregular shape were observed in the emission (Fig. 1.11(a)). The domain boundaries can have quite a complicated form, including self-crossings, and move in general. Fig. 1.11(b) shows the intensity of a portion of the emitted radiation, as well as a interferogram made with a plane wave Fig. 1.11(c), showing a phase difference of $\pi$ between domains, thus proving the real-valued nature of the order parameter of emitted field.

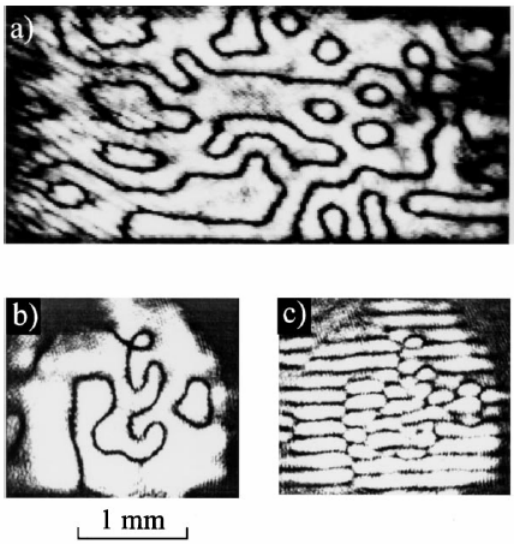


Fig. 1.11. Domains of complicated shape as obtained experimentally: (a) The near field of the whole beam, (b) a small section from the whole beam, and (c) interferogram, showing that the adjacent domains have opposite phase [37].

### 1.2.5. Spatial structures in synchronously pumped optical parametric oscillators

First report of experimental observation spatial patterns was in synchronously pumped

degenerate optical parametric oscillators (SPOPOs) on type I and type II phase matching crystals [3]. A confocal resonator configuration, providing high Fresnel numbers and high degeneracy of resonator transverse modes was used for experiments.

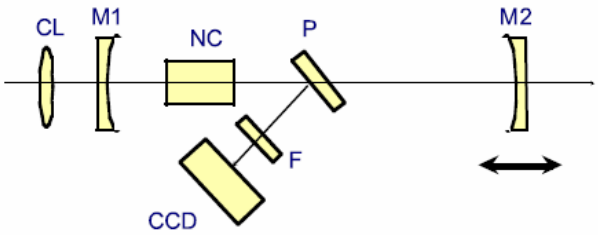


Fig. 1.12. Experimental set-up of SPOPO

Nd:glass laser with passive mode locking and active negative feedback was used as a pump for the SPOPO. The parameters of pump pulses: duration 1.7 ps, wavelength 527 nm, energy (of a single pulse in the train) 60 μJ. The confocal SPOPO (Fig. 1.12) consisted of the concave mirrors M1, M2 of 95% reflectivity in the spectral region 950–1110 nm, and a nonlinear crystal (NC). The nonlinear crystal was pumped through the mirror M1. The transmission of the mirrors for the pump wave was more than 85 %. The optical length of the SPOPO cavity was equal, twice or three times shorter than the length of the pump laser cavity. The exact tuning of the SPOPO resonator to modelocked pumping was achieved by continuous displacement of the mirror M2. The experiments were performed on type I (CDA and KDP) and type II (KDP) phase matching crystals. Cylindrical focusing was used to reach the threshold intensity and to ensure a large Fresnel number (~20–60), at least in one plane. Pump beam size on the entrance face of the crystal was 6 x 0.3 mm (at the $e^{-2}$ level) in horizontal and vertical directions, respectively. The signal reflected from the glass plate (thickness 6 mm), placed inside the cavity, was directed to the CCD camera. The distance between the CCD camera and nonlinear crystal was 22 cm

The SPOPO spatial structure has shown dependence on the resonator length mismatch and mirror misalignment. The largest variation of the transverse structure caused by mirror misalignment was observed in the case of the confocal cavity with mirrors with radii R1 = R2 = 560 mm and the largest Fresnel number. In this case the characteristic stripe structure consisted of 2, 3 and 6 stripes (Fig. 1.13). In case of resonator length mismatch, the beam structure transforms from stripe to circle and back to a stripe (Fig 1.14).

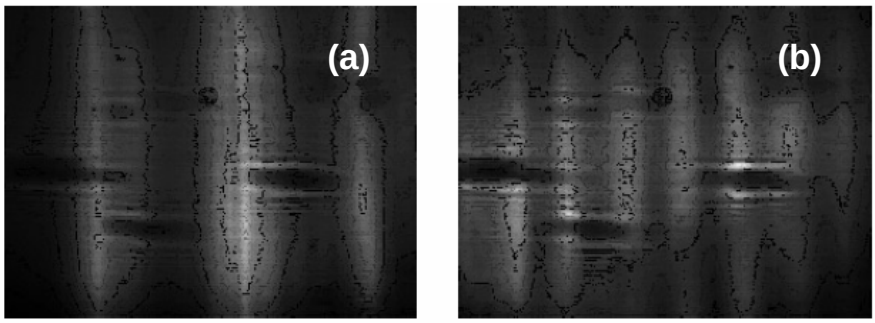


Fig. 1.13. Spatial structure of SPOPO (crystal CDA, type I phase matching) emission in the case of large (*a*) and small (*b*) mirror misalignment with respect to the pump beam axis. Misalignment takes place in the phase matching plane [3].

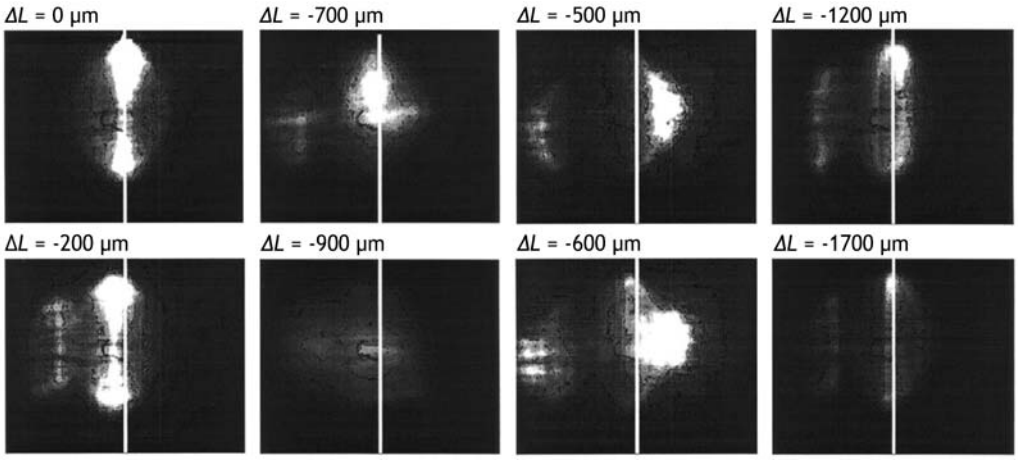


Fig. 1.14. Spatial structure of SPOPO (CDA crystal, type I phase matching). Dependence versus resonator length detuning. $\Delta L$ is the mismatch from $L$ = 807 mm, the resonator length, which corresponds to the maximum of synchro-resonance curve. White line indicates the position of the beam when $\Delta L = 0$ [3].

As concluding, it has been shown experimentally in [3] that complicated light field structures can appear in SPOPOs due to boundary effects (pumping

conditions, different resonator configurations, phase matching conditions) and can be interpreted as the simultaneous excitation of the transverse resonator modes, but not essentially nonlinear pattern formation. The spatial structure formation in such circumstances is driven by noncollinear parametric interaction and oscillation of higher transverse modes. For SPOPO cavities with small Fresnel numbers when higher transverse mode generation is not possible the spatial structure formation is caused mainly by noncollinear parametric interaction, however, for SPOPO cavities with large Fresnel numbers the variation of the spatial structure due to the SPOPO mirror misalignment and cavity length mismatch is caused by the oscillation of higher transverse modes and additionally due to noncollinear parametric interaction.

## 1.3 Temporal and spatial properties of photonic crystals

### 1.3.1 Nature and properties of photonic bandgaps

The idea of the periodic photonic crystal was conceived by Yablonovitch [38] who initially proposed to use such structures for the control of spontaneous emission processes in semiconductors. The initial concept was developed further in a series of subsequent works [39-41]. It relies heavily on the analogy between electrons in the periodic potential of the crystalline atomic lattice, and EM waves in a medium with periodically modulated optical

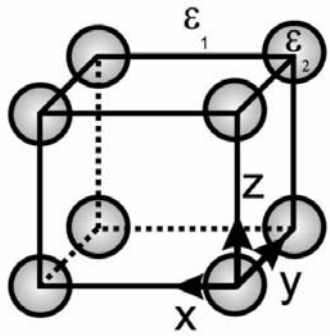


Fig. 1.15. Schematic images of 3D cubic photonic crystals: primitive cell with spherical dielectric "atoms" having $\varepsilon_2$ and placed at the lattice nodes in the medium with $\varepsilon_1 \neq \varepsilon_2$

properties. Broader explanation of the physical principles and ideas motivating the PhC research, are given by Yablonovitch [42, 43] and by Joannopoulos et al. [44]. More condensed reviews are given in [45].

Response of the material to EM waves, including light waves, is described by its dielectric permittivity $\varepsilon$ and magnetic susceptibility $\mu$. The dielectric permittivity is in general a complex quantity $\varepsilon = \varepsilon' + i\varepsilon''$. Its real part $\varepsilon'$ describes the refractive properties of the material, and is often represented by the refractive index $n = \sqrt{\varepsilon'}$. The imaginary part $\varepsilon''$ describes dissipative damping of the wave's amplitude via absorption. (In terms of this work negligible absorption can be assumed) The material is regarded as non-magnetic, i.e. $\mu = 1$ independent of the spatial coordinates.

The most important similarity between photonic and solid crystals is their translational symmetry. Photonic crystals can be formed from materials satisfying the requirements outlined above by periodically modulating their dielectric properties $\varepsilon$ (or $n$) in space. A simple way to do so is to periodically remove volumes of homogeneous dielectric material with $\varepsilon_1$, and fill them with another dielectric with $\varepsilon_2 \neq \varepsilon_1$. As a result, a periodic dielectric arrangement with dielectric contrast $\varepsilon_2/\varepsilon_1$ (refractive contrast $n_2/n_1$) will be created. Since air has low value $\varepsilon = 1$, PhC can be fabricated by periodically removing some parts of the material from a dielectric with $\varepsilon > 1$. Alternatively, one can assemble spatially periodic arrangements from small dielectric "atoms" in air or other medium. One of the most common characteristics of photonic structures is the *filling ratio*, which describes the percentage of total crystal volume occupied by the dielectric material. Fig. 1.15 sketches a unit cell of a PhC structure that consists of spherical "atoms" (marked by darker shades of gray) placed at the nodes of a 3D cubic lattice. An extended periodic PhC can be obtained by translating the unit cell along the vectors:

$$\boldsymbol{T}ijk = i\boldsymbol{x} + j\boldsymbol{y} + k\boldsymbol{z}, \qquad (1.3.1)$$

where $\boldsymbol{x}$, $\boldsymbol{y}$ and $\boldsymbol{z}$ are the primitive translation vectors, and $i$, $j$ and $k$ are arbitrary integers. Photonic lattice type definitions and classifications are adopted from

crystallography. Since we anticipate importance of periodicity in PhCs, a reciprocal lattice with primitive vectors $\boldsymbol{g}_1$, $\boldsymbol{g}_2$ and $\boldsymbol{g}_3$ is defined in reciprocal space by analogy with solid state physics:

$$g_1 = \frac{2\pi}{x[y \times z]}[y \times z],\ g_2 = \frac{2\pi}{x[y \times z]}[z \times x],\ g3 = \frac{2\pi}{x[y \times z]}[x \times y]. \qquad (1.3.2)$$

Photonic crystals must have a period comparable to the EM wavelength (typically in the range from microwave to visible). The first photonic crystal working in the microwave spectral region was fabricated by Yablonovitch et al. [40] by mechanical drilling of oriented holes through a slab of dielectric.

If an EM wave with wavelength $\lambda$ is incident on a PhC, dielectric discontinuities introduced by the "atomic" sites will result in multiple scattering and diffraction. Interference between the scattered fields, may be constructive or destructive, as in the case of X-rays (or electronic waves) in solids. The well-known Bragg condition [46] describes complete X-ray reflection in the periodic crystal at $\lambda = 2d \sin(\theta + \delta)$, where $\theta$ and $\delta$ are incidence and reflection angles, respectively, and $d$ is the distance between the atomic planes. This condition also applies for EM waves in photonic crystals.

Propagation of EM waves is described by the set of Maxwell's equations:

$$\nabla \times \vec{E} = -\frac{\partial \vec{B}}{\partial t}, \qquad (1.3.3)$$

$$\nabla \times \vec{H} = \sigma \vec{E} + \frac{\partial \vec{D}}{\partial t}, \qquad (1.3.4)$$

$$\nabla \vec{D} = \rho, \qquad (1.3.5)$$

$$\nabla \vec{B} = 0, \qquad (1.3.6)$$

$$\vec{D} = \varepsilon_0 \varepsilon(\vec{r}) \vec{E}, \qquad (1.3.7)$$

$$\vec{B} = \mu_0 \mu \vec{H}, \qquad (1.3.8)$$

It can be shown that Maxwell's equations can be transformed into the following expression for harmonic magnetic modes:

$$\left[\nabla \times \frac{1}{\varepsilon(\vec{r})}\nabla\right] \times H_{\omega}(r) = \omega^2 \vec{H}(r) \qquad (1.3.9)$$

(Mathematically similar electron propagation is described by the Schrödinger equation [46]) For EM waves in isotropic medium, Eq. (1.3.9) have plane wave solutions $\vec{E}_k(\vec{r},\omega,t) = E_0 \exp[i(\vec{k}\vec{r} - \omega t)]$. In this case, the dispersion is also continuous but is described by the linear law (Fig. 1.16 (a)): $\omega = ck/\sqrt{\varepsilon}$, where $c$ is the speed of light.

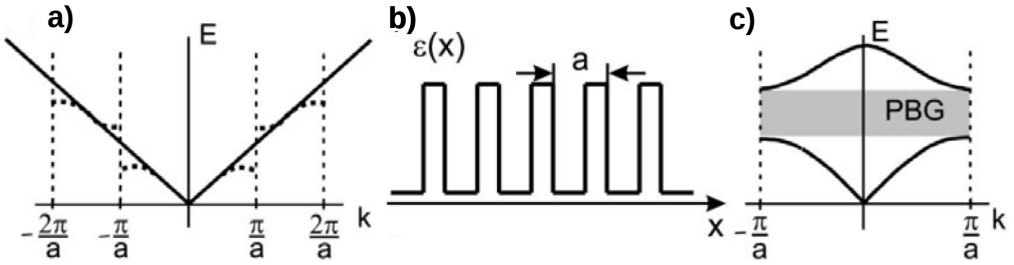


Fig. 1.16. Dispersion relations for electromagnetic waves in isotropic media (a), (plotted as solid lines). Sketch of one-dimensional periodic dielectric susceptibility *ε(x) (b)*. The dispersion relations for EM waves modified due to the periodicity are sketched in (a) by dashed lines. Folding of the *k*-space to the first Brillouin zone and representation of the energy bands within this domain for EM waves (c) [47].

Periodic modulation of the environment can be described by following condition: $\varepsilon(\vec{r} + \vec{T}) = \varepsilon(\vec{r})$, where $\vec{T}$ is a translation vector. For EM waves, an approach equivalent to the weakly perturbed electron approximation is realized by substituting the EM Bloch waves into Eq. (1.3.9), and yields *E(k)* dependencies, modified as schematically shown in Fig. 1.16(b) by dashed lines. Just as in the case of electrons, the dispersion relations are no longer smooth, and manifest forbidden energy gaps, or photonic band gaps at $k_i$. The periodicity of photonic lattice folds the dispersion relations into the first Brillouin zone ($[-\pi/a; \pi/a]$) in reciprocal space, as shown in Fig. 1.16(c). EM states with energies in the PBG are forbidden, and if such waves are incident on the structure from outside, they will be rejected. This mechanism of light reflection is widely exploited in dielectric Bragg mirrors, which in fact are

stacks of alternating dielectric layers with different values of refractive index, and thickness equal to a quarter of the EM wavelength. Conventional explanation of almost 100 % Bragg mirror reflectivity within some wavelength range (stop-band) is based on the destructive interference between waves, multiply reflected from the internal interfaces. On the other hand, stop-bands can be understood as manifestations of one-dimensional photonic band gaps.

Two-dimensional photonic crystals systems exhibit most of the important characteristics of photonic crystals, from nontrivial Brillouin zones to topological sensitivity to a minimum index contrast, and can also be used to demonstrate most proposed photonic-crystal devices. The key to understanding photonic crystals in two dimensions is to realize that the fields in 2D can be divided into two polarizations by symmetry: TM (transverse magnetic), in which the magnetic field is in the (*xy*) plane and the electric field is perpendicular (*z*); and TE (transverse electric), in which the electric field is in the plane and the magnetic field is perpendicular.

Corresponding to the polarizations, there are two basic topologies for 2D photonic crystals, as depicted in Fig. 1.17: high index rods surrounded by low index (top) and low-index holes in high index (bottom). Here, we use a hexagonal lattice because, as noted earlier, it gives the largest gaps. Recall that a photonic band gap requires that the electric field lines run along thin veins: thus, the rods are best suited to TM light ( $\vec{E}$ parallel to the rods), and the holes are best suited to TE light ( $\vec{E}$ running around the holes). This preference is reflected in the band diagrams, shown in Fig. 1.17, in which the rods/holes (top/bottom) have a strong TM/TE band gap. For these diagrams, the rod/hole radii is chosen to be 0.2a/0.3a, where a is the lattice constant (the nearest neighbor periodicity) and the high/low ε is 12/1. The TM/TE band gaps are then 47%/28% as a fraction of mid-gap frequency, but these band gaps require a minimum ε contrast of 1.7/1 and 1.9/1, respectively. Moreover, it is conventional to give the frequencies ω in units of 2πc/a, which is equivalent to a/λ (λ being the vacuum wavelength)—Maxwell's equations are scale-

invariant, and the same solutions can be applied to any wavelength simply by choosing the appropriate *a*. For example, the TM mid-gap ω in these units is 0.36, so if one wanted this to correspond to λ = 1.55μm one would use a = 0.36·1.55μm = 0.56μm.

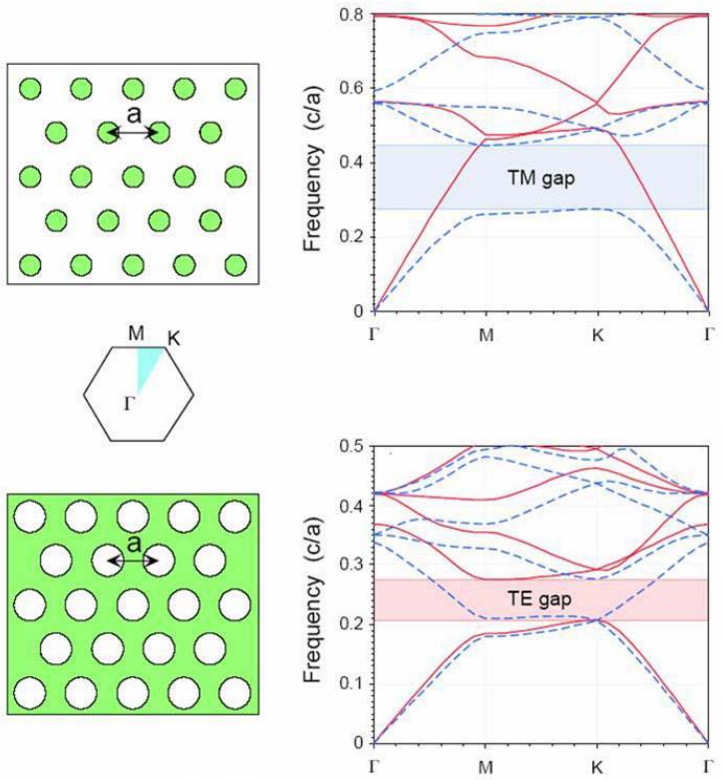


Fig. 1.17. Band diagrams and photonic band gaps for hexagonal lattices of high dielectric rods (ε = 12, r = 0.2a) in air (top), and air holes (r = 0.3a) in dielectric (bottom), where a is the center-center periodicity. The frequencies are plotted around the boundary of the irreducible Brillouin zone (shaded triangle, left center), with solid-red/dashed-blue lines denoting TE/TM polarization (electric field parallel/perpendicular to plane of periodicity). The rods/holes have a gap in the TM/TE bands.

The Brillouin zone (a hexagon) is shown in the inset, with the irreducible Brillouin zone shaded (following the sixfold symmetry of the crystal); the corners (high symmetry points) of this zone are given canonical names, where Γ always denotes the origin $\vec{k} = 0$, K is the nearest-neighbor direction, and M is the next-nearest-neighbor direction. The Brillouin zone is a two-dimensional region of wave vectors, so the bands $\omega_n(\vec{k})$ are actually surfaces, but in practice the band extrema almost always occur along the

boundaries of the irreducible zone (i.e. the high-symmetry directions). So, it is conventional to plot the bands only along these zone boundaries in order to identify the band gap, as is done in Fig. 1.17. Actually, the hole lattice can display not only a TE gap, but a complete photonic band gap (for both polarizations) if the holes are sufficiently large (nearly touching).

### 1.3.2 Nondifractive light propagation in photonic crystals

A decade after first Yablonovitch works [38, 40] it was found that the *spatial* dispersion (diffraction) characteristics also modify substantially in periodic materials: the diffraction can become negative [48, 49], or can vanish to zero [50-54], resulting in the so-called self-collimation effect in the latter case. A self-collimated beam of light does not spread when it propagates in photonic crystal. In contrast to spatial solitons, where the nonlinearity of homogeneous medium counteracts the natural spreading of the beam due to diffraction, the formation of self-collimated, or self-guided, beams in photonic crystal is a purely linear phenomenon. The spreading of the beam is counteracted by the crystal anysotropy, such that all wave vectors building the beam lead to the power flux in the same direction.

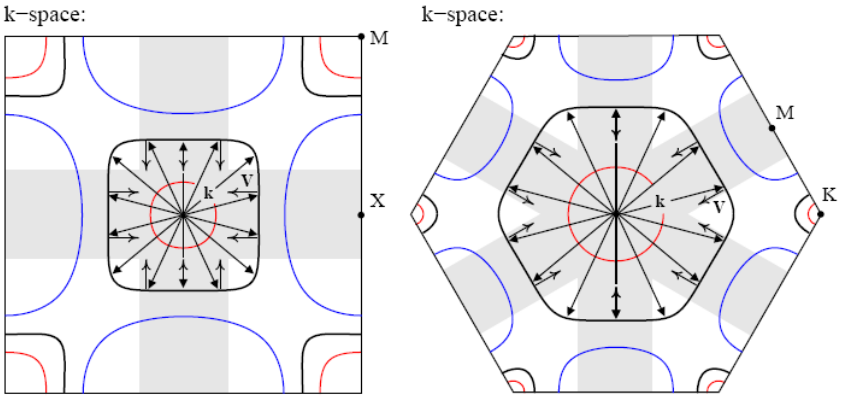


Fig. 1.18. Convex (red), concave (blue) and flat (black) iso-frequency contours. Iso-frequency contours on the left (right) panel correspond to the second band of a two-dimensional square (triangular) lattice photonic crystal made of dielectric rods in vacuum. Rods have the refractive index 2.9 and radius $r = 0.15d$, where $d$ is the lattice period. The wave vectors resulting in the Bloch eigenwaves with the group velocity pointing to the direction normal to the Brillouin zone boundary are depicted with arrows [52].

This can be realized for the wave vectors ending at the flat regions on an iso-frequency surface of a photonic crystal. The self-collimation regime reported by Kosaka *et al.* [55] relies on the inflection points of an iso-frequency surface, where the Gaussian curvature of the surface tends to zero. Typically, a flat region spreads over very limited wave vector directions centered at the wave vector ending at the inflection point. As a consequence, selfcollimation can occur only for very limited orientations of the beam with respect to the crystal lattice and for limited beam widths.

For some frequencies the form of iso-frequency surface mimics the form of the Brillouin zone of the crystal. In Fig. 1.18, iso-frequency contours for realistic square (left) and triangular (right) lattice photonic crystals are depicted. With changing frequency, the anisotropy of a photonic crystal changes dramatically, its iso-frequency contours evolve from convex (red contours in Fig. 1.18) to concave (blue contours in Fig. 1.18). There exists a frequency range where an iso-frequency contour forms almost perfect square or hexagon. Then, a wide angular range of flat dispersion exists canceling out diffraction of a light beam with the corresponding range of wave vectors (Fig. 1.18).

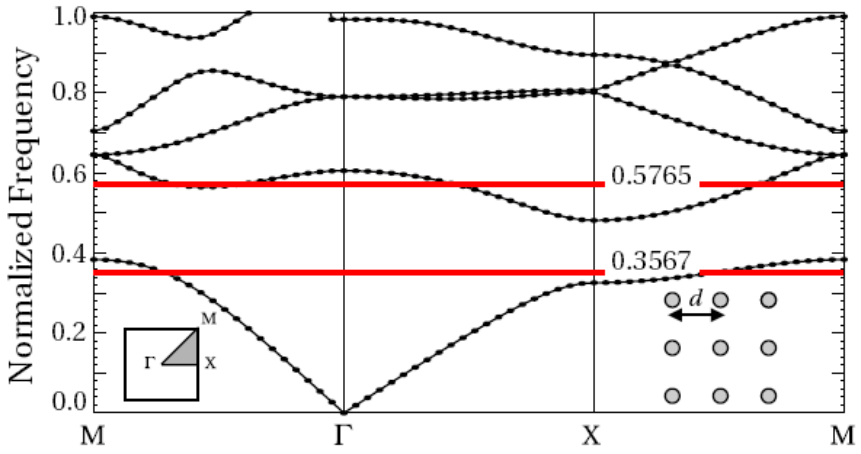


Fig. 1.19. Photonic band structure of the square lattice photonic crystal made of dielectric rods in vacuum. Rods have the refractive index 2.9 and radius $r = 0.15d$, where $d$ is the lattice period. The band structure is given for TM polarization. The frequency is normalized to $\Omega = \omega d/2\pi c = d/\lambda$ . $c$ is the speed of light in the vacuum. Insets show the first Brillouin zone (left) and a part of the lattice (right) [52].

2D infinite size photonic crystal (Fig. 1.19) is studied with restriction to the case of in-plane propagation. Consequently, the problem of electromagnetic wave interaction with a 2D photonic crystal is reduced to two independent problems, which we call TE (TM) when the magnetic (electric) field is parallel to the rods axis. In what follows, we limit ourselves to the case of TM modes. The photonic band structure of the square lattice photonic crystal made of dielectric rods in vacuum is shown in Fig. 1.19. The refractive index of the rods is 2.9 and their radius is $r = 0.15d$, where $d$ is the period of the lattice. A band structure calculations was done using the plane wave expansion method [56].

The analysis is performed with first two bands of the crystal, the iso-frequency contours of which evolve from convex to concave topology. In Fig. 1.20 transition iso-frequency contours corresponding to the normalized frequencies $\Omega = d/\lambda = 0.3567$ (the first band) and $\Omega = d/\lambda = 0.5765$ (the second band) are depicted.

The iso-frequency contour for the normalized frequency $\Omega = d/\lambda = 0.3567$ forms a square with rounded corners, rotated by 45± with respect to the Brillouin zone and centered at M-point of the first Brillouin zone (Fig. 1.20, left). The iso-frequency contour for the normalized frequency $\Omega = d/\lambda = 0.5765$ consists of two branches, which are plotted in red and blue in Fig. 1.20, right. Both branches mimic the form of the first Brillouin zone of the crystal being squares with rounded corners. The ”red” branch is centered at the G-point and the ”blue” branch is centered at the M-point of the Brillouin zone (Fig. 1.20, right).

The important feature of the wave propagation inside a photonic crystal at the considered normalized frequencies is that even a cylindrical initial wave results in an energy flow strongly focused along some specific directions, while it remains negligible for all other directions. To emphasize this special type of self-collimated electromagnetic wave propagation inside a photonic crystal will refer to it as *self-guiding*.

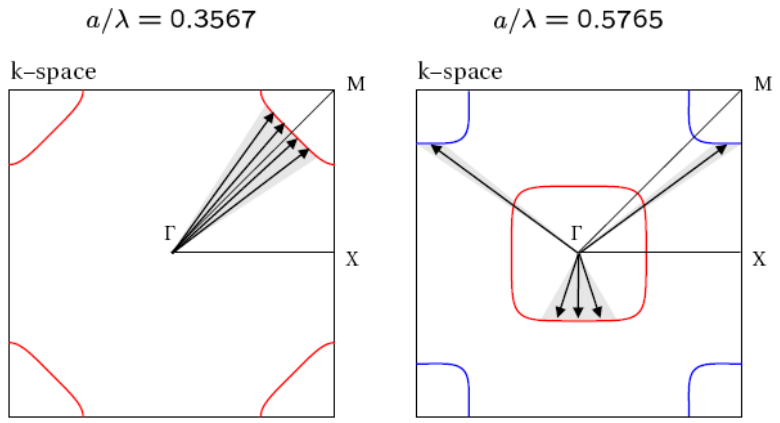


Fig. 1.20. Iso-frequency diagram for the normalized frequencies $\Omega = d/\lambda = 0.3567$ (left) and $\Omega = d/\lambda = 0.5765$ (right). The shaded regions show the wave vectors resulting in the Bloch eigenwaves with the group velocity vectors pointing to the same direction. The crystal parameters are given in Fig. 1.19 caption [52].

In Fig. 1.21 the electric modulus field map is shown, when a 30x30 rod crystal is excited by a point isotropic source at the normalized frequencies W = $d$/l = 0.3567 (left) and W = $d$/l = 0.5765 (right). The point source is placed in the middle of the crystal, at $x0 = 0$ and $y0 = 0$. The emitted light is guided in channels in the [11] and [10] directions, correspondingly, as it was predicted in the previous section.

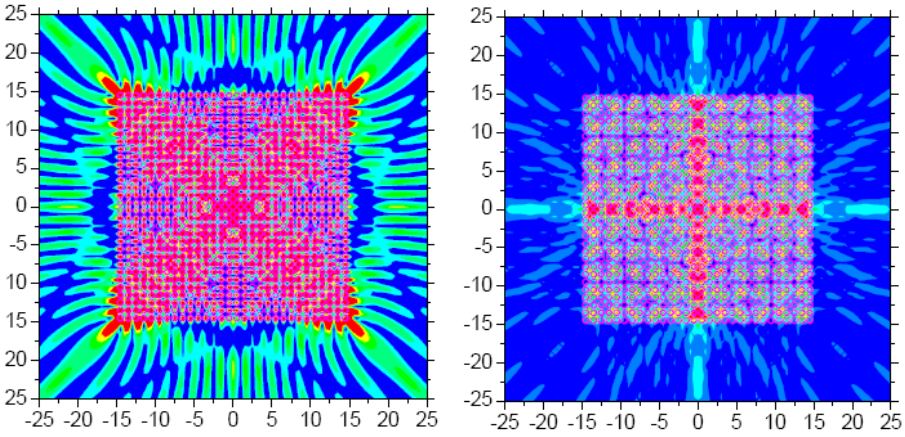


Fig. 1.21. Modulus of the electric field map for a 30x30 rod photonic crystal excited by a point isotropic source. Left, W = $d$/l = 0.3567; right, W = $d$/l = 0.5765. The axis scales are in units of $d$ and the colorscale is from 0 (blue) to 1 (red) [52].

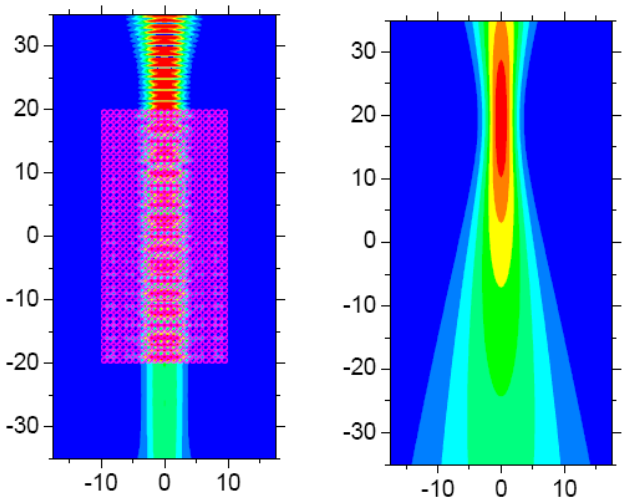


Fig. 1.22. Self-guiding in a limit-size photonic crystal. Left: Modulus of the electric field map for a 20x40 rod photonic crystal illuminated by a Gaussian beam with $W/d = 2.5$, $\Omega = d/\lambda = 0.5765$. Right: Modulus of the electric field of the incident Gaussian beam. The axis scales are in units of $d$ and the colorscale is from 0 (blue) to 1 (red) [52].

In Fig. 1.22, a rigorous numerical simulation of self-guided Gaussian beam is presented for a normalized frequency $\Omega = d/\lambda = 0.5765$. Figure 1.22, right shows the field map of the TM polarized incident beam, where the width of the beam is $W/d = 2.5$ and the waist is located at $x_0 = 0$ and $y_0/d = 19.5$. The self-guiding in the [10] lattice direction is shown in Fig. 1.22 left. The crystal is made of 20x40 rods and is illuminated from the top by an incident Gaussian beam. The guiding of the beam is obvious in the photonic crystal, as seeing by comparing the width of the beam at the bottom of the crystal and at the same ordinate in free space. The width of the incident beam fully defines the width of the self-guided beam in the crystal. In the same time, the presence of the self-guiding phenomenon does not depend on the incident beam width. It is important to note that in this study we did not make any attempt to optimize the coupling of the incident beam. The transmitted energy below the crystal is about 33% of the incident one.

Diffractionless propagation over 12 diffraction lengths for both polarizations theoreticaly and experimentaly was demostrated by R.Iliew *et. al.* [53]. PhCs with a width of 100 mm and a length of 128 mm, 255 mm and 510

mm were fabricated for operation near 1.5 μm. The scanning electron microscope (SEM) images (see Fig. 1.23) of the optical facet reveal deeply etched holes (total depth 950 nm) and an average hole diameter of 285 nm. In order to couple light of a defined width into the structure ridge waveguide tapers were used, where the ridge waveguide width at the photonic crystal interface was 1.5 or 2.5 mm.

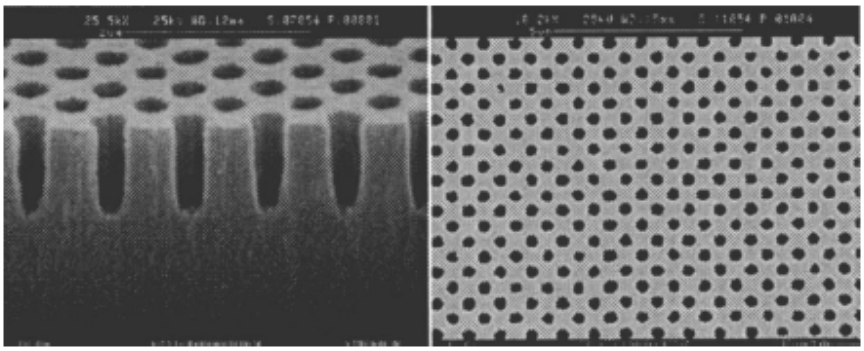

Fig. 1.23. SEM images of the fabricated photonic crystals consisting of holes with a diameter of 285 nm and a depth of 950 nm (aspect ratio of 1:3) in a quadratic lattice with pitch 600 nm [53].

To evaluate the propagation loss and to monitor the selfguiding behavior the light of a tunable continuous-wave optical parametric oscillator was coupled with the desired polarization (TE or TM) into the taper via a standard telecom fiber, and the top view stray light was recorded for different fixed wavelengths via a microscope objective (125X, NA = 0.8) and an infrared camera. The self-collimation effect in dependence on the wavelength could be monitored directly. For obtaining the propagation loss first the stray light intensity was integrated over the transverse beam coordinate. Then the resulting dependence on propagation length was fitted with an exponential decay function. For TE polarization the stray light images revealed that for wavelengths between 1.578 and 1.612 μm the input beam is neither broadened nor does it split up upon propagation over 510 μm in the PhC (see Fig. 1.24). This wavelength range of self-collimation is in full agreement with the numerically obtained transmission spectrum. In contrast, detuning the

wavelength the beam splits up into two or even more individual beams. However, this splitting does not become apparent up to a propagation length of 150 μm.

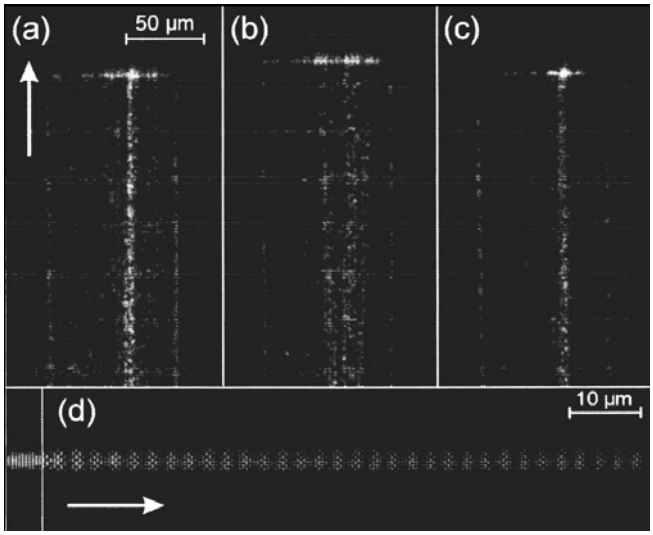


Fig. 1.24. Stray light images showing the last 200 μm of the 510 μm long PhC for TE polarization at a wavelength (a) of 1.599 μm, (b) of 1.622 μm, and (c) for TM polarized light at 1.492 μm. Streaks of reflected light mark the boundaries of the PhC region. (d) FDTD calculation for TE monochromatic excitation at l=1.6 mm, the white line denoting the PhC interface; (arrowsdirectionof propagation) [53].

Analytical study of nondiffractive light propagation in photonics crystals phenomenon is presented by K.Staliunas and R.Herrero in [54]. Superposition of two periodic lamellaelike refraction index gratings: $\Delta n(\mathbf{r})=2m[\cos(\mathbf{q}_1\mathbf{r})+\cos(\mathbf{q}_2\,\mathbf{r})]$ with $|q_1| = |q_2| = q$ at angles ±α to the optical axis, as shown in Fig. 1.25.

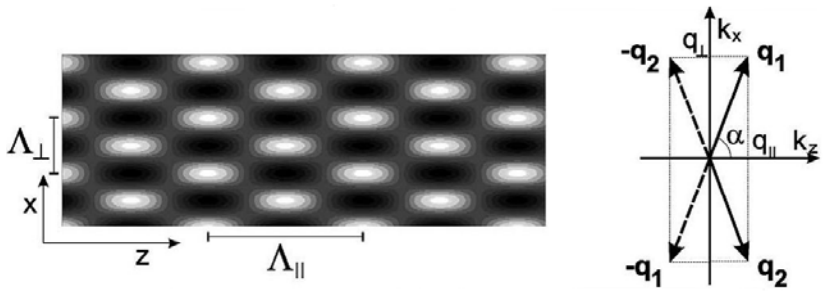


Fig. 1.25. Harmonic modulation of refraction index as, e.g., imposed holographically in photorefractive material. In this twodimensional case the grating is written by two pairs of counter propagating beams [54]

This results in refractive index modulation profile $\Delta n(x,z) = 4m\cos(q_{\perp}x)\cos(q_{\mathrm{II}}z)$, with $q_{\mathrm{II}} = q\cos(\alpha)$, and $q_{\perp} = q\sin(\alpha)$. The crystallographic axes of such a harmonic photonic crystal are $\pi(\pm 1/q_{||}, 1/q_{\perp})$, and the reciprocal lattice vectors of the photonic crystal are $\mathbf{q}_1$ and $\mathbf{q}_2$. We further assume for simplicity that the spatial period of the photonic crystal is significantly larger than the wavelength of the probe beam. This legitimatizes paraxial approximation for the description of propagation of the probe beams:

$$\left[2ik_0\partial/\partial z + \partial^2/\partial x^2 + 2\Delta n(x,z)k_0^2\right]A(x,z) = 0 \qquad (1.3.10)$$

Here $A(x, z)$ is the slowly varying complex envelope of the electromagnetic field in two-dimensional space $E(x,z,t) = A(x,z)e^{ik_0 z - i\omega_0 t}$ propagating along the $z$ direction with a wave number $k_0 = \omega_0/c$. Advantage of the use of paraxial approximation is a substantial simplification of the problem to the explicit analytical expressions in asymptotical cases. The disadvantage is that the treatment is restricted for the photonic crystal with the modulation period larger than the wavelength of the probe beam.

Analytical study of the propagation is performed by expanding the electromagnetic field into a set of spatially harmonic (Bloch) modes.

$$A(x,z) = \sum_{j,l} A_{j,l} e^{ik_{\perp,j}x + ik_{II,l}z} \qquad (1.3.11)$$

with $\mathbf{k}_{j,l} = (k_{\perp,j}, k_{||,l}) = (k_{\perp} + jq_{\perp}, k_{//} + lq_{||})$ , $j$ , $l$=...−2,−1,0,1,2,..., respectively. The expansion (1.3.11) results in a coupled system for the amplitudes of harmonics:

$$\left(-2k_0 k_{II,l} - k^2{}_{\perp,j}\right)A_{j,l} + 2mk_0^2 \sum_{r=j\pm1,\,p=l\pm1} A_{r,p} = 0 \qquad (1.3.12)$$

Solvability of Eq. (1.3.12) results in a transverse dispersion relation (the dependence of the longitudinal component $k_{\perp}$ on the transverse component $k_{||}$ of the wave vector). We restricted to the five most relevant harmonics in our study (respectively, nine components for three-dimensional case), consisting of a central component with the wave vector $\mathbf{k} = (k_{\perp}, k_{||})$, and four most relevant modulated (sideband) components with the wave vectors ( $k_{\perp} \pm jq_{\perp}$, $k_{||} \pm lq_{||}$), respectively. The transversal dispersion relations as calculated numerically

from Eq. (1.3.12) are given in Fig. 1.26. In the absence of refractive index modulation $m = 0$ the formal solution of Eq. (1.3.12) consists of a set of parabolas [dashed curves in Fig. 1.26, (a)] shifted one with respect to another by the vectors of photonic crystal lattice $\mathbf{q}_{1,2}$. These parabolas represent the transverse dispersion curves for uncoupled harmonic components of the expansion (1.3.10). For a nonparaxial description of light propagation these parabolas would be substituted by circles. The modulation of the refractive index $m \neq 0$ lifts the degeneracy at the crossing points and gives rise to band gaps in spatial wave number domain [Fig. 1.26(a)]. We focus on the appearance of plateaus on the transverse dispersion curves, indicating the vanishing of diffraction. For some particular parameters, essentially the geometry of photonic crystal given by vectors $\mathbf{q}_{1,2}$ and modulation depth m, the upper dispersion branch, corresponding to the most homogeneous Bloch mode (see insets of Fig. 1.26), can become nondiffractive, with zero curvature at $k_\perp = 0$ (Fig. 1.26 (b)). The insets of Fig. 1.26 show the field eigenfunctions at a particular propagation distance (the envelopes $A(x, z) = 0$)).

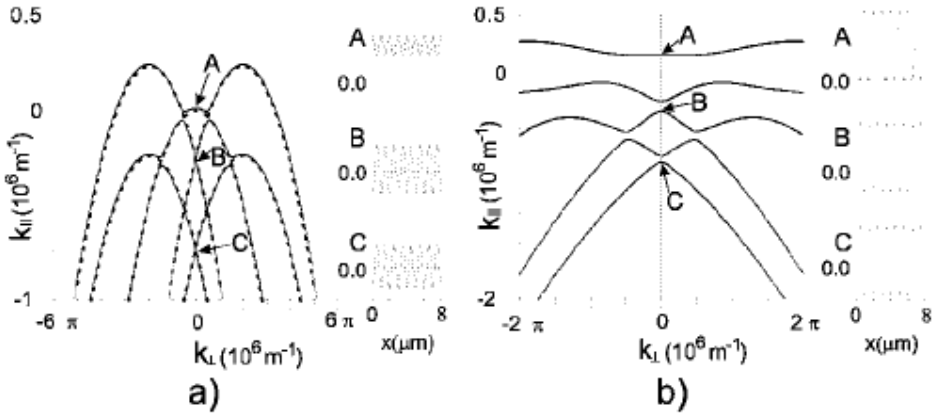


Fig. 1.26. Transverse dispersion relation obtained by numerical integration of Eq. (1.3.12) considering the five most relevant modes ($j$, $l = -1, 0, 1$): (a) in absence of modulation $m = 0$ (dashed parabolas), and for a weak modulation of refraction index $m = 0.003$ (solid line); and (b) for particular amplitude of modulation $m = 0.0175$ inducing zero diffraction. Insets show corresponding Bloch modes calculated at $k_\perp = 0$. Parameters: $\lambda = 500$ nm ($k_0 = 4\pi 10^6$ m$^{-1}$), $q_\perp = 2\pi 10^6$ m$^{-1}$, and $q_{||} = 0.75*10^6$ m$^{-1}$ [54].

Predicted phenomenon of nondiffractive propagation was checked by direct numerical integration of Eq. (1.3.10) for a two-dimensional modulation of refractive index (Fig. 1.27) and also for the three-dimensional case. The

integration shows an evident decrease of the diffraction: whereas in the absence of spatial modulation of the refractive index the narrow prove beam is diffractively broadening [Fig. 1.27 (a)], in the presence of refraction index grating of particular parameters the spreading was strongly suppressed [Fig. 1.27 (b)]. The magnified part of the nondiffractive propagation plot [Fig. 1.27 (e)] indicates that the nondiffractively propagating beam is in fact an envelope of the spatially modulated nondiffractive propagation mode. Calculations in the three-dimensional case result in essentially the same nondiffractive behavior as in two dimensional cases shown in Fig. 1.27.

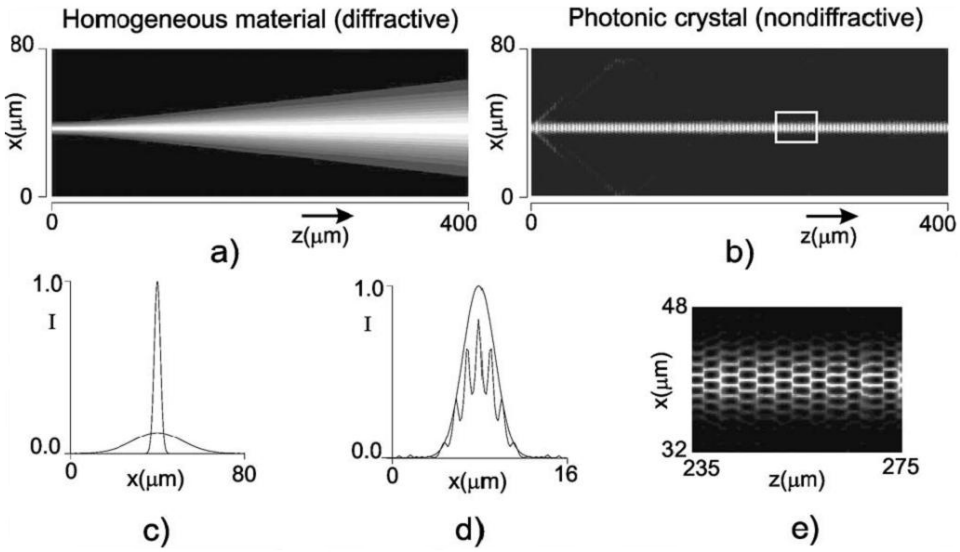


Fig. 1.27. Diffractive (a) and nondiffractive (b) propagation of a gaussian beam obtained by numerical integration of Eq. (1.3.10). (c) and (d) show initial and final envelopes of the beam (intensity), and (e) shows a magnified area from (b). The real world parameters: $\lambda = 500$ nm, $n_0 = 1$, $m = 0.0175$, $\lambda_{0\perp} = 1.0$ μm, and $\lambda_{0\|} = 7.0$ μm. The initial beam waist $W_0 = 2.82$ μm, with corresponding Rayleigh length: $z_0 = 50$ μm [54].

# 2. Optical Parametrical Oscillation in monolithic mini-cavities

Material related to this chapter was published in [A1-A4].

## 2.1. Introduction

Transverse pattern formation in broad aperture lasers and in other nonlinear optical resonators like photorefractive oscillators, and Optical Parametric Oscillators (OPOs) is attracting an increasing interest. The interest stems both: from the fundamental physical viewpoint, since the nonlinear optical systems are convenient systems for studies of self-organization and pattern formation in spatially extended systems; from the viewpoint of applications, since optical patterns have an application potential for parallel information processing, for image processing, nonlinear microscopy, and related topics. Pattern formation in nonlinear *micro-* and *mini-cavities* is especially attractive from the application viewpoint due to the compactness of the system.

Transverse patterns have been predicted to occur and observed in several different nonlinear optical systems (see e.g. [13] for a review). In the case of a quadratic nonlinear interaction patterns have been predicted in OPOs [57-59], in degenerate OPOs [16, 19, 60], and in second harmonic generation SHG [61-63]. Degenerate OPOs are particularly interesting due to the possibility of excitation of phase patterns [34, 36, 64], and of phase solitons [33]. Experimentally transverse patterns have been observed for OPOs [1-3], and for second harmonic generation [65]. No patterns have been seen for *degenerate* OPOs, or for OPOs in monolithic cavities.

## 2.2. Multiconical Emission of a monolithic mini-cavity Optical Parametric Oscillator

This chapter presents a step towards spatial pattern generation in degenerate OPOs: we show the linear and weakly-nonlinear stage of the pattern formation, i.e. the conical (off-axis) emission. It is known that conical emission is an essential ingredient of transverse pattern formation: the patterns occur due to the instability of a homogeneous (trivial - dark or nontrivial - bright) solution with respect to spatially modulated modes with the modulus of transverse wave-number $|k|$ depending on the resonator detuning. This means an off-axis (conical) emission with the cone angle depending on the detuning, which is a "weakly nonlinear" precursor of the nonlinear transverse patterns.

The experiments used a BBO type I crystal of size 5x5x1.7 mm, with the thickness 1.7 mm along the propagation direction. The phase matching direction for degenerate parametric down conversion at 532 nm is coincident with the optical axis of the cavity (crystal orientation angles are: $\theta = 22.8°$, and $\phi = 90°$). High-transmission coatings for 532 nm and high-reflection coatings for 1064 nm were used, resulting in a monolithic mini-cavity for subharmonic radiation. Fig. 2.1 shows experimentally recorded spectral characteristics of micro-cavity coatings for 1064 nm wave region. High reflectivity 94 % at 1064 nm results in finesse of the cavity $Q$ = 50. Spectral measurements show that degenerate operation at 1064 nm occurs, resulting in a higher threshold for nondegenerate operation.

The experimental scheme is shown in Fig. 2.2. The pump source is a Nd:YAG passively modulated laser, generating 1064 nm pulses of 13 ns duration, 5 mJ energy and $TEM_{00}$ spatial mode. Laser temporal profiles (Fig. 2.3) hints a single (or two near) longitudal mode operation. A Nd:YAG double pass amplifier enhances the energy of the pulses up to 50 mJ. The diameter of the beam is ~2 mm after reduction by a two lens telescope.

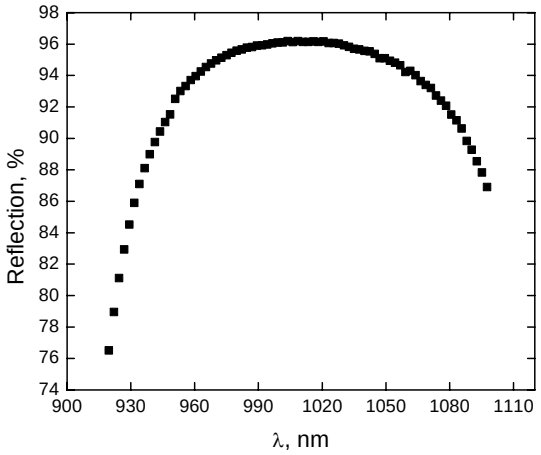


Fig. 2.1. Spectral characteristics of the coatings of the monolithic OPO mini-cavity.

The OPO pumping is performed by the second harmonic of the pump laser, generated in a DKDP type II crystal. A $\lambda/2$ wave plate is used for energy attenuation of the pump beam. After second harmonic generation the fundamental frequency is completely filtered, so no seed injection was present in the experiments. In the case of 13 ns pulse duration around 1000 resonant wave cavity round trips is possible in a 1.7 mm long BBO resonator. Q switching of the pump laser leads to emission with a small number of longitudinal modes (usually a single- or two neighboring longitudinal modes are emitted).

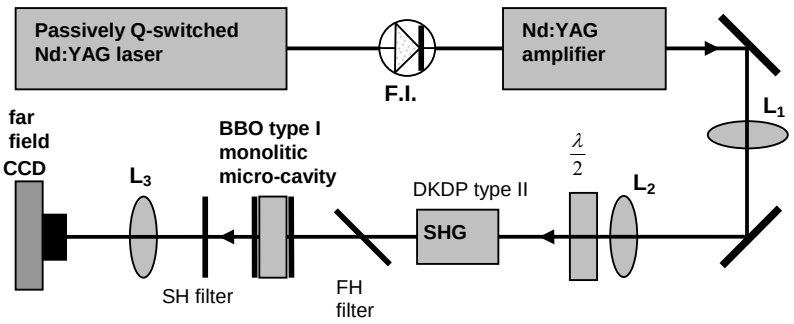


Fig. 2.2. Experimental scheme: F.I. - Faraday isolator; $L_1$, $L_2$ - telescope lenses; $L_3$ – far field imaging lens.

The mini-cavity orientation with respect to the pump beam can be changed in both directions. After passing the mini-cavity the pump beam is filtered out. A CCD camera and $f - f$ lens system was used for observation and recording of the OPO far-field pattern.

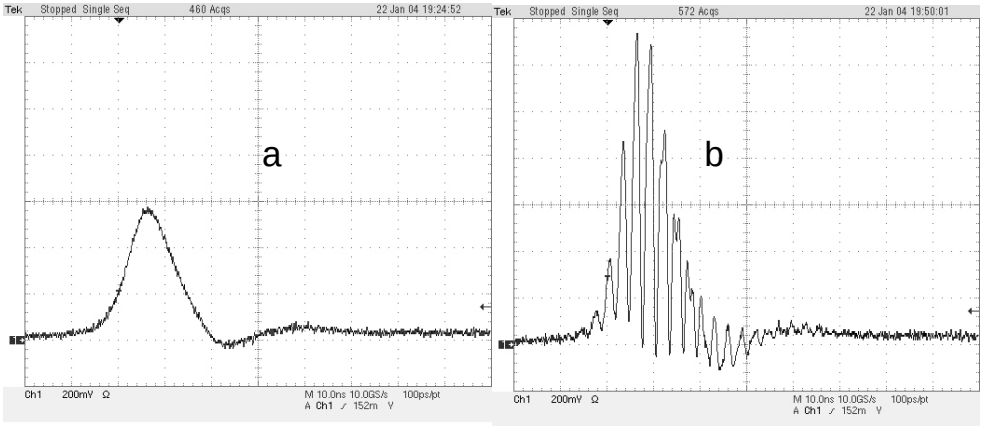


Fig 2.3 Laser pulse temporal profile. (a) – smooth shape appearing with 90% probability; (b) –modulated with two near longitudal laser modes.

First transmission of the cold resonator was measured by illuminating it with radiation at the sub-harmonic at $\lambda$ = 1064 nm in the absence of a pump beam. Transmission resonances were observed at some angles as shown in Fig. 2.4. The good separation of longitudinal modes (resonant rings) indicates relatively good finesse of the Fabry-Perot resonator, and certifies the above evaluated value of resonator finesse. An additional variation of the detuning (the cavity length) is possible by changing the temperature of the monolithic mini-cavity, resulting in variation of the radii of the concentric rings. Temperature change over 10 $^{o}$C corresponds to the change of the full cavity length by one $\lambda$, i.e. allows tuning over a free spectral range of the mini-cavity transmission.

In the case of a monolithic BBO mini-cavity only a few parameters can be varied for achieving optical parametrical oscillation: 1) cavity face plate orientation with respect to the direction of the pump beam in both directions: along the phase matching direction and transversally to it; and 2) cavity detuning through temperature induced crystal length change.

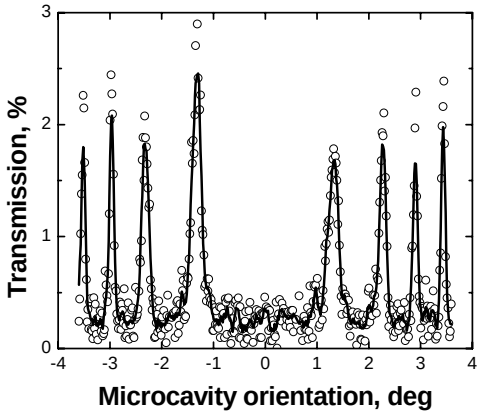


Fig. 2.4. Resonances of the cold cavity: an experimentally recorded transmission coefficient depending on a tilt of the cavity in one (of two possible) direction.

In this experiment we kept the cavity temperature constant. The BBO monolithic mini-cavity was pumped with 532 nm pulses of 10 mJ energy, and 13 ns duration. The pump beam diameter at the mini-cavity face plate was 2 mm. OPO radiation was observed for mini-cavity optical axes oriented at small 0.5-1.2 deg angles with respect to the pump beam in the phase matching direction. The lowest OPO threshold of 7 mJ per pulse at pump beam intensity 17 MW/cm$^2$ was observed for 0.75 deg incidence angle (OPO conversion efficiency to signal and idler waves for a 10 mJ pump pulse was 2.5 %).

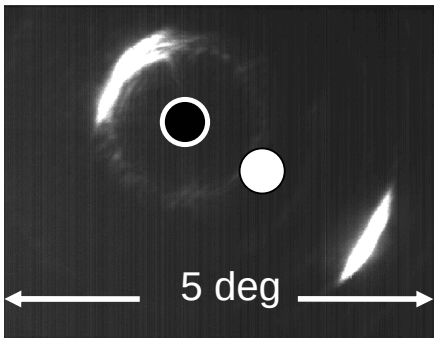


Fig. 2.5. Typical far field pattern of mini-cavity OPO emission. The empty spot indicates the direction of the mini-cavity optical axis, while the white spot indicates the direction of the pump.

Fig. 2.5 shows a typical far field OPO emission pattern. Signal and idler waves are always generated with a particular angle between them (conical

emission). The pump beam direction is always between the signal and idler waves. In this picture a faint pattern of cold cavity rings can also be observed.

The directions of the signal and idler waves and the angle of conical emission depend strongly on the mini-cavity orientation with respect to the pump beam as Fig. 2.6(a-d) shows. Fig. 2.6(a) shows the generation on one resonant cone; Fig. 2.6(b) indicates that two cone emission is possible. This generation pattern is very sensitive to cavity orientation in the phase matching direction, and is very weakly dependent on the pump energy, which indicates that the regime is quasi-linear.

When the mini-cavity orientation is changed in the non phase matching direction, then the signal and idler waves rotate around the direction of the pump beam (Fig. 2.6(e-h)). Here the mini-cavity orientation angle in the phase matching direction was fixed at a 0.75 deg angle. Our observations show that the signal and idler waves rotate around the pump beam direction by nearly 180 deg when the orientation is changed by $\pm 1$ deg. The OPO threshold increases when the mini-cavity orientation in the non phase matching direction exceeds 0.5 deg. At the value of 1 deg the OPO threshold energy rises from 7 mJ to 15 mJ. (36 MW/cm$^2$).

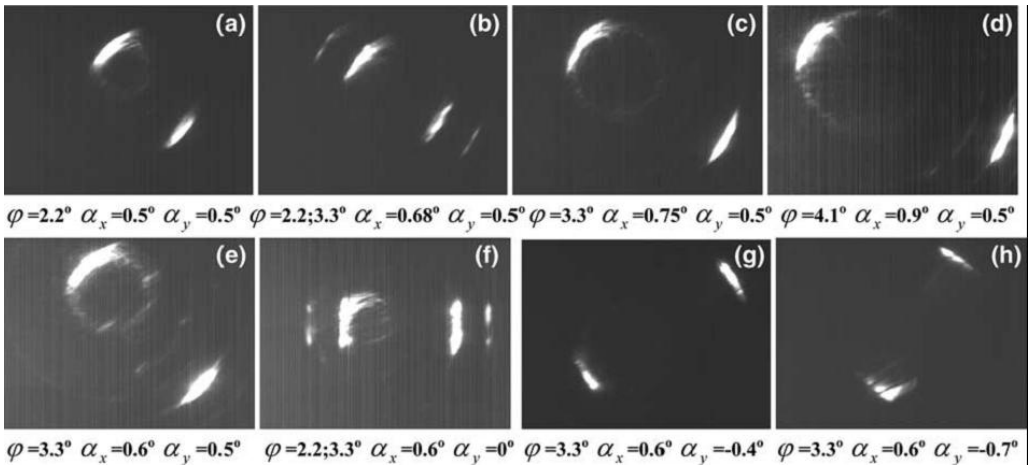


Fig. 2.6. Experimentally recorded far field pattern of DOPO. (a-d)– mini-cavity orientation as the pump beam is tilted in the phase-matching direction, (e-h) – in the non phase-matching direction. $\alpha_x$ - angle between coupling beam and cavity optical axes in phase matching direction, $\alpha_y$ - angle in non phase matching direction. $\varphi$ – angle between signal and idler waves.

## 2.3 Phenomenological interpretation of conical OPO emission

For a theoretical interpretation of the observed conical and multiconical patterns, we first describe the formation of the ring structure of the far field in the cold cavity. We assume that the OPO radiation resides on the resonant rings of the cavity in accordance with the theory of multiconical OPO emission in monolithic resonators [66], and based on this assumption we describe the formation of OPO patterns.

1) Resonant rings of the cold cavity: The intensity transmission coefficient (transparency) of the Fabry-Perot cavity is:

$$T = \frac{t_1 t_2}{1 + r_1 r_2 - 2\sqrt{r_1 r_2}\cos(\varphi)} \qquad (2.3.1)$$

where $r_{1,2}$ and $t_{1,2}$ are the reflection and transmission coefficients of the mirrors, calculated for the field amplitude (the intensity reflection and transmission coefficients are $R_i = r_i^2$, $T_i = t_i^2$ and $R_i + T_i = 1$). The resonator finesse is related with the cavity parameters via a standard definition $F = \pi (R_1 R_2)^{1/4} / \left(1 - \sqrt{R_1 R_2}\right)$, which in the limit of good cavity simplifies to $F \approx 2\pi / (T_1 + T_2)$. The $\varphi$ is the phase shift over full resonator roundtrip of a wave tilted at the angle $\alpha$ with respect to the optical axis of the cavity: $\varphi = \left(l\cos(\alpha) - l_0\right) \cdot 2\pi / \lambda$. $l$ is the full length of the cavity, $l_0$ is the full resonant length of the cavity, and $\lambda$ is the wavelength. (2.3.1) results in a well know ring structure (Fresnel rings) of the large aspect ratio resonators. Fig. 2.7 shows the ring structure as following from (2.3.1), and taking into account parameters of the cavity used in experiments: we use the value of the full cavity length $l$ in (1) as directly taken from experiments, and we choose the resonant cavity length $l_0$ by matching the radii of the inner resonant ring in experimental observations and in numerical calculations. The rough interpretation of the experimentally observed patterns is illustrated in Fig. 2.7. We fix, for simplicity the origin of the coordinate system with the direction of the optical

axis of the resonator, but vary the angle of the pump $\boldsymbol{\alpha}_0 = (\alpha_{0,x}, \alpha_{0,y})$ in both x, and y, directions, which correspond to the direction along and transversally to the direction of phase matching.

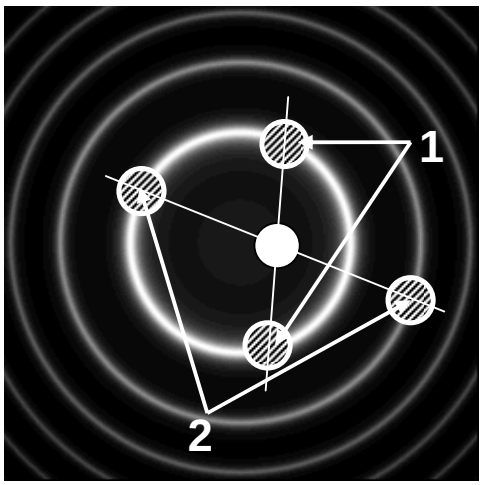


Fig.2.7. Ring structure of a cold cavity. The white spot indicates direction of the pump beam, and the pairs of symmetrically (with respect to the pump direction) placed pattern spots illustrate possible directions of the OPO generation. The pair 1 illustrates OPO generation on the same (first) ring, the pair 2 – on two different rings. The ring density is inverse proportional to the full cavity length, and the radius of the inner ring depends on the off-resonance detuning.

The OPO emission is determined essentially by three conditions:

1) by the resonance conditions for the mini-resonators (multicones with respect to the optical axis of the resonator) as described by (2.3.1), which means that the emission should reside on the resonant rings.

2) by the phase momentum conservation condition, which means that the emission in the far field domain must be symmetric with respect to the direction of the pump.

3) by the phase matching condition.

The pattern spots, as shown in Fig. 2.7, indicate the direction of OPO generation. It is obvious from this illustration that the fulfilment of the above conditions results in a complicated angular structure of the OPO generation.

Mathematically the total gain of the OPO in the linear regime is given by:

$$g(\boldsymbol{\alpha}_{1,2}) = -\frac{\beta_1(\boldsymbol{\alpha}_1) + \beta_2(\boldsymbol{\alpha}_2)}{2} + \sqrt{\gamma(\boldsymbol{\alpha}_{1,2})^2 + \frac{(\beta_1(\boldsymbol{\alpha}_1) - \beta_2(\boldsymbol{\alpha}_2))^2}{2}} \qquad (2.3.2)$$

as easily obtained from solution of equations describing parametric gain in lossy media (see e.g. [67] ). Here $\beta_{1,2}(\boldsymbol{\alpha}_{1,2})$ are the coefficients of the losses for both generated waves depending on their angles (corresponding to the resonant ring structure – see condition 1), and $\gamma(\boldsymbol{\alpha}_{1,2})$ is the gain coefficient, which is dependent on the angles of both generated waves (the cone of phase matching in the case of vectorial synchronism – see condition 3). For a strong gain $\gamma >> \beta_{1,2}$ (2.3.2) simplifies to $g(\boldsymbol{\alpha}_{1,2}) = \gamma(\boldsymbol{\alpha}_{1,2}) - (\beta_1(\boldsymbol{\alpha}_1) + \beta_2(\boldsymbol{\alpha}_2))/2$. The coefficients of losses follow directly from (2.3.1). Next we take into account the momentum conservation condition with respect to the direction of pump beam. If we assume that the pump beam is a plane wave (spatial $\delta$ – function in the far field domain) then the emission angles of both waves $\boldsymbol{\alpha}_{1,2}$ fulfil: $\boldsymbol{\alpha}_1 + \boldsymbol{\alpha}_2 = 2\boldsymbol{\alpha}_0$. This allows to eliminate one angle (say $\boldsymbol{\alpha}_2$) from (2.3.2). Finally introducing (e.g. phenomenologically) the expression of the phase matching $\gamma(\boldsymbol{\alpha}_{1,2})$ one obtains an analytical expression for the direction of the OPO generation $\boldsymbol{\alpha}_1$. The resulting analytical expression for the angular distribution of OPO radiation in the far-field is cumbersome, and we do not give it here. Instead we plot the intensity distributions predicted by the formula in Fig. 2.8.

Qualitatively the correspondence between experimentally observed (Fig. 2.6) and numerically obtained (Fig. 2.8) distributions is good. The conical emission angle varies with the angle of the pump by varying the pump angle in the phase matching direction (by varying the phase matching cone angle phenomenologically) as shown in series (a - d). Also the far field patterns rotate by varying the pump angle in the direction perpendicular to the phase matching direction, as shown in series (e - h). Typically upon varying the pump angle, the radial and the azimuthal emission angles vary smoothly, before they jump abruptly to new locations. The quantitative correspondence between the far-field distributions for different angles between the pump wave and the optical axis of the resonator is also good.

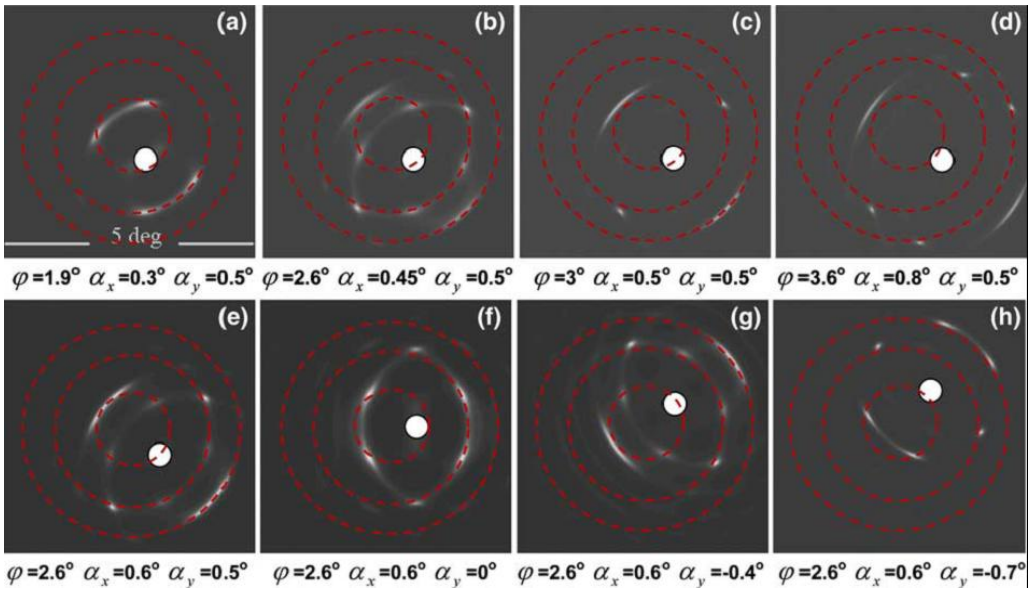


Fig. 2.8. Simulated OPO far field pattern. Resonator detuning $\Delta = 0.2$ (as normalized to free spectral range), finesse $Q = 50$, gain $\gamma = 5$ (as calculated for the photon propagation length in a cold cavity), $\varphi$ - the phase matching angle of OPO emission; $\alpha_x$ - angle between coupling beam and cavity optical axes in phase matching direction, $\alpha_y$ - angle in non phase matching direction. Dashed concentric rings indicate the resonance rings of the cold cavity.

## 2.4 Non-mean-field theoretical interpretation for OPO

Most of the theoretical - numerical studies on transverse patterns in nonlinear optics consider mean field approximation, which means equivalently a single longitudinal mode assumption. Within this assumption the emission of a spatially extended system evolves on a resonant ring in the far field domain with the ring radius dependent on the detuning on the resonator: $k_\perp^2 = 2|\mathbf{k}|(\omega - \omega_0)/c$, where $k_\perp$ is the transverse wave-number of the emitted radiation, $|\mathbf{k}| = \omega/c$, $\omega$ is the gain frequency (atomic gain frequency in lasers, half-pump-frequency for degenerate OPOs, and the frequency of injection in passive systems), $\omega_0$ is the eigenfrequency of the (closest) longitudinal mode of the resonator, and $c$ is the velocity of light in material. Therefore the off-axis (conical) emission with the cone angle depending on the detuning is a "weakly nonlinear" precursor of the nonlinear transverse patterns. The basic mechanism

of the "essentially nonlinear" pattern formation in lasers is the tilted wave selection, i.e. a selection of one or several waves from those allowed by the above resonant ring condition [68]. Analogously the basic mechanism of the essentially nonlinear" pattern formation in degenerate OPOs is the stripe pattern selection with the spatial Fourier components lying on the resonant ring [16, 58, 59, 69].

Simple geometrical interpretation of the conical emission is that if the modulus of the wave-vector of the generated radiation $\mathbf{k}$ is larger than that of the resonant one $|\mathbf{k}| > k_n$ ($k_n = 2\pi n/L$ is the wave-number corresponding to the nearest longitudinal mode of the resonator of length $L$), then the radiation is emitted at some angle in order to match the resonance condition: $k_\perp^2 = |\mathbf{k}|^2 - k_n^2$. Assuming, however, that several longitudinal modes can be excited with $k_{n-j} = 2\pi(n-j)/L$ $j$=0, 1, 2,… the multi-conical emission can be expected, with $k_{\perp,j}^2 = |\mathbf{k}|^2 - k_{n-j}^2$. Theoretically the multi-conical emission for OPOs was predicted in [66]. Experimentally nonlinear multiconical patterns were never observed in OPOs, however were observed in a related system - Photorefractive Oscillators [27, 70]. We report here the results of our study of multiconical emission of monolithical OPOs: 1) we present the results of numerical study based on numerical integration of OPO equations without using the mean field approximation; 2) we give the experimental evidence of multiconical emission.

Theoretical study is based on the non-mean-field model of a degenerate OPO, introduced e.g. in [22]:

$$\left(\frac{\partial}{\partial z} + \frac{1}{c}\frac{\partial}{\partial t}\right)A_1 = -i\frac{\Delta k}{2} + \sigma A_0 A_1^* + id_1\nabla_\perp^2 A_1 \qquad (2.4.1.a)$$

$$\left(\frac{\partial}{\partial z} + \frac{1}{c}\frac{\partial}{\partial t}\right)A_0 = -\frac{\sigma}{2}A_1^2 + id_0\nabla_\perp^2 A_0 \qquad (2.4.1.b)$$

for the slowly varying complex envelopes of the subharmonic $A_1(x,y,z,t)$ and pump $A_0(x,y,z,t)$ waves propagating along the longitudinal direction $z$, and diffracting in the transverse space: $\nabla_\perp^2 = \left(\partial^2/\partial x^2 + \partial^2/\partial y^2\right)$ with the diffraction coefficients $d_i = 1/(2k_i)$. The phase mismatch $\Delta k$ in the present study is set to zero, assuming a phase matched interaction for simplicity. Equations (2.4.1) are coupled with the boundary conditions:

$$A_1(x,y,z=0,t) = A_1(x,y,z=L,t)\cdot r\cdot e^{i\Delta\varphi} \qquad (2.4.2.a)$$

$$A_0(x,y,z=0,t) = E \qquad (2.4.2.b)$$

where $r$ is the reflectivity of the output mirror (assuming 100 % reflectivity for subharmonics of input mirror), $L$ is the full resonator length, $\Delta\varphi = kL$ is the phase mismatch over the resonator roundtrip, and $E$ is the intensity of the pump wave entering into the resonator. The boundary condition Eq. (2.4.2.a) means, that subharmonic field $A_1(x,y,z,t)$ reflects from the input mirror instantaneously (with no delay).

We integrated Eq. (2.4.1) using a split step technique, i.e. integrating the nonlinear part in the space domain and the diffractive part in the spatial wave-vector (Fourier) domain on a grid of ($n_x$, $n_y$, $n_z$) = (256,256,128). Typical numerical results are shown in Fig. 2.9. Two stages of the evolution of spatial patterns can be distinguished:

1) a weakly nonlinear stage, characterized by formation of multiple ring structure in the far field, with the radius of the inner ring depending on the detuning of the resonator $\Delta\varphi = kL$ (see Fig. 2.4.1(a) and (b) illustrating the patterns for different values of the detuning). The near field (intensity as well as the phase) looks completely irregular at that stage.

2) an essentially nonlinear stage, characterized by a further selection of radiation modes belonging to the different, as well as on the same resonant rings. The nonlinear patterns are very different for different detunings.

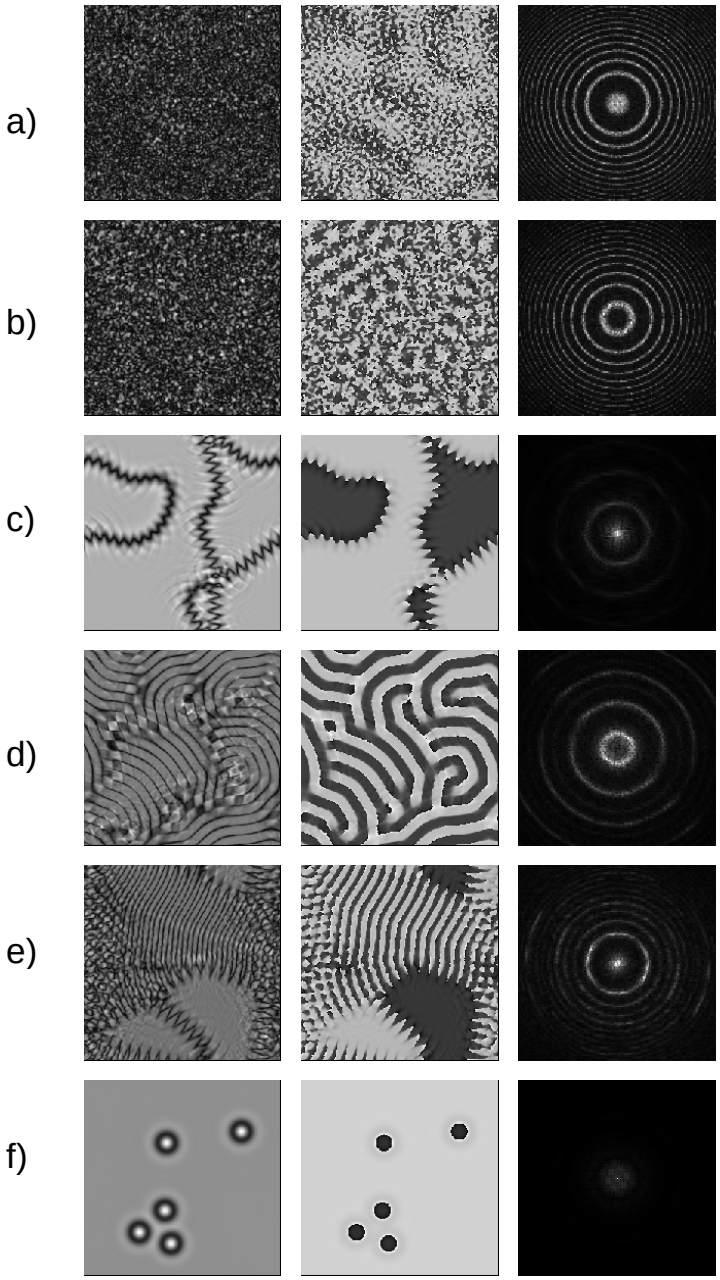


**Fig.2.9.** Transverse patterns in multi-longitudinal-mode OPOs, as obtained by numerical integration of Eq. (2.4.1). Intensity distributions of subharmonic field (near field) on the left, phase of the field (grayness corresponds to phase ranging from 0 to $2\pi$) at the middle, and intensity distribution in spatial Fourier domain (far field) on the right. Parameters used in integration: total losses of the resonator: $r = 0.95$ (resonator finesse $Q = 62$), unsaturated gain per resonator roundtrip: $\sigma EL = 0.5$, Fresnel number of the resonator for subharmonics: $F = a^2/(\lambda L) = a^2/(4\pi d_1 L) = 400$ ($a$ is the transverse size of integration window with periodic boundary conditions). Integration is performed on the grid 256*256 in transverse space and 128 in longitudinal direction. Cases (a) and (b) correspond to the linear stage of pattern evolution with the number of roundtrips $n_{roundtrip} = 10$, and cases (c), (d), (e) and (f) to the nonlinear stage with $n_{roundtrip} = 200$. Cavity detuning: (a) and (c) $\Delta\varphi = 0$, (b) and (d) $\Delta\varphi = 0.75$, e) $\Delta\varphi = 3$, and (f) $\Delta\varphi = 0.3$;

For small detuning the zigzagged phase domains can appear, where zigzagging is due to coexistence of the radiation on two different resonant rings (different space scales) (Fig. 2.9(c)). For moderate detuning the locking between spatial field harmonics on different resonant rings can occurs, leading e.g. to stripes with pronounced high harmonics (flat top stripes) (Fig. 2.9(d)). At some values of detuning a competition between the different resonant rings can occur, leading to spatial separation of radiation on different longitudinal modes (Fig. 2.9(e)). In the latter case the patterns with two different spatial scales are clearly visible. Apart from above listed patterns, which are typical for multi-longitudinal-mode case, the patterns analogous to those predicted by mean field theories are also observed. Fig. 2.9(f) is one such example: it shows phase (or dark ring) solitons (Fig. 2.9(e)) whose analogs have been found in mean field approximation [33].

## 2.5. Experimental attempt to observe transverse near field patterns in OPO

Experiments in this chapter presents attempt to observe near field transverse patterns in OPO. Experimental setup is very much close to one discussed in previous chapter 2.2. The main technical difference was a better quality BBO type I crystal of size 5x5x1.5 mm, with the thickness 1.5 mm along the propagation direction and 2f – 2f lens imaging system for near field recording (Fig. 2.30). The BBO monolithic mini-cavity was pumped with 532 nm pulses of 10 mJ energy. The pump beam diameter at the mini-cavity face plate was 2 mm.

Fig. 2.31 shows a typical near field OPO emission pattern. First of all the quality of the monolithic crystal was not ideal: several defects, in bulk as well as on the surface, were present resulting in distorted near field distributions (white spot surrounded by concentric rings).

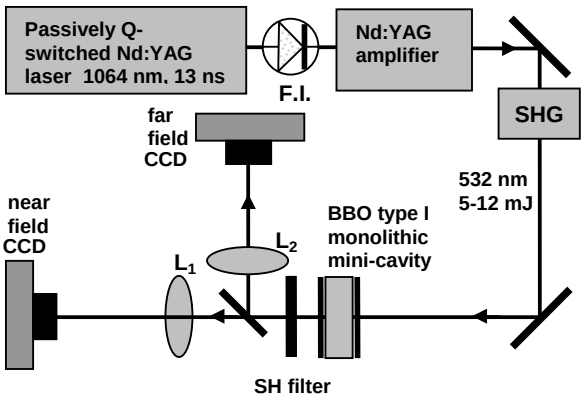


Fig. 2.30. Experimental scheme: F.I. - Faraday isolator; $L_1$ - 2f – 2f near field imaging lens; $L_2$ – f - f far field imaging lens.

These defects limit severely the ability to observe theoretically predicted patterns, however several signatures of theoretically predicted multi-longitudinal-mode patterns can be identified. The coexistence of stripes with different spatial scales is observed.

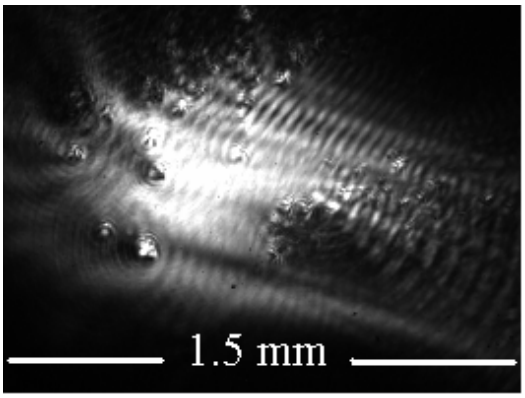


Fig. 2.31. Typical near field pattern of mini-cavity OPO emission.

## 2.6 Stripe Patterns in Degenerate Optical Parametric Oscillators

Stripe (or roll-) patterns appear in a variety of spatially extended systems in Nature, like ripples of sand, or markings of the skins of the animals, and also in variety of laboratory systems, like in Rayleigh-Benard convection [71], or Taylor-Couette flows [72]. Stripe patterns were predicted to occur also in nonlinear optical systems, such as degenerate optical parametric oscillators

(OPOs) [16, 73], and degenerate four wave mixing [19]. In the latter system the stripe patterns were observed experimentally [37]. Despite the large variety of pattern forming systems, a universal description of stripe patterns is possible. Universal features of stripe pattern dynamics (e.g. the zig-zag or Eckhaus instabilities) are well known, as investigated on universal model equations: on the Swift-Hohenberg equation as an order parameter equation for stripes in spatially isotropic system [74], or on the Newell-Whitehead-Segel equation as an amplitude equation for perturbations of stripe patterns [75, 76].

In spite of many theoretical-numerical works on stripes in degenerate OPOs, and some experimental attempts [10], the stripes have never been convincingly observed experimentally up to now. There are several reasons for the difficulties to observe those predicted patterns: i) the theoretical models usually consider single-longitudinal-mode approach, whereas the real systems are the multi-longitudinal-mode ones. In multi-longitudinal mode case the system is no more two-dimensional (two transversal dimensions plus time) but rather three-dimensional one (with additionally the longitudinal space coordinate involved). The basic three dimensional OPOs patterns are not stripes but the lamellae patterns [11], which however can be tilted arbitrarily in space (as illustrated by a pair of empty circles in Fig. 2.32). The tilted lamellae pattern in 3D results in a moving 2D stripe in output radiation, what results in the homogeneous spatial distributions in the averaged (in time) observations; ii) the stripes, even belonging to the same longitudinal mode (denoted by a pair of filled circles in Fig. 1) drift in space as driven by quantum and technical noise, which in average smears the observed pattern. We solved these both problems by using the short (millimeter length) cavities, which allowed to increase substantially the frequency separation between the longitudinal modes (free spectral range). We also used a weak injection at the frequency of subharmonics, which allowed to fix the position and the 2D stripes (orientation of the 3D lamellae), and thus make them observable. In this way we were able

to observe experimentally the stripe pattern for the degenerate OPOs for the first time, what is the first key result reported in the present paragraph.

Another key result reported here is the observation of unusual properties of the temporal spectra of the signal emitted by the broad aperture degenerate OPO. Usually the OPOs have a Lorenzian profile of temporal spectra. This is related with the resonance line of the driven oscillator universally (independently on the physical system) showing a Lorenzian profile, with the asymptotic decay law $|\omega-\omega_{rez}|^{-2}$ (for the frequencies sufficiently far from the resonance). The emission spectra reported here however show the character of decay more similar to the $|\omega-\omega_{rez}|^{-1}$ law, i.e. the so called 1/f noise. The 1/f-, or "flicker" noise is found that many different kinds of systems, from physics, technology, biology, astrophysics, geophysics and sociology, where the power spectra show $f^{-\alpha}$ dependence, with $\alpha$ around one, i.e. $0.5 \le \alpha \le 1.5$ [77-79].

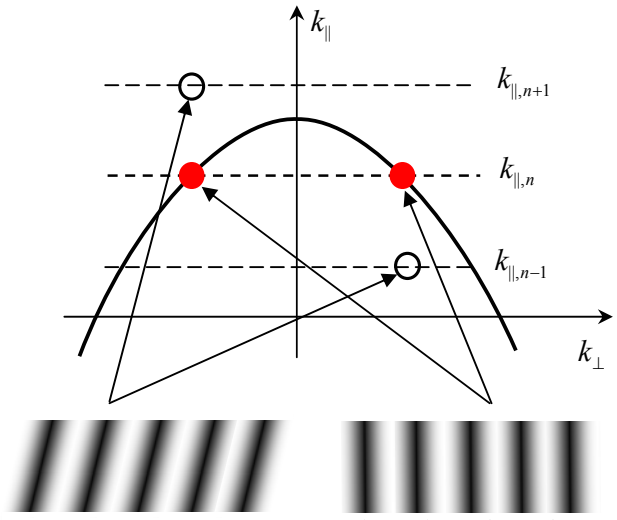


Fig. 2.32. Illustration of pattern formation in degenerate OPOs. Parabola depicts the spatial dispersion curve (dependence of the longitudinal component of the wavenumber $k_{\|}$ on the transversal one $k_{\perp}$) for a given (subharmonic) frequency. The resonator tuning leads to the vertical shift of the modes (dashed lines) and result in the of axis emission (filled circles on parabola) which leads to stripe formation. However, in addition to degenerate stripes, the nondegenerate stripes are also possible (a pair of empty circles) with frequencies shifted by $\pm\Delta\omega, \pm 2\Delta\omega \ldots$. The insets illustrate the forward-propagating field configuration in resonator.

The presence of the 1/f noise has been recently related with the presence of the spatial degrees of freedom in the system [80]. In particular the 1/f noise was predicted for condensates described by a stochastic Ginzburg-Landau equation, where the dependence of the exponent $\alpha$ on the dimension of space D was derived to be $\alpha = 1 + (2 - D)/2$.

The results were also extended to the stripe patterns leading to essentially the same dependence of power exponent on the dimensionality of the system [81]. We interpret experimentally observed 1/f-like spectra basing on these models, as well as on numerical integration of the corresponding equations.

The basis of experiment is OPO in a monolithic plane mini-cavity in the presence of week injection. The detailed experiment scheme (without the injection) is described in paragraph 2.2. The main technical difference is a better quality BBO type I crystal of size 5x5x1.5 mm, with the thickness 1.5 mm along the propagation direction. Additionally to the experiment scheme described in paragraph 2.2 seed injection (0.2 mJ) can be added for optical parametrical amplification OPA process observation (Fig. 2.33). A CCD cameras were used for simultaneous observation and recording of the OPO far-field and near-field patterns. Spectrometer “Avantes AvaSpec-2048“ was used for OPA emission temporal spectrum recording.

In the absence of injection the collinear OPO generation was obtained for the mini-cavity orientation to pump beam at 0.7 deg in phase matching direction. By tuning the resonator (by means of temperature and cavity orientation) the off-axis emission in the far field was achieved. The radiation in the far field consists of two spots placed symmetrically with respect to the pump direction (Fig. 2.34(b)), with the tunable distance between the spots.

According to common opinion this far-field distribution should correspond to the stripe pattern in the near fields, however no stripes were observed. The near field distribution was always obtained nearly homogeneous (Fig. 2.34(a)). Moreover the spectral analysis of the subharmonics radiation showed broad

spectra, centered around the subharmonics frequency, however with no sign of locking to the degenerate regime.

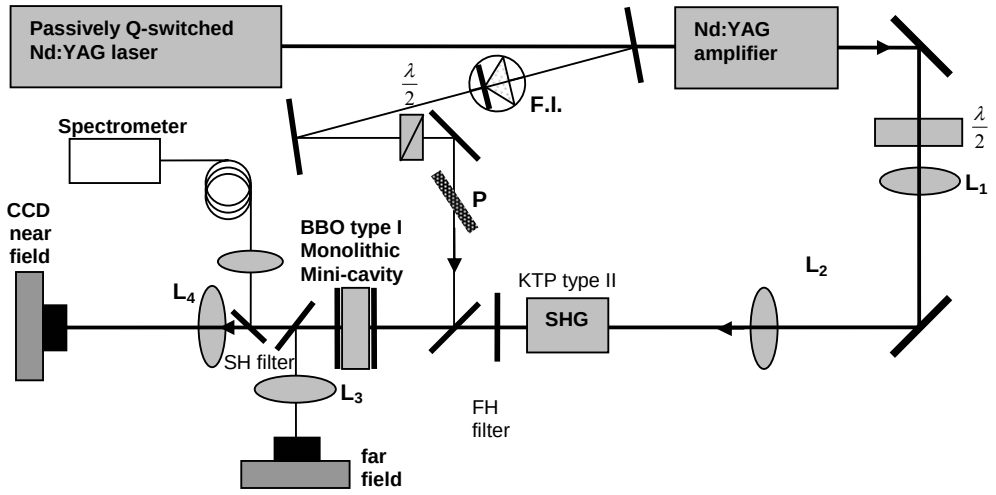


Fig. 2.33. Experimental scheme: F.I. - Faraday isolator; $L_1$, $L_2$ - telescope lenses; $L_3$ – far field imaging lens; $L_4$ – near field imaging lens.

These (negative) observations hinted on the necessity to revisit the theory of the process of locking to degeneracy for broad aperture OPOs. The locking process is a well established fact for the zero-dimensional systems, i.e for the systems with the evolution occurring in time, but not in space. We perform therefore here the analysis on the governing equations of broad aperture degenerate OPO, which in the presence of spatial degrees of freedom, as described by parametrically driven Ginzburg-Landau equation (PDGLE) [3,4]:

$$\frac{\partial A}{\partial t} = -A + \gamma A^* - |A|^2 A + i\Delta A + i\nabla^2 A \qquad (2.6.1)$$

Here the complex-valued order parameter $A(\mathbf{r},t)$, which is proportional to the slowly varying envelope of the electric field, is defined in D-dimensional space $\mathbf{r}$ (space coordinates are normalized to convert the diffraction coefficient to unity), and evolving in time $t$ (time is normalized to photon life-time in the cold cavity). $\gamma$ is normalized parametric gain coefficient (threshold at $\gamma = 1$), $\Delta$ is the detuning parameter, determining the resonant transverse wavenumber of the stripe pattern $\mathbf{k}_0$: $\mathbf{k}_0^2 = \Delta$,

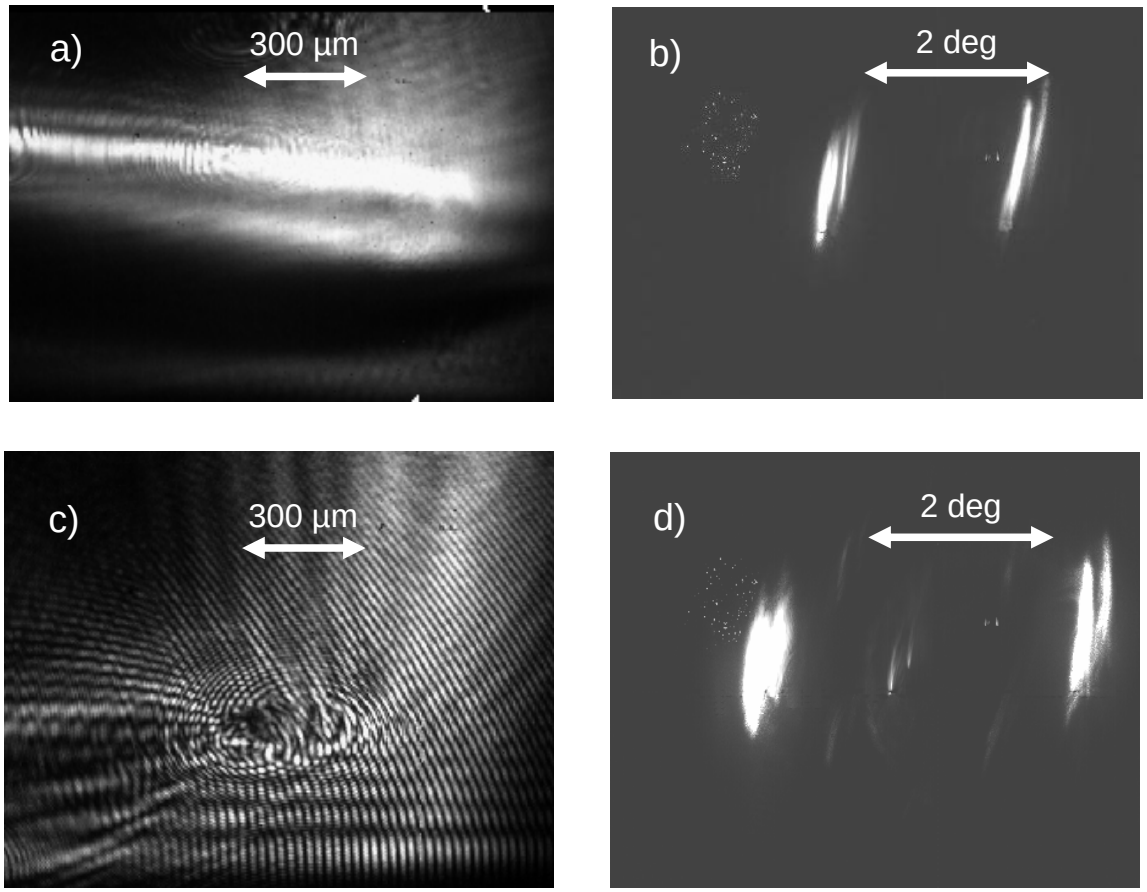


Fig. 2.34. Experimentally observed stripe pattern in OPO without injection (a, b) and with week injection (c, d) in the near field (a, c) and the far field (b, d). The "doubled" character of the far fields is the experimental artifact.

In the absence of special degrees of freedom $\nabla^2 \to 0$ and for the zero detuning $\Delta = 0$, locking to the degenerate regimes occurs as the linear stability of (2.6.1) analysis shows. One searches for a solution in form $A(t) = a_+(t)\exp(i\omega t) + a_-(t)\exp(-i\omega t)$, and looks for its exponential growth $a_\pm(t) \propto \exp(\lambda t)$. For $|\omega| >> 1$ the growth exponents are (as follows from the linear stability analysis of (1)): $\lambda_{1,2} = -1 \pm \gamma$. However for $|\omega| << 1$, when the parametric interaction of the each wave by itself is sensible (taking into account the terms $da_+(t)/dt = ... + \gamma a_+^*(t)\exp(-2i\omega t)...$ and $da_-(t)/dt = ... + \gamma a_-^*(t)\exp(2i\omega t)...$ in the linear stability analysis), and the growth exponents are: $\lambda_1 = -1$ and $\lambda_2 = -1 + 2\gamma$. As the expressions for $\lambda_2$ indicate, the parametric gain at the degenerate frequency is double to that at the

nondegenerate frequencies. Physically this means that the close-to-degeneracy frequency components of quantum noise with $|\omega| \le 1$ amplify two-times stronger than those far from degeneracy This is the locking mechanism responsible for that the degenerate frequency components win the competition against the nondegenerate components.

For the stripe patterns the above locking-to-degeneracy mechanism is absent. Indeed, the linear stability analysis of (2.6.1) with respect to the resonant stripes $A(t) = a_+(t)\exp(i\omega t + i\mathbf{k}_0\mathbf{r}) + a_-(t)\exp(-i\omega t - i\mathbf{k}_0\mathbf{r})$ with $\mathbf{k}_0^2 = \Delta$ shows that the parametric self-coupling term is always absent for $|\omega| << 1$. The spatial dependence (the modulation with the wavevector $\mathbf{k}_0$) removes totally the mechanism of the frequency locking. This means that for the stripe patterns the degeneracy has no physical sense, since all frequency components are amplifying equally, and each component can win the competition. Also that the radiation frequencies can drift randomly at around the degeneracy frequency, as driven by quantum or technical noise.

The above analysis implies a need to seek for another locking-to-degeneracy mechanism in order to observe experimentally the stripes, as the mechanism of intrinsic locking does not work. We applied therefore a week injection at the subharmonic frequency to ensure the "external" locking to degeneracy. We prepared the injection radiation from the pump laser (taking a part of its radiation (0.2 mJ) before the second harmonic generator and expanding beam diameter in order to match OPO mini-cavity aperture 6 mm). With the injection the stripe pattern was observed in near field image (Fig 2.34(c)). Fig. 2.34(d) shows the far field of the OPO emission. Weak point in the center indicates transmitted injection which is collinear with a pump. Signal and idler waves reside symmetrically with respect to the pump (and injection) in the far field. Although the far field with injection visually does not differ much from the one without injection – the near field distributions differ dramatically. The formation of stripes in presence of injection is evident.

Finally, we recorded temporal spectra by taking a part of the OPO emission and focusing it into a spectrometer fiber through a diffuser. A pronounced peak at subharmonic frequency (Fig. 2.35) also evidences the locking to degeneracy. In addition, we observe that the decay of the spectra follows the power law $|f - f_{rez}|^{-\alpha}$, with the exponent α varying in the range between 0.5 and 1 and asymptotically approaching 0.5. The observations of spectra qualitatively agree with [80, 81], which state that the presence of the spatial degrees of freedom results in the $1/f$-like spectra with the power exponent $\alpha \approx 1$, whereas in the absence of spatial degrees of freedom $\alpha = 2$. In the presence of spatial degrees of freedom, one has a continuum of oscillators of different eigenfrequencies (spatial modes with the different transverse wavenumbers $\vec{k}_0$). The summation over modes (integration over wavenumbers $\vec{k}_0$) results in $\alpha \approx 1$. Leaving the detailed analysis of the $1/f$ character of the spectra, we note that the very fact of its observation indicates that we observe the spatial patterns, and not the discrete transverse modes, according to the theory [80, 81].

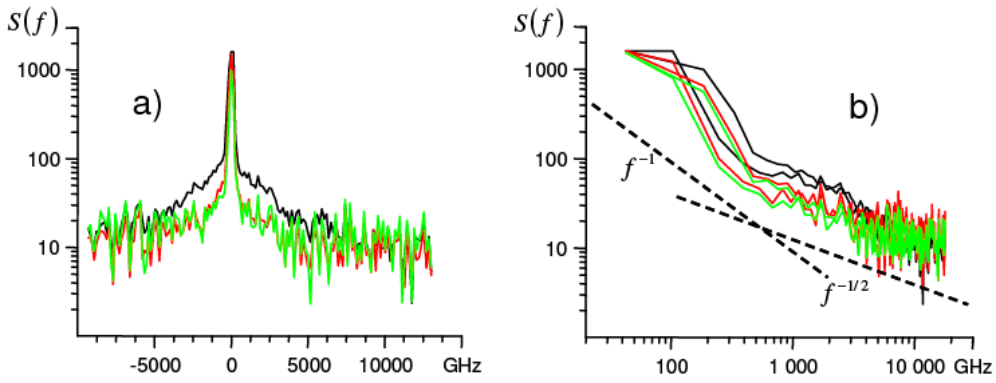


Fig. 2.35. Experimentally recorded temporal spectra in OPO with week injection: (a) linear-log scale and (b) log-log scale. The dashed lines indicate $f^{-1}$ and $f^{-1/2}$ power laws. The log-log spectra contain the right part as well as the mirror-reflected left part of spectra (with respect to subharmonics frequencies) for three realizations.

## 2.7 Conclusions

- We demonstrated OPO generation in a monolithic BBO type I crystal mini-cavity. We show that OPO emission in a monolithic mini-cavity is conical and multiconical, so signal and idler wave directions depend on cavity detuning to laser frequency, phase matching cone and cavity orientation with respect to the pump beam. This allows the OPO emission direction to be controlled by changing the mini-cavity orientation, by temperature changes or by laser frequency change. In the case of external monolithic mini-cavity refractive index change, or external phase matching condition change, the OPO emission angles can be modulated or attenuated (external electric field or external light induced refractive index change). We expect that OPO far field control is also possible for a non-monolithic cavity, although the monolithic mini-cavity is attractive for compactness and stability of the cavity alignment.
- We demonstrate experimentally the stripe patterns in broad aperture optical parametric oscillators in plane mirror mini-cavities for the first time. We highlight the absence of the intrinsic locking-to-degeneracy mechanism for the spatially dependent systems. We achieve the stabilization of the stripes by a week injection at subharmonic frequency. Finally we measure the temporal spectra and obtain the 1/f like spectra in qualitative accordance with the theories of the noise-spectra in the spatially extended systems.

# 3. Resonators with Intracavity Photonic Crystals

Material related to this chapter was published in [A5-A6].

## 3.1. Introduction

Photonic crystals (PhCs), the materials with periodic in space refraction index, is an object of intensive study since their proposal in 1987 [38, 82]. The studies were focused initially on the *temporal* dispersion characteristics of the PhCs. It was discovered that the dispersion curves strongly depend on the periodic modulation of refraction index, and demonstrate a band structure - a most celebrated feature of the PhCs. More recently it was found that the *spatial* dispersion (diffraction) characteristics also vary substantially in periodic materials: the diffraction can become negative [48, 49], or can vanish to zero [50-54], resulting in the so-called self-collimation effect in the latter case.

Diffraction manipulation affects primarily the linear propagation of light beams in bulk PhCs [48-54] However, diffraction manipulation can also create phenomena in more complicated systems based on PhCs. In particular, the periodic index modulation in Kerr-nonlinear materials leads to the nonlinear formation of light field, such as band gap solitons [83], subdiffractive solitons [84], and others. Periodic index modulation in quadratic nonlinear materials leads to modification of the spatial phase matching profile [85]. The present work is based on the idea that the periodic modulation of the refractive index can also substantially alter the properties of the *resonator* filled by such material. The transverse and longitudidal mode structure as well as the angular transmission profile are (strongly) dependent on diffractive characteristics of resonator. Manipulation of diffractive characteristics leads to changes of mode and angular transmission profiles.

### 3.1.1. Spatial dispersion curves of PhC resonator

The transverse and longitudinal mode structure of homogeneous plane-mirror (Fabry-Perrot) resonators are well known. Fig. 3.1(a) illustrates formation of the resonator modes for the monochromatic radiation of frequency $\omega$ (and correspondingly of the modulus of the wave-vector $|\mathbf{k}| = \omega/c = 2\pi/\lambda$). As the presence of the resonator imposes conditions on the longitudinal component of the wave-vector: $k_{\parallel} = 2\pi m/(2l)$ (here $m$ is the longitudinal mode number, and $l$ is the linear cavity length), then the transverse wave-numbers of the plane mirror resonator are: $k_{\perp} = \sqrt{|\mathbf{k}|^2 - k_{\parallel}^2} = \sqrt{(\omega/c)^2 - (\pi m/l)^2}$, resulting in the well known Fresnel ring structure. For many applications (e.g. lasers, nonlinear optical systems) only the isotropic central Fresnel spot ($\omega \approx \omega_0$), or the central ring $\omega \approx \omega_0$ determines the angular profile of the resonator transmission, where $\omega_0 = \pi m_0 / l$ is the resonance frequency of the $m_0$-th longitudinal mode.

Here we investigate the mode structure of the resonator filled by two dimensional (2D) photonic crystal (PhC), i.e. the resonator with the refraction index modulated in the longitudinal and in one transverse direction. It is known that the diffraction properties of light propagating through PhCs can be substantially modified [48-54, 83] The diffraction of light in index modulated materials can be inverted in sign (can become negative) [48, 49, 83], or can be set to zero [50-54] resulting in the so called self-collimation effect. In the latter case one also uses the term “subdiffraction” [54], since when the leading order of diffraction is eliminated, the light propagation is governed by the higher orders of diffraction (with spatial derivatives of the order larger than two), i.e. by subdiffraction. The origin of the subdiffraction is that the spatial dispersion curves (or spatial dispersion surface in 3D case) are modified due to the presence of the PhCs in such a way, that it develops flat segments (or flat surface areas in the 3D case). The wavevectors lying on the flat segments have the same longitudinal components, thus the plane wave constituents of the beam do not dephase during the propagation, and the beam propagates without

the diffractive spreading (see Fig. 3.1(b)). The beam width is inversely proportional to the width of plateau. Consequently only sufficiently broad plateaus of the diffraction curve result in subdiffraction; the narrow plateaus result in the opposite effect of spatial frequency filtering.

The idea behind this chapter is that the deformation of the diffraction curve (or of diffraction surface in 3D case) strongly modified the mode structure of the resonator too. In particular the broad angular region of the wave-vectors can be at resonance for a fixed detuning for subdiffractive intracavity PhCs, as Fig. 3.1(b) illustrates. The broad spatial spectrum at the resonance means that the resonator supports relatively small space scale structures. The dashed line in a) indicates the spatial dispersion curve without paraxial approximation (half-circle). The dashed lines in b) indicate the dispersion curves in the limit of vanishing index modulation ($s \to 0$).

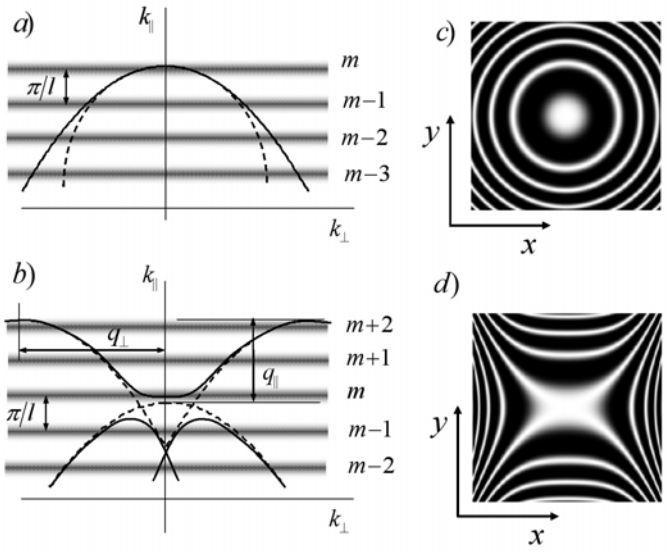


Fig. 3.1. The spatial dispersion curves of the monochromatic plane waves in homogeneous media (a) and of the Bloch modes in photonic crystals (b). The dispersion curve is calculated by a standard technique of harmonic wave expansion [A5]. The dashed lines in (b) indicates the dispersion curves of the uncoupled plane waves (or equivalently of the Bloch modes in the limit of vanishing index modulation ($s \to 0$)). The thick fuzzy lines in (a, b) indicate the resonances of the resonator as characterized by the condition of the longitudinal component of the wavevector $k_\parallel = 2\pi m/(2l)$. (c) the Fresnel ring structure of the homogeneously filled resonator, and (d) shows the mode structure for the resonator with index modulation in one transverse direction.

The resonator for our experiments was fabricated having in mind that the nondiffractive propagation in the first propagation band occurs along diagonal direction of the square- or the rhombic lattice of PhC [50-54]. The resonator, as used in experiments, is shown schematically in Fig. 3.2(a). 1D (or 2D) periodical refractive index modulation was added on a mirrors surface. The mirrors were shifted one with respect to another by the half of the grating period in order to mimic the 2D photonic crystal with the optical axis directed along the diagonals of rhombs (see Fig. 3.2(b) for the unfolded structure of the resonator). In this way the radiation in a round trip along the resonator "sees" exactly one longitudinal period of the unfolded PhC.

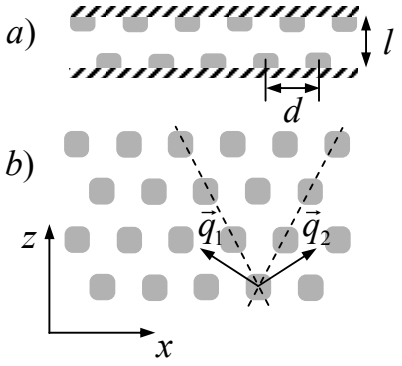


Fig. 3.2. The scheme of the resonator used in experiments a), and the corresponding unfolded PC structure b). The dashed lines indicate crystolographic axes of the unfolded PC structure, and the arrows represent the vectors of the reciprocal lattice.

### 3.1.2 Mode expansion method

The theoretical analysis of the resonator is based on the unfolded structure of the modulated resonator (Fig. 3.2(b), with the refraction index periodic in the $x$ (transversal) and $z$ (longitudinal) directions with the corresponding periods $d$ and $2l$. We solve first the paraxial equation for the light propagating through the unfolded PhC structure:

$$\partial_Z A(\mathbf{r}) = i\left[\nabla_\perp^2 + V(\mathbf{r})\right]A(\mathbf{r}), \qquad (3.2.1.1)$$

where $\nabla_\perp^2 = \partial^2/\partial X^2 + \partial^2/\partial Y^2$ is the Laplace operator acting in the transverse plane. The transverse coordinates $X, Y$ are normalized to $x_0 = d/2\pi$ in order to make the normalized transverse wave-number of the index grating equal to

unity $q_\perp = 1$, and the longitudinal coordinate is normalized to $z_0 = 2|\mathbf{k}|x_0^2$ in order to make the coefficient of diffraction equal to one. The longitudinal period of the index grating in the new coordinates $Z$ is then $L = l(2\pi)^2/(|\mathbf{k}|d^2)$ and the corresponding wave-number is $q_\parallel = 2\pi/L = d^2/(\lambda l)$. $V(\mathbf{r})$ is proportional to the refraction index: $V(\mathbf{r}) = 2x_0^2 n(\mathbf{r})$.

We expand the field into a set of the plane waves:

$$A(\mathbf{r}) = e^{i(k_x X + k_y Y)} \sum_{m,n} a_{m,n}(Z) e^{i(mX - nq_\parallel Z)}. \qquad (3.2.1.2)$$

Substitution of Eq. (3.2.1.2) into Eq. (3.2.1.1) yields the coupled equation system:

$$\partial_z a_{m,n} = -i\left[(m + k_x)^2 + k_y^2 - nq_\parallel\right] a_{m,n} + if_{m,n} \sum_{p \neq m, q \neq n} a_{p,q} \qquad (3.2.1.3)$$

for the amplitudes of the plane waves $a_{m,n}$. Here $f_{m,n}$ is the matrix of the coupling coefficients depending on the modulation of the index: $f_{m,n} = c^{-1} \int V(\mathbf{r}) e^{-i(mX - nq_\parallel Z)} d\mathbf{r}$, as integrated over unit cell of the PhC lattice, $c$ being the area of the cell.

It comes out that only the three harmonics in the expansion (3.2.1.2) are relevant for the subdiffractive propagation through the PhC (see e.g. [54, 84], and consequently for the subdiffractive dynamics of the resonator. We therefore rewrite (3.2.1.3) in terms of the vector of the amplitudes of plane waves: $\mathbf{A} = \{a_{-1,1}, a_0, a_{11}\}$. In the limit of zero coupling these are the waves propagate with wave-vectors $\{(k_\perp - 1, k_\parallel + q_\parallel), (k_\perp, k_\parallel), (k_\perp + 1, k_\parallel + q_\parallel)\}$. The integration of (3.2.1.3) over one longitudinal period of the PhC (equivalently over one resonator round trip) leads to the mapping:

$$\mathbf{A}(Z + L) = e^{(\mathbf{P}+\mathbf{F})L} \mathbf{A}(Z) \qquad (3.2.1.4)$$

$\mathbf{P}$ is diagonal propagation matrix with the elements: $\left(-i(k_\perp - 1)^2 + iq_\parallel, -ik_\perp^2, -i(k_\perp + 1)^2 + iq_\parallel\right)$, and $\mathbf{F}$ is the scattering matrix:

$$\mathbf{F} = \begin{pmatrix} 0 & if & if \\ if & 0 & if \\ if & if & 0 \end{pmatrix} \tag{3.2.1.5}$$

We considered here all off diagonal elements of $\mathbf{F}$ equal, as guided by experimental measurements of the scattering from the grating, however the qualitative results are not sensitive to the form of the matrix $\mathbf{F}$.

We calculated the propagation through unfolded PhC structure (and consequently performed a search of the zero diffraction point) by diagonalising the propagation and the scattering matrix $\mathbf{P}+\mathbf{S}$. The imaginary part of the eigenvalues yields the dispersion relation $k_Z(k_X, k_Y)$. Respectively the imaginary part of the eigenvalues of the propagation operator over longitudinal period of the PhC yields the phase shift of the Bloch modes over the PhC period. Fig. 3.1(b) shows the dispersion relation at cross-section $k_y = 0$, as calculated at zero diffraction point. The zero diffraction point means that initially parabolic segments of the dispersion curves interact, pull one from another at the crossing points, and disshape into the flat segments. The degree of the lift of degeneracy is proportional to the coefficient of coupling. It follows from the geometric considerations that the zero diffraction point occurs close to- (but not exactly at-) the point of the triple intersection of the spatial dispersion curves $L = 2\pi$ (see Fig. 3.1(b)) with the distance depending on the scattering strength $s$.

Asymptotic analysis was performed in order to localize the zero diffraction point. In the limit of weak scattering $f << 1$, also near to triple intersection point $q_{\|} \to 1$ ($L \to 2\pi$), the spatial dispersion curve (the corresponding eigenvalue of (3.2.1.4)) can be obtained as the series expansion at the point $k_x = k_y = 0$:

$$k_Z(k_X, k_Y) = D_0 - D_2 k_X^2 - k_Y^2 - D_4 k_X^4 + O(k_X^6) \tag{3.2.1.6}$$

For the scalings see e.g. [54, 84]. Here $D_0 = 2f^2/(1-q_{\|})$ is the uniform shift of the wavenumber due to the modulation of refractive index;

$D_2 = 1 - 8f^2/(1-q_{||})^3$ is the first (leading) order diffraction coefficient, which can be tuned to zero at $8f^2 = (1-q_{||})^3$; $D_4 = 32f^2/(1-q_{||})^5$ describes the second order diffraction, which becomes dominant at- or close to the zero diffraction point. The spatial dispersion surface (3.2.1.6) has a single maximum in normal diffraction regime ($8f^2 < (1-q_{||})^3$), however it has the shape of saddle in case of negative or zero diffraction.

Next, in order to consider the resonator, we introduce the nonzero transmission of the mirrors (by adding the losses to the mapping (3.2.1.4)), the resonator phase shift, and take into account the incident light at every roundtrip. The role of the mirrors were accounted by considering the diagonal matrix with elements $t^2$: $t^2\mathbf{1}$, where $\mathbf{1}$ is the unit matrix, and $t$ denote the transmission of a mirror (the resonator of two identical mirrors was considered). The resonator phase shift was described by term $e^{i\varphi\mathbf{1}}$. The incident light was accounted by adding the incident light $\mathbf{A_0} = (0,t,0)$ at every resonator round trip. We consider for simplicity in the limit of a good finesse cavity (this means the weak scattering in the PC structure and the highly reflecting mirrors), which allows to simplify the propagation operator in (3.2.1.4) by expanding it in series $e^{(\mathbf{P}+\mathbf{F})L+i\varphi\mathbf{1}} \approx \mathbf{1} + (\mathbf{P}+\mathbf{F})L + i\varphi\mathbf{1} + \ldots$. This expansion actually means a close-to resonance limit. We calculate the resonator transmission in an analogous way as the transmission of the homogeneous plane-mirror Fabri-Perror resonator, however manipulating not with the scalar field, rather with the vector $\mathbf{A}$ consisting of plane wave components. We required, in a standard way, that the radiation inside the cavity is unaltered during the round trip. $\mathbf{A}(L) = \left(\mathbf{1}(1-t^2+i\varphi) + (\mathbf{P}+\mathbf{F})L\right)\mathbf{A}(0) + \mathbf{A}_0$, where $\mathbf{I}$ is the unit matrix. Then the calculation of the resonator transmission results in the inversion of the matrix:

$$\mathbf{R} = \left(\mathbf{1}(t^2 - i\varphi) - (\mathbf{P}+\mathbf{F})L\right)^{-1}\mathbf{T} \qquad (3.2.1.7)$$

The element $R_{22}$ of the resonator matrix (3.2.1.7) yields the transmission of the central component of the resonator.

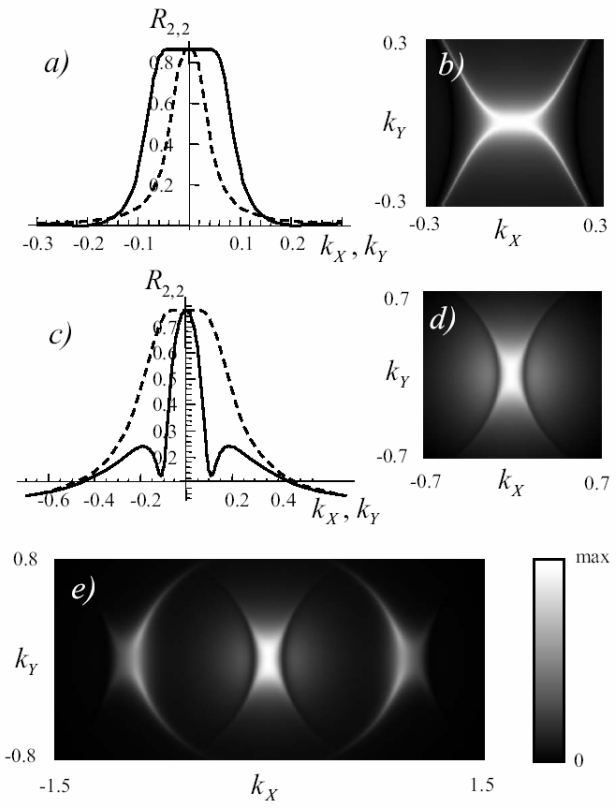


Fig. 3.3. The transmission of the resonator: (a), (c) show transmission on the cross sections $k_Y = 0$ (solid lines) and $k_Z = 0$ (dashed lines). (b), (d) show 2D transmission profiles. (e) shows the full transmission as containing not only the central transmission component given by $R_{22}$ but also the first diffraction maxima given by $R_{21}$ and $R_{23}$. Parameters for (a), (b) are $L = 9.5$, $s = fL = 0.75$, $t = 0.1$, $\varphi = -0.395$; for (c)-(e), $L = 7.5$, $s = fL = 0.45$, $t = 0.44$, $\varphi = -0.35$.

The transmission of the resonator can be calculated at the zero diffraction point numerically, as based on (3.2.1.7). The cross sections and the 2D shapes of the angular intensity transmission are given in the Fig. 3.3 in two different limits. Figs. 3.3(a, b) represents the subdiffraction limit, where the angular transmission function is broadened in the direction of modulation, as compared to the distribution in homogeneous resonator. This case corresponds to the situation when the plateau of the manipulated spatial dispersion curve is relatively broad. The Figs.3.3(c-e) represent the opposite limit, when the dispersion curve develop relatively narrow plateaus, resulting not in subdiffraction but rather to the filtering function of the resonator. In all cases the formation of strongly anisotropic (of hyperbolic or X-like form) transmission distributions is evident.

Set of captions (Fig. 3.4(a-c)) are calculated at optimal resonator length $d = 4.75$ for subdiffraction regime with slightly different resonator detuning. Subdifraction regime is clearly visible in Fig. 3.4(b) and shows X-shape form and central plateo. Phase difference in Fig. 3.4 between (a) and (b) and (b) and (c) recounted in length will be in order 24 – 30 nm. That is about 20 times smaller compared to illuminating light (532 nm) and makes the resonator very sensitive to any mechanical impact and complicates attenuation of a cavity.

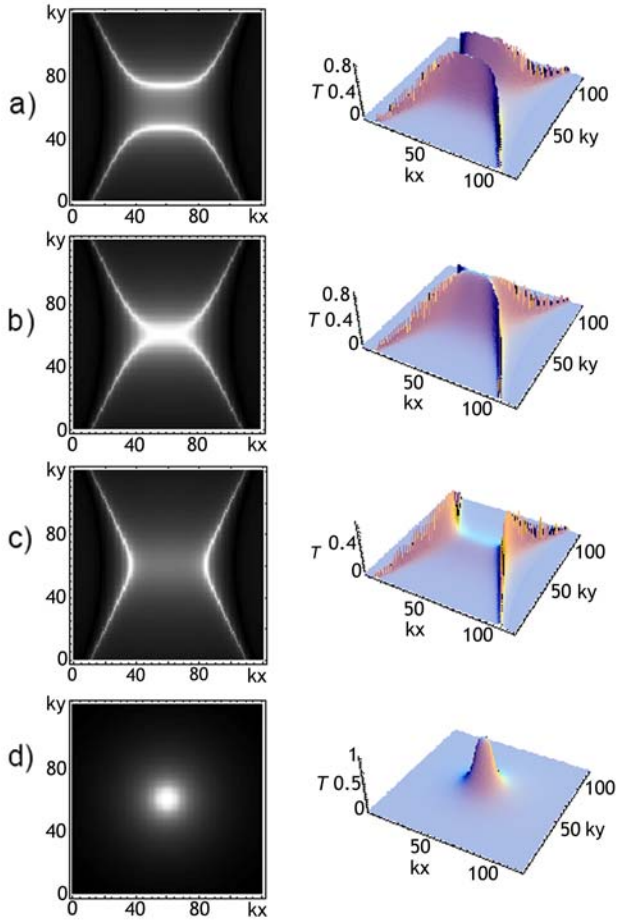


Fig. 3.4. Transmission of a PhC resonator counted using mode expansion method at zero diffraction length $d = 4.57$. Parameters: $s = 0.75$, $t = 0.01$, $d = 4.75$, $m=\pi$, $\varphi(a) = -0.35$; $\varphi(b) = -0.395$; $\varphi(c) = -0.45$. Transmission in homogeneous case (d)

PhC resonator superdiffraction regime can be evaluated at shorter cavity length and higher mirrors transmission. Typical 2D angular transmission profile is shown in Fig. 3.5.

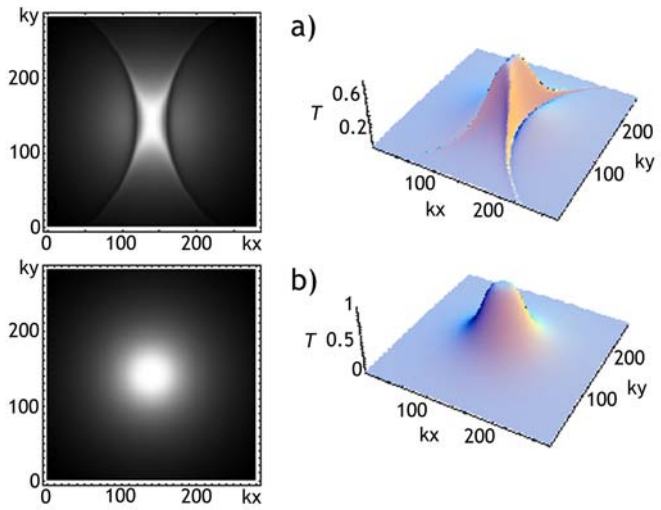


Fig. 3.5. Transmission of a PhC resonator counted using mode expansion method at superdiffraction length $d$ = 3.75 with parameters: $s$ = 0.45, $t$ = 0.15,$\varphi$ = -0.35 (a) and in homogeneous case: $t$ = 0, $\varphi$ = 0 (b).

### 3.1.3. Point scattering method

Another theoretical-numerical analysis of the resonator modes is based on the multiple scattering matrix technique. We analyze a round trip propagation of light along the resonator, and calculate the transformation of the field on each of the elements consecutively: i) the diffraction on the modulated surface of the mirror; ii) the free space propagation between the mirrors (diffraction in homogeneous material); iii) the lateral shift of the periodic structure of the mirrors with respect one to another, iv) the partial reflections from the mirrors. After calculating the field transformation in a resonator roundtrip (by applying the transformation operators, i.e. by multiplying by corresponding transformation matrices), we calculate the resonator transmission matrix by the standard techniques: by adding the entering plane wave to the resonators, and by searching for a stationary state. This is essentially a classical approach to calculate the mode structure of the homogeneously filled Fabry-Perrot resonator, with the difference that the field transformations on each of the element in the resonator now are not the scalars but operators (represented by matrices).

The periodic modulation of the mirror surface results in a set of diffraction components in reflected light with transverse the components of the wavevectors $\vec{k}_\perp + \vec{q}_{m,n}$, here $\vec{k}_\perp = (k_x, k_y)$ is the transverse wavevector of the incident light, and $\vec{q}_{m,n} = (mq_x, nq_y)$ are the multiples of the modulation wavevector. Strictly speaking one should consider all the possible field harmonics, however, it comes out that the consideration of the central component plus the first order sidebands is sufficient [A5]. For 1D modulation of the mirrors this results in three components (as considered in [A5]), for 2D square modulation of the mirrors - in five components [86]. We approximate, therefore, the optical field in the following way:

$$A(\mathbf{r}) = e^{i(k_x x + k_y y)}\left(a_{0,0} + a_{-1,0}e^{-iq_x x} + a_{+1,0}e^{iq_x x}\right) \qquad (3.1.3.1)$$

For convenience, the field is represented by the column-vector of plane wave components:

$$\vec{A} = \left(a_{-1,0}, a_{0,0}, a_{+1,0}\right)^T \qquad (3.1.3.2)$$

The $q_\perp = q_x$ are the wavevector of the index modulation in the transverse direction (the field is expanded in its harmonics). Next we list separately all the field transformations in the resonator roundtrip.

**Scattering by the phase grating** The periodically modulated phase of the field on the reflection of the surface of the mirror couples the components of the field vectors. For the harmonic modulation the coupling occurs between the central component $a_{0,0}$ and the sidebands in this tree harmonic model. We introduce the phenomenological scattering coefficient $s_x$. The scattering s can be linked to microscopic parameters of the coating, as the depth of the modulation, and the refraction index of the photoresist. However it is more convenient to keep the macroscopic scattering parameter, as it is directly linked with the experimentally accessible diffraction efficiency of the grating

(*s* is the square root of the scattering intensity into the sidebands). The scattering matrix is:

$$\hat{S} = Exp\begin{pmatrix} 0 & is_x & 0 \\ is_x & 0 & is_x \\ 0 & is_x & 0 \end{pmatrix} \tag{3.1.3.3}$$

More convenient (for numerical purposes) is however to simplify the scattering operator, which in (3.1.3.3) is the matrix exponent:

$$\hat{S} = \begin{pmatrix} 1+\frac{1}{2}\left(-1+\sqrt{1-2s_x{}^2}\right) & is_x & \frac{1}{2}\left(-1+\sqrt{1-2s_x{}^2}\right) \\ is_x & \sqrt{1-2s_x{}^2} & is_x \\ \frac{1}{2}\left(-1+\sqrt{1-2s_x{}^2}\right) & is_x & 1+\frac{1}{2}\left(-1+\sqrt{1-2s_x{}^2}\right) \end{pmatrix} \tag{3.1.3.4}$$

**Free propagation.** The free propagation over the linear length of the resonator is considered by the paraxial propagation equation:

$$\partial_z A(\mathbf{r}) = \frac{i}{2k_0}\nabla_\perp^2 A(\mathbf{r}) \tag{3.1.3.5}$$

where $\nabla_\perp^2 = \partial^2/\partial x^2 + \partial^2/\partial y^2$ is the Laplace operator acting in the transverse plane. Substitution of expansion (3.1.3.1) into (3.1.3.5) yields the equation system:

$$\partial_z a_{m,n} = -\frac{i}{2k_0}\left[(mq_x + k_x)^2 + k_y{}^2\right]a_{m,n}, \tag{3.1.3.6}$$

Integration of (3.1.3.6) over one linear resonator length results the diagonal transformation matrix:

$$\vec{P} = \begin{pmatrix} e^{-id(1+k_x)^2} & 0 & 0 \\ 0 & e^{-idk_x^2} & 0 \\ 0 & 0 & e^{-id(-1+k_x)^2} \end{pmatrix}, \qquad (3.1.3.7)$$

Here $L = l/(2k_0)$ is the normalized length of the resonator, representing its diffraction.

**Lateral shift of the mirror.** We account for the lateral shift of the grating (determined by $\vec{m}$) using the following trick. We fix the reference frame with the position of the first mirror. Then, for the calculation of the scattering from the laterally shifted second mirror we change the reference frame, by applying the operator:

$$\vec{M} = \begin{pmatrix} e^{im} & 0 & 0 \\ 0 & 1 & 0 \\ 0 & 0 & e^{-im} \end{pmatrix} \qquad (3.1.3.8)$$

Then, after calculation the scattering on the second mirror (by using (3.1.3.3) or (3.1.3.4)) in the new reference frame), we restore the original reference frame, by applying $\vec{M}^{-1}$.

**Resonator mirrors.** Since the reflectivity is the same for all harmonic components of the wave, it is accounted in a standard way – by multiplication by a scalar $r$. Without losing generality in theory, and in accordance to our experiment, we consider the both mirrors of the same reflectivity.

**Resonator roundtrip.** The variation of the field in a resonator roundtrip is calculated by applying consecutively all the operators discussed above:

$$\hat{R} = r^2 \hat{P}\hat{M}^{-1}\hat{S}\hat{M}\hat{P}\hat{S} \qquad (3.1.3.9)$$

**Resonator transfer function.** The plane wave entering into the resonator is denoted in this vector form by $\vec{A}_0 = (0,0,B_0,0,0)^T$. Then we calculate the

radiation balance in one resonator roundtrip, and analogously to the homogeneous Fabry-Perot case, we obtain:

$$\vec{A} = t\left(\hat{1} - \hat{R}\right)^{-1} \vec{A}_0 \qquad (3.1.3.10)$$

for the radiation at the entrance mirror. The only difference from the homogeneous Fabry-Perot case is that here we deal with the vectors of the wave components and transformation matrices, instead of complex scalar factors. Finally the resonator transmission matrix is:

$$\hat{T} = t^2\left(\hat{1} - \hat{R}\right)^{-1} = t^2\left(\hat{1} - r^2\hat{M}^{-1}\hat{P}\hat{S}\hat{M}\hat{P}\hat{S}\right)^{-1}. \qquad (3.1.3.11)$$

The transmission for the homogeneous component is given by the element $T_{0,0}$ of the transfer matrix (3.1.3.11). The scattering of the resonator into the sidebands harmonics is described by the corresponding off-diagonal column elements of the matrix: by $T_{-1,0}$ and $T_{+1,0}$ into the diffraction components in x direction.

Set of captions (Fig. 3.6(a-c)) are calculated at optimal resonator length d = 4.75 for subdifraction regime with slightly different resonator detuning. Subdifraction regime is shown in Fig. 3.6(c) Resonator 2D transmission profilles are in general the same as calculted using *mode expansion* method (Fig. 3.4). Phase difference in Fig. 3.4 between (a) and (b) and (b) and (c) recounted in length will be of the order of 15 nm. That is aabout 40 times smaller compared to illuminating light wavelength (532 nm) and predicts even bigger resonator sensitivity to mechanical impact than that obtained by mode *mode expansion* method.

Resonator superdiffraction regime profiles are shown in Fig. 3.7. Fig. 3.7(a) shows strict X shape profile calculated for high finesse cavity (t=0.01). Fig. 3.7(b) shows typical transmission profile and is the same character as it was obtained by *mode expansion* method (Fig. 3.5(a)).

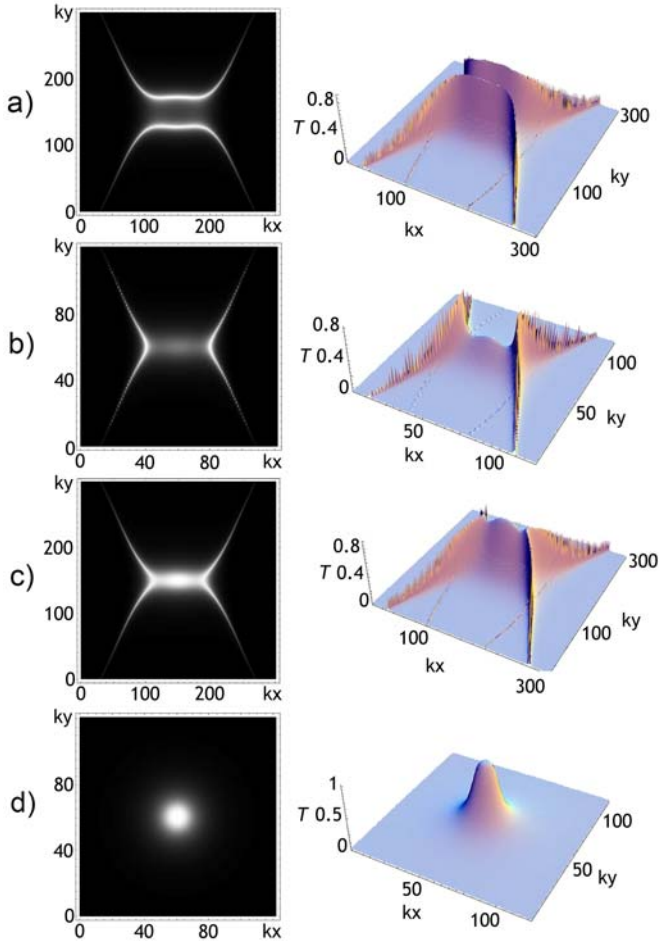


Fig. 3.6. Transmission of a PhC resonator counted using point scattering method at zero diffraction length $d = 4.75$ with parameters: $s = 0.35$, $t = 0.07$, $d = 4.75$, $m = \pi$, $\varphi(a) = -0.22$, $\varphi(b) = -0.25$, $\varphi(c) = -0.24$. Transmission in homogeneous case (d) $\varphi = 0$, $s = 0$.

Difference between these two methods is evident if full transmission is containing not only the central transmission component given by $R_{22}$ but also the first diffraction maxima given by $R_{21}$ and $R_{23}$ (Fig. 3.8). In case of *point scattering* method resonator Freshnel ring structure is presented. As it will be shown experimentally, *point scattering* method can fully describe PhC resonator.

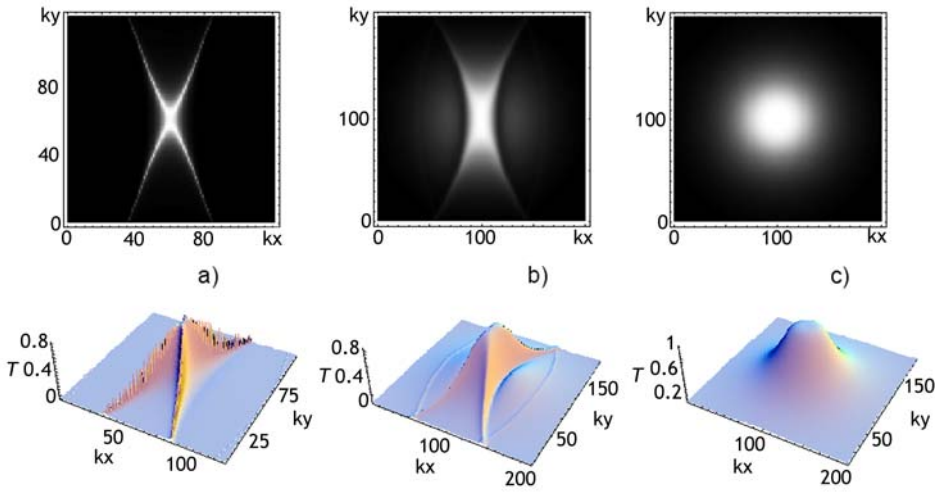


Fig. 3.7. Transmission of a PhC resonator counted using point scattering method at superdiffraction length $d = 3.6$ with parameters: (a) – $s = 0.2$; $t = 0.01$; $m = \pi$; $\varphi = -0.27$; (b) – $s = 0.2$; $t = 0.15$; $m = \pi$; $\varphi = -0.27$; (c) – homogeneous case $s = 0$; $\varphi = 0$; $t = 0.15$.

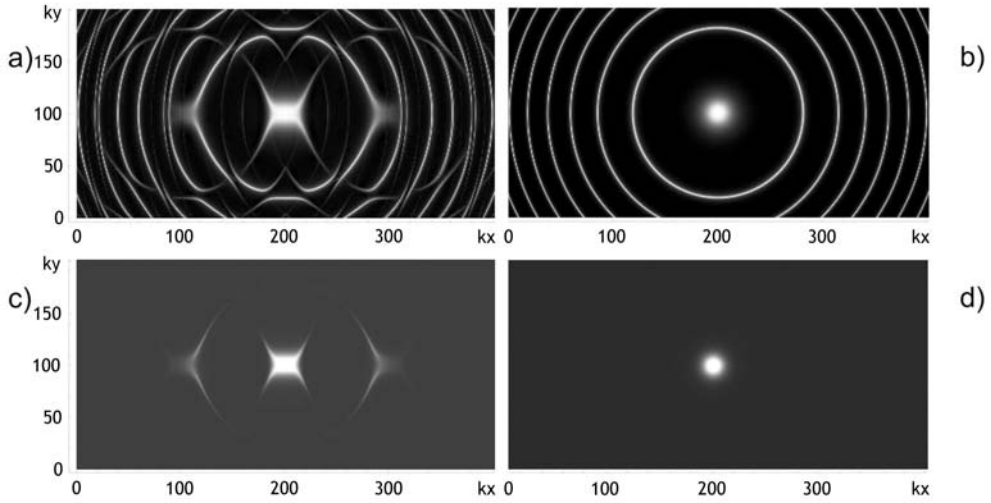


Fig. 3.8. 2D PhC resonator full transmission containing not only the central transmission component given by $R_{22}$ but also the first diffraction maxima given by $R_{21}$ and $R_{23}$. *Point scattering* method in (a) with parameters: $s = 0.35$; $t = 0.07$; $\varphi = -0.27$ and *mode expansion* method in (c) with parameters: $s = 0.75$; $t = 0.07$; $\varphi = -0.395$. Corresponding homogeneous case in (b) and (d).

### 3.1.4. Parameter analysis

It is convenient to analyze 2D resonator spatial characteristics by using transmission cross sections $k_Y = 0$. Resonator transmission profile depends on cavity length ($d$) and fine tuning, or phase $\varphi$, diffraction efficiency $s$, mirrors

transmission $t$. As it was mentioned above, two cavity spatial dispersion characteristics can be distinguished: superdiffraction (filtering) and subdiffraction. Thought critical length for subdiffraction can be evaluated in general there are appropriate parameter limits for one or another regime. Figs. 3.9(a, c, e) represents superdiffraction, Figs. 3.9(b, d, f) subdiffraction. Black line in Fig. 3.9 indicates transmission of a homogeneous cavity.

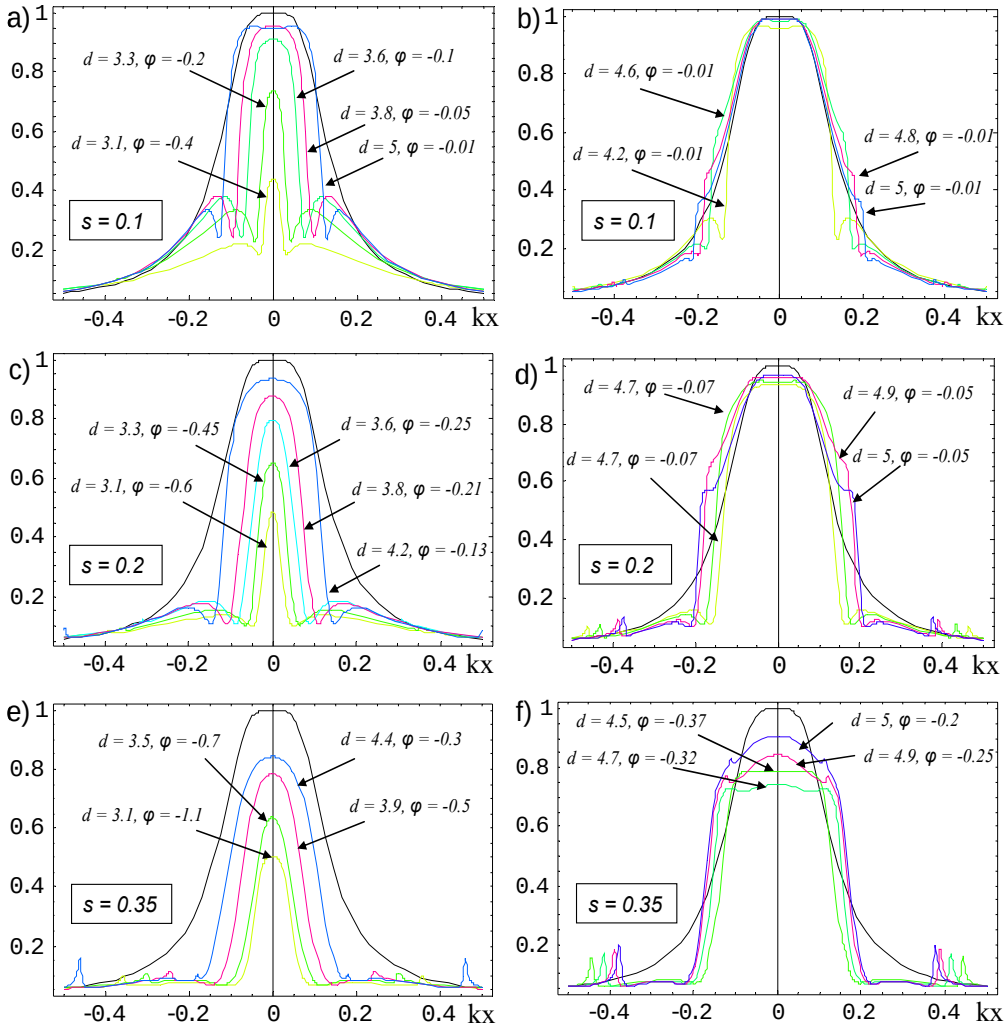


Fig. 3.9. Resonator transmission cross section at $k_y = 0$ for different cavity parameters. Super-diffraction case considered in (a, c, e). Subdifraction considered in (b, d, f). Resonator transmission $t = 0.1$ fixed for all cases.

Resonator phase is attenuated for maximum transmission and filtering. At low diffraction efficiency (Fig. 3.9(a) $s = 0.1$ and $3.3 \le d \le 3.8$ filtered central peak

transmission exceeds 0.9, but the boarders are relatively high. If length is shorter cavity transmission decreases rapidly. For the higher length angular transmission spectrum is wider than homogeneous resonator. Boarders gets smaller if diffraction efficiency is increased (see Fig. 3.9(c)). For diffraction efficiency $s$ = 0.35 Fig. 3.9(e) boarders are insignificant, but central peak transmission decreases down to 0.8.

Cavity length for subdifraction regime is in range 4.5 $\leq d \leq$ 5. If diffraction efficiency is low ($s$ = 0.1) subdifraction is insignificant (Fig. 3.9(b)) and the central peak transmission is near 1. Higher diffraction efficiency makes transmission broader than homogeneous one (Fig. 3.9(d)). Dispersion curve has abrupt edges so the cavity still can be used as a filter. In case of high diffraction efficiency (Fig. 3.5(f)) dispersion exhibits quadratic-like shape with nearly flat platou. There should be noted, that in case of high diffraction efficiency the shape of dispersion curve is very sensitive to cavity phase.

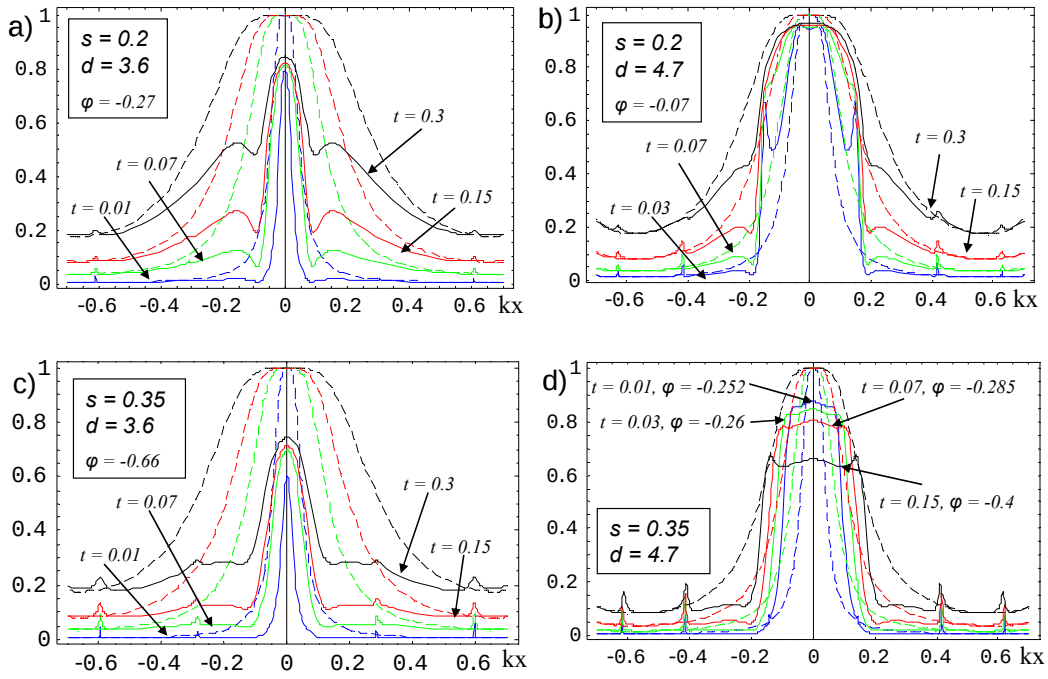


Fig. 3.10. 2D modulated resonator spatial dispersion cross section at $k_y$ = 0 dependence on cavity mirrors transmission $t$. Superdiffraction case considered in (a, c). Subdifraction considered in (b, d).

Cavity finesse influence on spatial dispersion characteristic is summarized in Fig. 3.10. Two sets of parameters are used to explore filtering and subdifraction. Transmission of uniform resonator is indicated by dashed lines. Higher cavity finesse (lower mirrors transmission) reduces borders around central peak in all cases. Figs. 3.10(a, c) shows filtering regime. One can see, that filtering is possible at any cavity mirrors transmission or gratings diffraction efficiency. Though lower mirrors transmission reduces boarders but does not affect central peak intensity very much. After filtering central peak intensity is lower by number of 20-40 %. From application point of view that might be a problem.

Contrarily to filtering, subdifraction regime cannot be realized in cavity with high transmission mirrors (Figs. 3.10(b, d)). Cavity transmission for diffraction efficiency $s = 0.2$ and constant phase is shown in Fig. 3.10(b). Half intensity width is almost unchanged, but for low transmission mirrors three intensity peaks appear. In Fig. 3.10(d) phase is attenuated to form nearly flat top. It is evident from this picture, that subdiffraction regime takes place in a cavity with relatively high finesse and diffraction efficiency.

### 3.2. Phase diffraction gratings fabrication on dielectric mirror surface

There are several ways of producing refractive index modulation on dielectric mirror surface. It might be photolithography or two photon polymerization. Photolithography technology seems to be acceptable because of relatively simple large area processing. Three different methods were considered in this thesis:

- contact UV photolithography technology;
- interference photolithography technology;
- plasma chemical etching.

The task for technological part was to fabricate harmonic refraction index modulation, i.e. phase diffraction grating. According to resonator parameter analysis presented in the previous chapter, diffraction efficiency to the ±1 order maxima should be 10 % and 80 % should be left at zero order. Diffraction efficiency to the higher order should be as negligible as possible. Grating period is in range from 2 μm to 15 μm. This task was solved by scientist of Kaunas University of Technology, Institute of Physical Electronics.

The low roughness (λ/20) fused silica substrates were used for fabrication of the mirrors. Working side of a mirror was covered with high reflection (98.5 % at 532 nm wavelength) coatings and the other side with antireflection coatings at 532 nm wavelength. The surfaces of the mirrors were first covered with a thin film of positive MICROPOSIT® S1805® photoresist using spin-on coating technique. This part was the same for all three methods listened above.

Using *contact UV photolithography technology* layer of photoresist is exposed to UV light through 2 μm, 4 μm or 15 μm period photomask. Positive photoresist becomes soluble in the basic developer when exposed. This chemical change allows some of the photoresist to be removed by a special solution.

Typical spinning speed of 3000-4500 rpm using MICROPOSIT® S1805® photoresist allow to fabricate 490-420 nm thickness layer. This is an optimal thickness for producing phase diffraction gratings with high diffraction efficiency for 532 nm wavelength ($m = 0.5$, Fig. 3.12), but it is not acceptable for direct formation of low efficiency grating. It is also not acceptable because of non harmonic profile and higher order diffraction maximums. The problem might be solved by heating the sample. Fig. 3.13 shows the influence of sample heating on diffraction efficiency. During heating process rectangular photoresist groves are melting and forms harmonic-like profile (Fig. 3.14). Groves height are also reduced during heating. Despite process simplicity it is hard to repeat results from sample to sample.

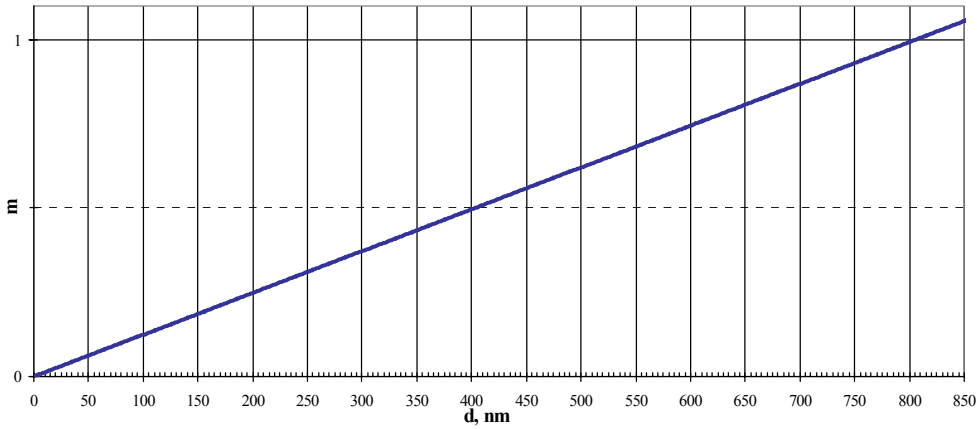


Fig. 3.12. Standing wave number in a transmission phase grating as a function of photoresist thickness ($\lambda$ = 532 nm, $\alpha = 0^0$, $n$ = 1.6602) [http://www.microresist.de (visited on 2008 09 08)].

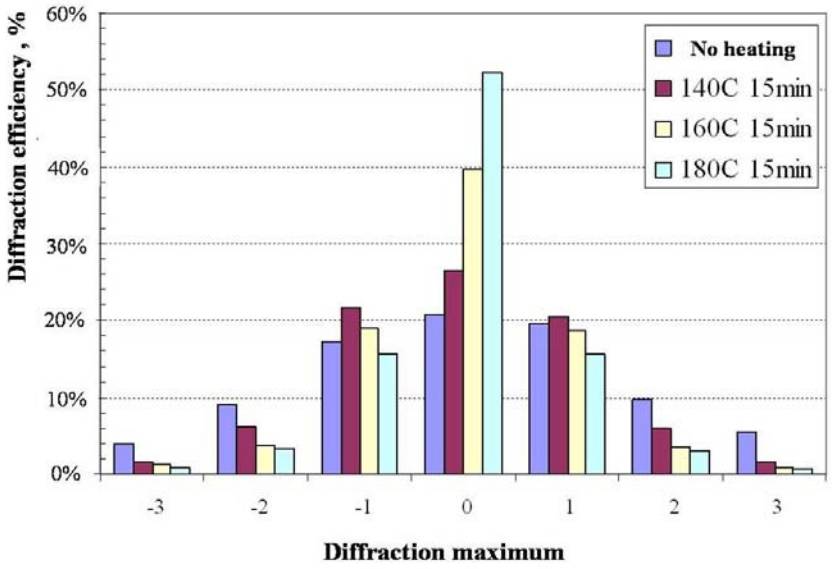


Fig. 3.13. Diffraction efficiency of a 2 μm grating after sample heating

Depth of the periodical structures was estimated using atomic force microscope (AFM). The AFM images (see Fig. 3.14(a–d)) have shown that the profile formed in the photoresist is harmonic-like for 2 μm grating. Profile of 4 μm grating has scotch on top.

*Interference photolithography* technology can also be used for periodic structure formation on dielectric mirrors coatings. Two coherent laser beam interference pattern is formed in a thin photoresist layer. Modulation period

depends on a laser beam wavelength and the angle between interfering beams.

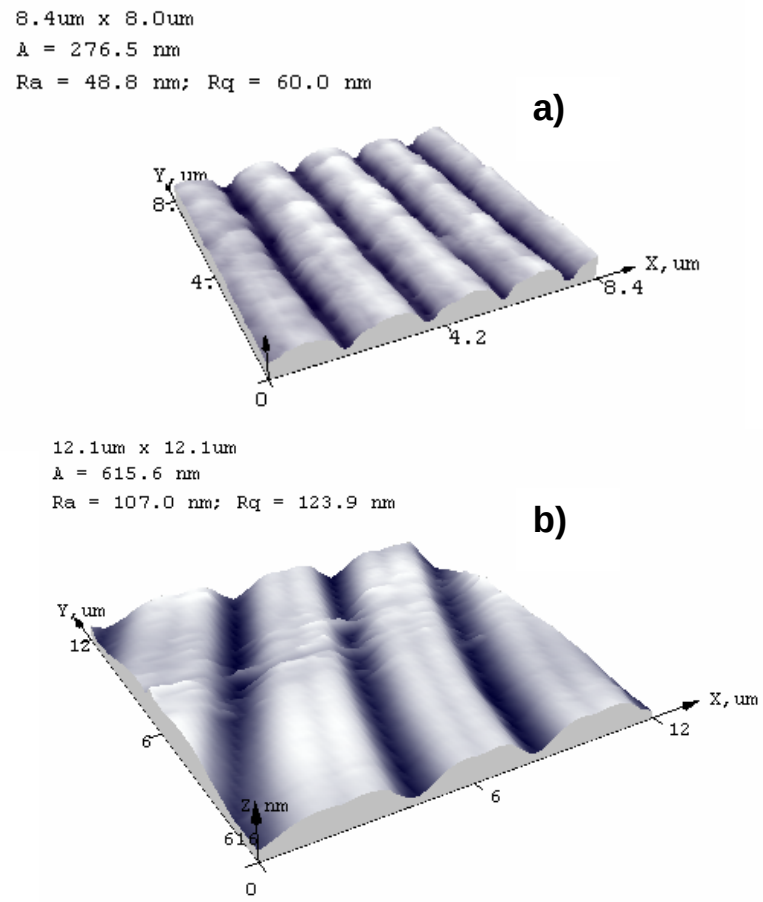


Fig. 3.14. AFM images of 2 μm (a) and 4 μm (b) period gratings.

Positive photoresist becomes soluble in the basic developer when exposed. This chemical change allows some of the photoresist to be removed by a special solution. An advantage of this method is a possibility to control modulation period and physical contact-less processing. On the other side mirrors should be both side coated with antireflection coatings for interference pattern forming laser. Fig. 3.15(a) shows a 2 μm grating formed by using interference photolithography. Two HeCd laser ($\lambda$ = 441.6 nm) beams overlap at $12.7^0$ angle to form a 2 μm interference pattern. Antireflection coatings reduced reflection coefficient for writing laser down to 1% and it wasn't enough to escape parasitic fringes (Fig. 3.15(b)).

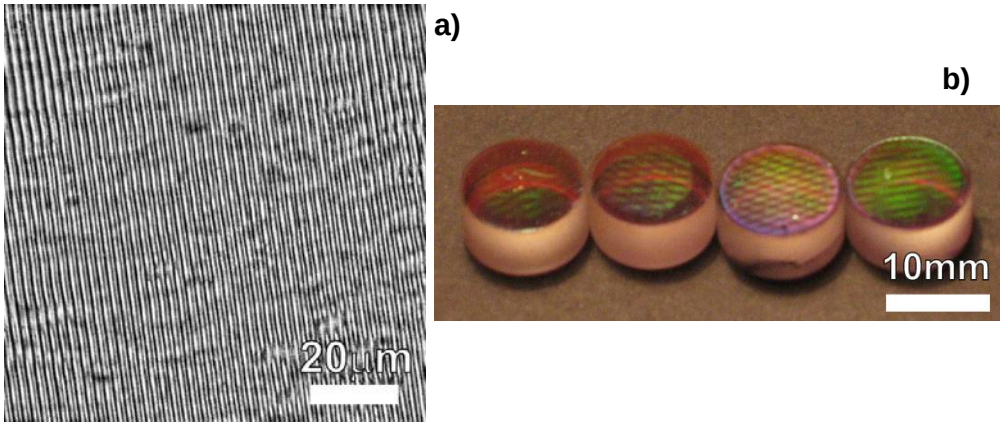


Fig. 3.15. 2 μm grating formed on a interference mirror by Interference photolithography. (a) – image of a optical microscope, (b) – different fringes observed on a samples.

Employing microlithography and *plasma chemical etching* it is possible to transfer 2 μm period gratings formed in softly baked photoresist to the $SiO_2$ top layer of the MLD structure using $CF_4$ / $O_2$ plasma processing [87]. Diffraction gratings were formed on (10 × 10) $mm^2$ substrates using standard contact-optical lithography processes and plasma chemical ion etching. The photoresist was deposited on the substrates employing spin-on coating at 4500 rpm (thickness of the layer 430 nm). The exposition (5 s – 6 s) was performed with the MA 750 contact optical lithography equipment. Residual layer of the developed resist in the grooves of the gratings was removed employing radio frequency (RF) oxygen plasma processing (RF = 13.56 MHz, $P$ = 0.3 W/cm2, $p$ = 133 Pa, $t$ = 60 s). The periodical structures formed in the resist were softly baked in the infrared oven ($T$ = 100 °C) preparing photoresist as a mask for the plasmochemical processing. 2D structures profiles in the SiO2 were etched in the CF4 / O2 feedstock gas mixture (80 % : 20 % and 85 % : 15 %) RF plasma. The etching was performed using plasma-etching equipment PK-2430PD at 67 Pa pressure, total flux of gases was 300 sccm, and 0.75 W/cm2 RF power density. After PCE processing the etching mask was removed boiling the samples in dimethylformamide (DMF). Figure 3.16(a) shows diffraction efficiency dependence on the duration of PCE treatment. AFM image of 2 μm

period grating plasmochemicaly etched in $SiO_2$ shows a harmonic-like modulation of a surface.

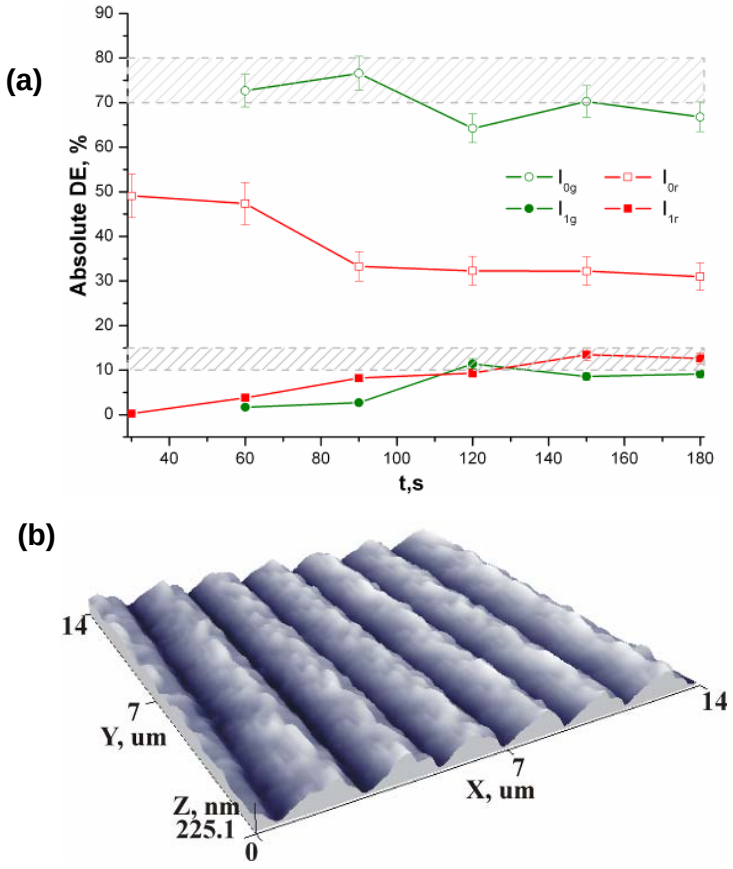


Fig. 3.16 (a) Diffraction efficiency (DE) dependence on the duration of PCE treatment in $CF_4$ / $O_2$ -80 % / 20 % plasma. (b) AFM image of 2 μm period grating plasmochemicaly etched in $SiO_2$ after 150 s of etching [87].

Despite method complexity it allows fine control of grating diffraction properties (Fig. 3.16(a)). $SiO_2$ has a higher optical damage threshold and mechanical strength. This might be useful for third material (for example nonlinear $\chi^2$ material) filled photonic resonator construction.

### 3.3. Experimental realization of photonic crystal resonators

Construction of a photonic crystal resonator in principal is not complicated. Two flat, high reflection dielectrics mirrors with a diffraction grating on a dielectric coating should be parallel at particular critical length. Principal scheme of a PhC resonator is presented in Fig. 3.17. Diffraction gratings must be parallel and shifted by half of a modulation period. The first mirror has two degrees of freedom and can be turned around *x* and *y* axes. The second mirror has all six degrees of freedom and can be turned around *x, y* and *z* and laterally shifted along *x, y, z* axes (Fig. 3.17). For the firs step second mirror is placed and tuned perpendicular to laser beam. It is convenient to tune surface modulation direction along *x* axes. (i. e. diffraction maxima resides in horizontal plane). On a next step the first mirror is placed and turned perpendicular to the laser beam. It was also tuned roughly to match modulation on a second mirror. Optical holder of the first mirror is massive and substantially mounted to the optical table. For maximum accuracy and stability the micrometers screws of a holder are turned by worm-gear.

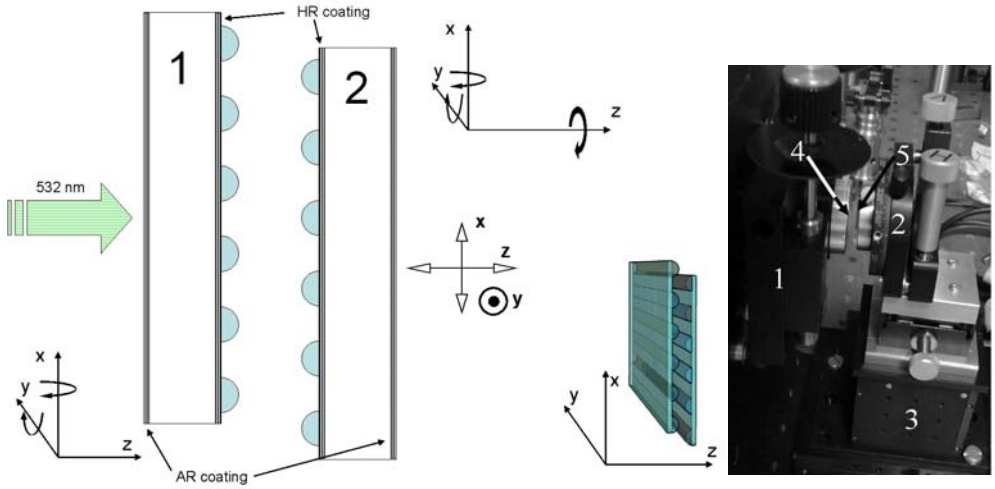


Fig. 3.17. Photonic crystal resonator.

Resonator is adjusted depending on a central transmission spot. Diffuser is placed in front of the first cavity mirror order to obtain wide spatial spectrum. For a precise lateral positioning of a second mirror piezo electrical 10 nm

resolution translation stage was used. For large scale translation in *z* direction mechanical translator was used. Though construction looks simple technically it is very sensitive to any mechanical impact. Experimental setup for resonator spatial transmission registration is shown in Fig. 3.18. The resonator was illuminated by the cw laser beam (wavelength 532 nm, beam width 2.5 mm, power 10-30 mW). A diffuser was placed in front of the resonator in order to generate broad spatial spectrum of the illuminating radiation. A place of a diffuser was tuned in order to find a best picture quality. For a resonator with 2 μm and 4 μm diffuser was placed at 1 mm distance from a resonator front mirror. Since a quality of a gratings was not uniform a beam position on a diffuser was scanned for a best picture quality. A lens of 58 mm focal distance collected the transmitted radiation on CCD camera for the far field recording (Fig. 3.18(a)). In case of a 2 μm modulation resonator a transmitted radiation cannot fit into a lens aperture since the distance from a cavity is limited by an optical holder. White screen and digital photo camera were used for far field recording in this situation (Fig. 3.18(b)).

.

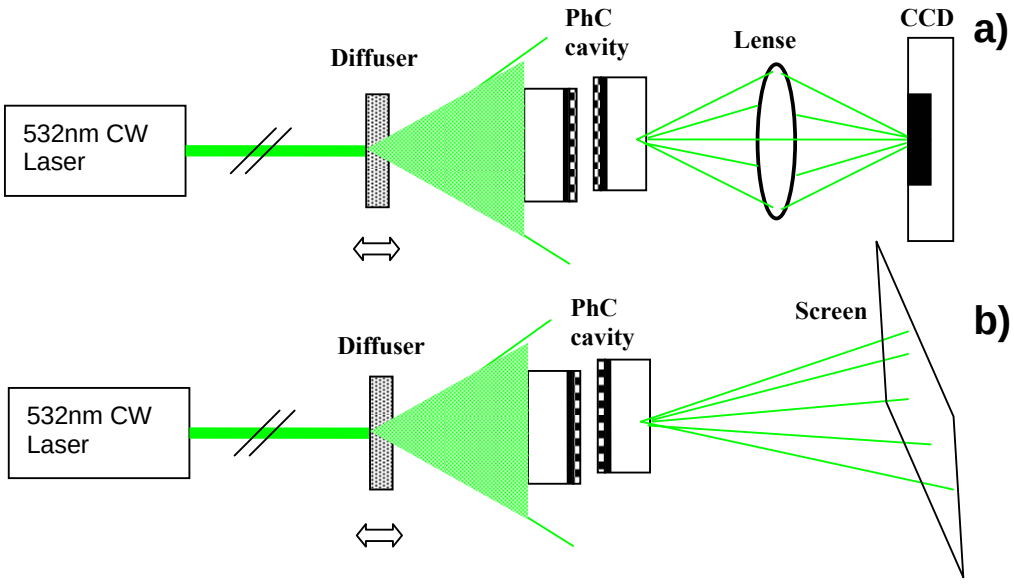


Fig. 3.18. Experimental schemes for PhC resonator transmission recording. (a) – for a 4 μm and 15 μm period modulation of a mirrors surface, (b) – for a 2 μm period modulation.

*PhC resonators with 1D modulation of the mirror surfaces.*

First experiments were done with 15 μm period modulated mirrors. Diffraction grating was fabricated using standard photolithography technology (chapter 3.2). In experiments we tuned the length of the resonator on a large scale in order to obtain the zero diffraction regimes, which, according to the theoretical calculations calculated value ($L = 7.5$) was evaluated to be $l = 0.55\,mm$ (the critical point of triple interaction occurs at $l = d^2/\lambda = 0.44\ mm$). The length of the resonator was also tuned on the small (submicron) scale in order to vary the phase, and tune to the resonance. Fig. 3.19 shows the experimentally recorded and numerically simulated far field pattern. Experimentally obtained distribution corresponds well to the theoretically calculated X-like structure.

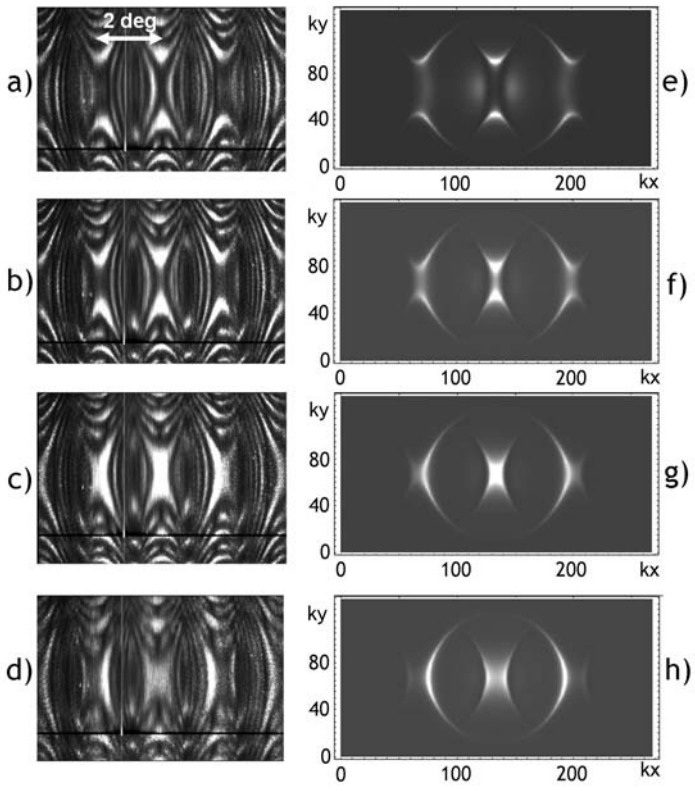


Fig. 3.19. 2D transmission profiles.(a, b, c, d) experimentaly recorded, (e, f, g, h) shows numerically calculated the full transmission as containing not only the central transmission component given by $R_{22}$ but also the first diffraction maxima given by $R_{21}$ and $R_{23}$.Parameters: $s$ = 0.75, $t$ = 0.2, $d$ = 3.75, $\varphi$(e) = 0, $\varphi$(f) = -0.94, $\varphi$(g) = -1.26, $\varphi$(h) = -1.57.

It is clearly visible, that side bands, as appearing from the first diffraction maxima (Fig. 3.19(e-h)) are also observed experimentally. Numerical simulation also works well for different cavity length tuning in submicron scale.

Apart from the central part, however a lot of higher order diffraction components are present in experimentally recorded transmission pattern (Fig. 3.20). Those components are beyond the theoretical treatment, as related with the higher diffraction orders (in theoretical treatment only the first diffraction orders are considered) as well as related with the different longitudinal modes (in the theory the single longitudinal mode treatment is considered).

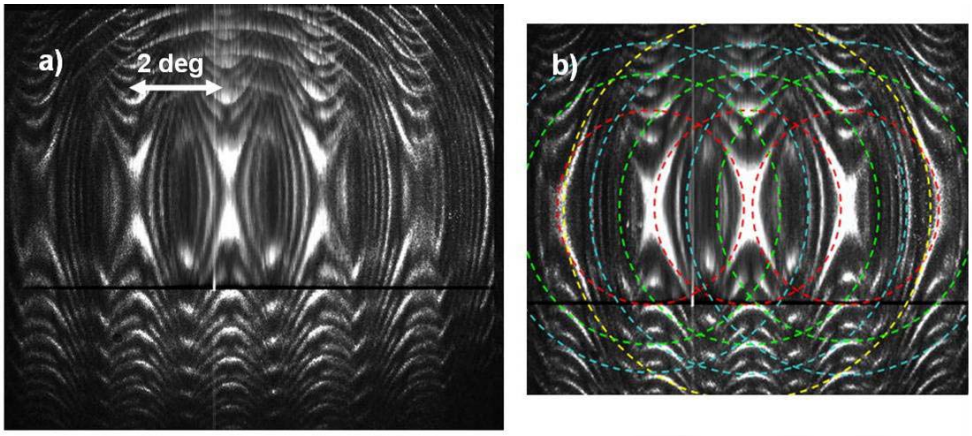


Fig. 3.20. The full transmission spectrum of the resonator containing higher harmonics as obtained experimentally in the far field representation. (a) the dashed circles fit the resonator modes calculated in the limit of weak index modulation. (b) cold resonator modes visible as obtained iluminating a part of notmodulated cavity.

Point scattering method allows us to evaluate resonator transmission profile for different lateral tilt of a resonator gratings. Though almost all experimental our attempts to demonstrate lateral tilt wasn't successful. The reason for it might be slight crossing of a gratings which is hard to escape for small (2 μm and 4 μm) period modulation.

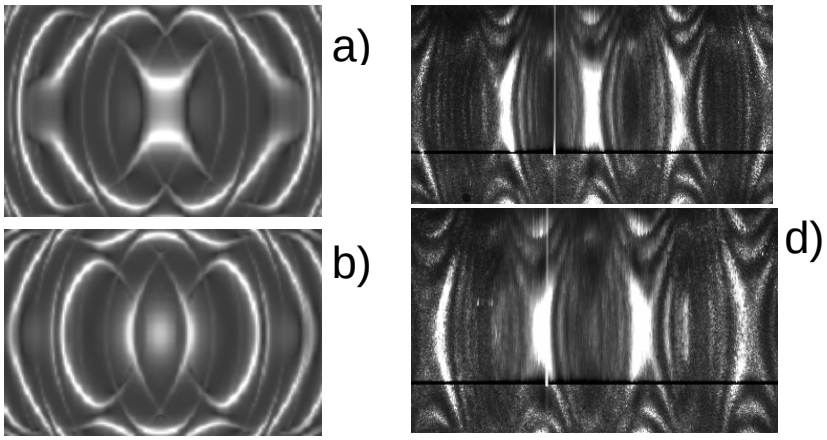


Fig. 3.21. The full transmission spectrum of the resonator with shifted gratings. (a) – represents normal case, then gratings are shifted by $m = \pi$. (b) – $m = 0$ Other parameters for (a), (b) are: $s = 0.4$, $t = 0.45$, $d = 4.5$, $m = \pi$, $\varphi = 0$ (c), (d) experimentaly obtained transmission spectrum.

For 2 μm period grating even 0.01 deg misalignment causes gratings crossing over 1cm modulated area. For a 15 μm grating gratings this misalignment is 0.1 deg. Fig. 3.21 shows resonator transmission profiles with half grating period shifted (a) and not shifted (b) and corresponding experimentally obtained profiles (c, d). Correspondence is fair but still comparable with theory.

Modulation of mirror surface ($d_x$ = 2 μm) implies the critical cavity length of $l_{cr} = d^2/\lambda = 7.5\mu m$. Modulated mirror surface is shown in Fig. 3.14(a). Fig. 3.22 shows the resonator transmission function obtained at around the critical length of the resonator, and by varying the fine tuning condition, as characterized by the roundtrip phase $\varphi = 2lk_0 - 2\pi n$. The roundtrip phase in experiments could not be directly determined, and was indirectly restored from the comparison with the corresponding numerical plots (with explicitly defined phase). The far field of the transmitted radiation as recorded experimentally (left column in Fig. 3.22) is in good qualitative correspondence with calculated numerically (right column in Fig. 3.22). The case (b) corresponds to the multiple resonance of all three waves, i.e. to the case when the frequency of the plateau of dispersion curve is fine-tuned to the

resonance. The cases (a) and (c) are characteristic for situations when the resonator is fine-tuned to the opposite directions from the resonance.

The multiple resonance conditions can be interpreted also in a geometric way. The discussed above rough tuning condition means that the radius of the first Fresnel ring (at resonance) is approximately equal to diffraction angle of a grating of the mirror.

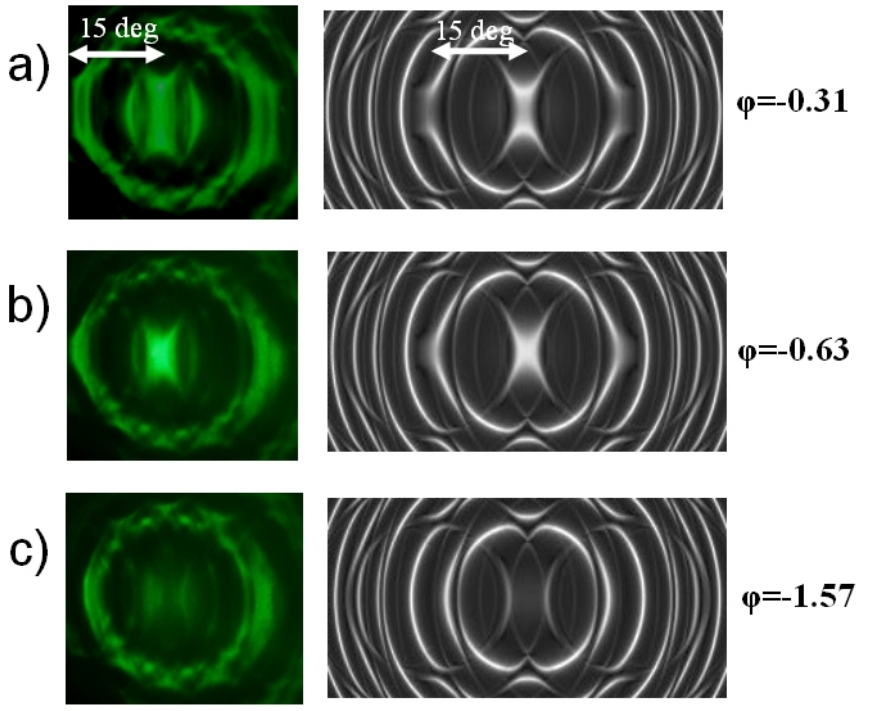


Fig. 3.22. Far field of the radiation transmitted through the resonator with 1D modulated mirror surface as recorded experimentally, and calculated numerically from (3.1.3.11). The lateral shift of the mirrors is a half of modulation period. Parameters used in numerics: $s = 0.4$, $t = 0.2$, $d = 4.0$, $m = \pi$. The resonator roundtrip phase was varied to fit the experimental plots.

The fine tuning condition means that the Fresnel rings from two diffracted components overlap on the spot of the central component. Fig. 3.23 shows the ring structure of the PhC cavity, illustrating the above discussed resonance condition. The ring structure around the diffraction maxima is clearly visible in both numerical and experimental field distributions, and the resulting far-field transmission pattern can be well interpreted with the help of the system of the Fresnel rings.

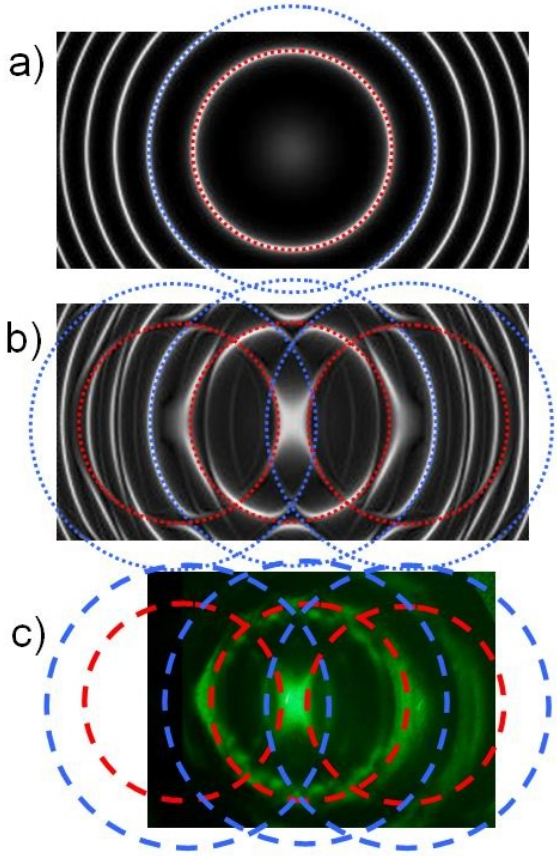


Fig. 3.23. Ring structure of the resonator with 1D modulated mirrors. (a) – cavity ring structure with the absence of a modulation ($S$=0); (b) – numerical simulation of PhC resonator ($s$ = 0.4). Parameters: $t$ = 0.2, $d$ = 4.0, $m$ = π; $\varphi$ = -0.63; (c) - Experimentally obtained resonator transmission. Rings are the same as (a, b) (asymmetry is experimental artifact).

### 3.4. PhC resonators with the single modulated mirror.

It was found during experiments, that a cavity with one modulated mirror also exhibits similar properties as with two modulated mirrors. The principal scheme of such resonator is shown in Fig. 3.24. The first mirror of a resonator is 1D modulated and has two degrees of freedom in order to tilt with respect to optical axes. The second mirror can be tilted with respect optical axes and can be moved along it. From the experimental view it is more convenient since there is no need for precise one grating alignment with respect to another (as in Fig. 3.17). Theoretically single modulated mirror PhC resonator can be analyzed by using mode expansion or point scattering method.

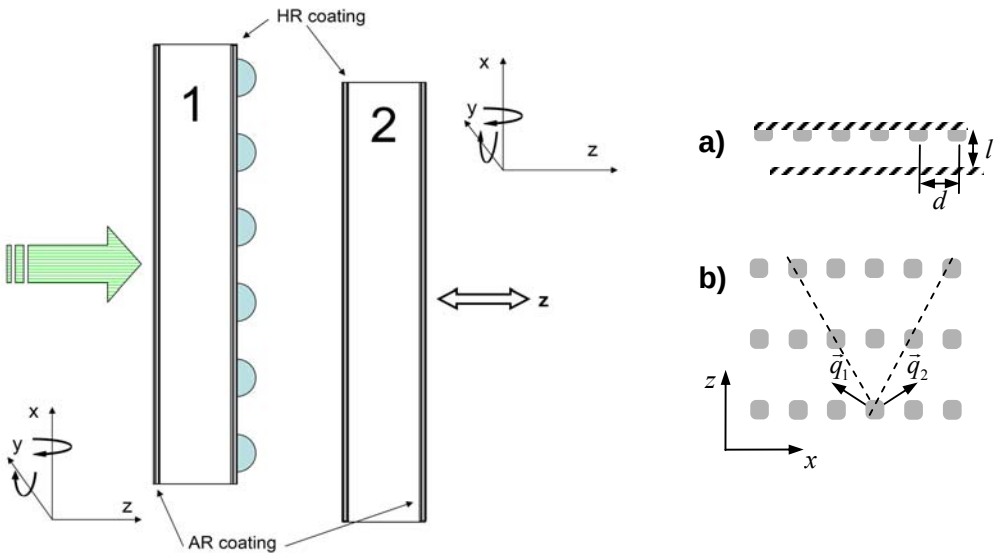


Fig. 3.24. Photonic crystal resonator with a single 1D modulated mirror. (a) – physical construction, (b) corresponding unfolded PhC structure.

Fig. 3.24(b) shows unfolded structure of such a resonator. Point scattering method (presented in chapter 3.1.3) can be easily adopted for single modulated mirror case by removing scattering and shifting operators in formula (3.1.3.11):

$$\hat{T} = t^2\left(\hat{1} - \hat{R}\right)^{-1} = t^2\left(\hat{1} - r^2\hat{P}\hat{P}\hat{S}\right)^{-1}. \qquad (3.4.1)$$

Calculated resonator transmission profile gives basic properties expected: sub-diffraction (Fig 3.25(a)) and super-diffraction (Fig 3.25(c)) The profile shape in general is the same for one and two modulated mirrors resonator (as evaluated in Fig. 3.6 and Fig. 3.7). Optimal resonator length, phase and transmission are slightly different.

For experiments was used 1D modulated 4 μm period mirror. Modulation profile is shown in Fig. 3.14(b) Diffraction efficiency of a grating was 27 % in zero order, 30.5 % in +-first order and 5 % ir the ±second order maxima. Experimental results are in good correspondence with numerical one (Fig. 3.26). In Fig. 3.26(b) filtering regime is evident. All experimentally obtained transmission profiles corresponds well at high resonator mirrors transmission (i.e. low resonator finesse). As it came out analyzing resonator

parameters at chapter 3.1.4 subdiffraction regime can't be evaluated if transmission is high $t = 0.2$. Mirrors actual transmission is $t = 0.015$. It should be enough for sub-diffraction registration, though it fails.

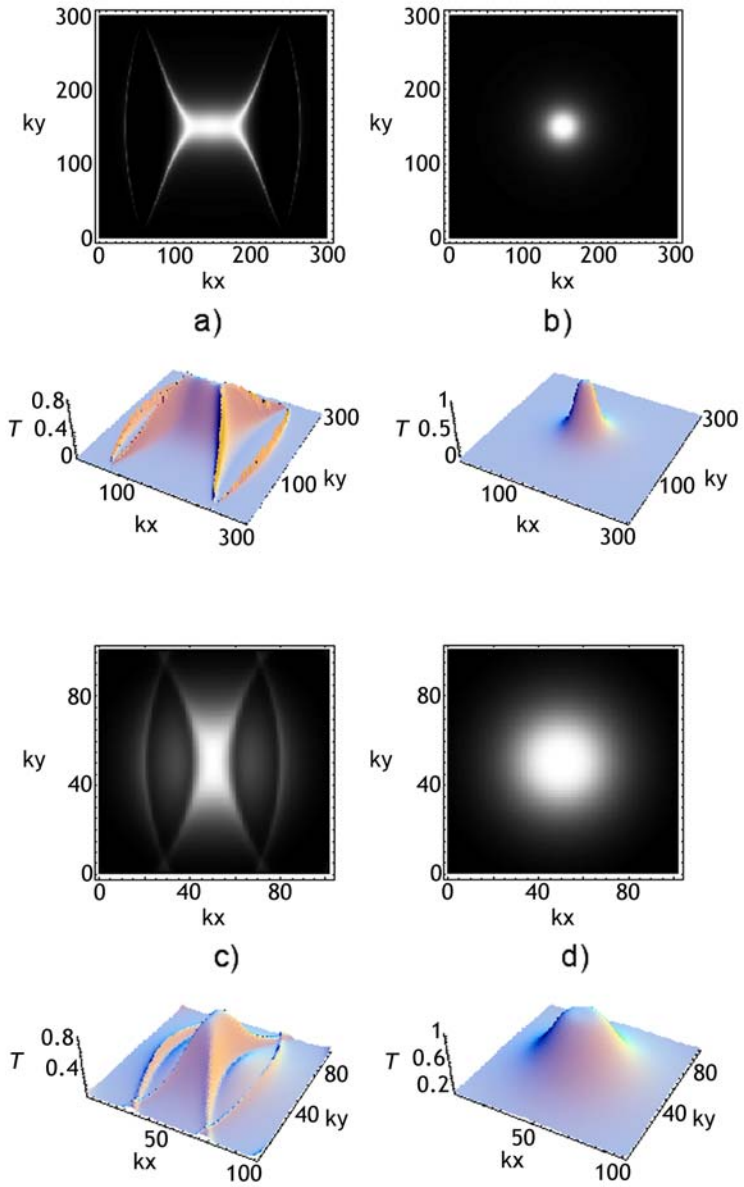


Fig. 3.25. Transmission of a PhC resonator with single modulated mirror counted using point scattering method. (a) shows sub-diffraction angular transmission profiles at length $d = 4.2$ with parameters: $s = 0.4$, $t = 0.01$, $\varphi = -0.1$; (b) is a homogeneous case of (a) at $s = 0$, $\varphi = 0$. (c) shows superdiffraction angular transmission profiles at length $d = 3.7$ with parameters: $s = 0.4$, $t = 0.2$, $\varphi = -0.25$ (d) is a corresponding homogeneous case of (c).

The reason for low finesse seems to be diffraction grating. Profile of a grating isn't strictly harmonic (Fig. 3.14(b, d)) and diffraction efficiency to higher order maxima is 10 % (counting both ±2'd order). This causes losses and reduces finesse of a cavity. Thought qualitative experimental-theoretical correspondence at low finesse shows possible success if appropriate mirrors and modulation parameters achieved.

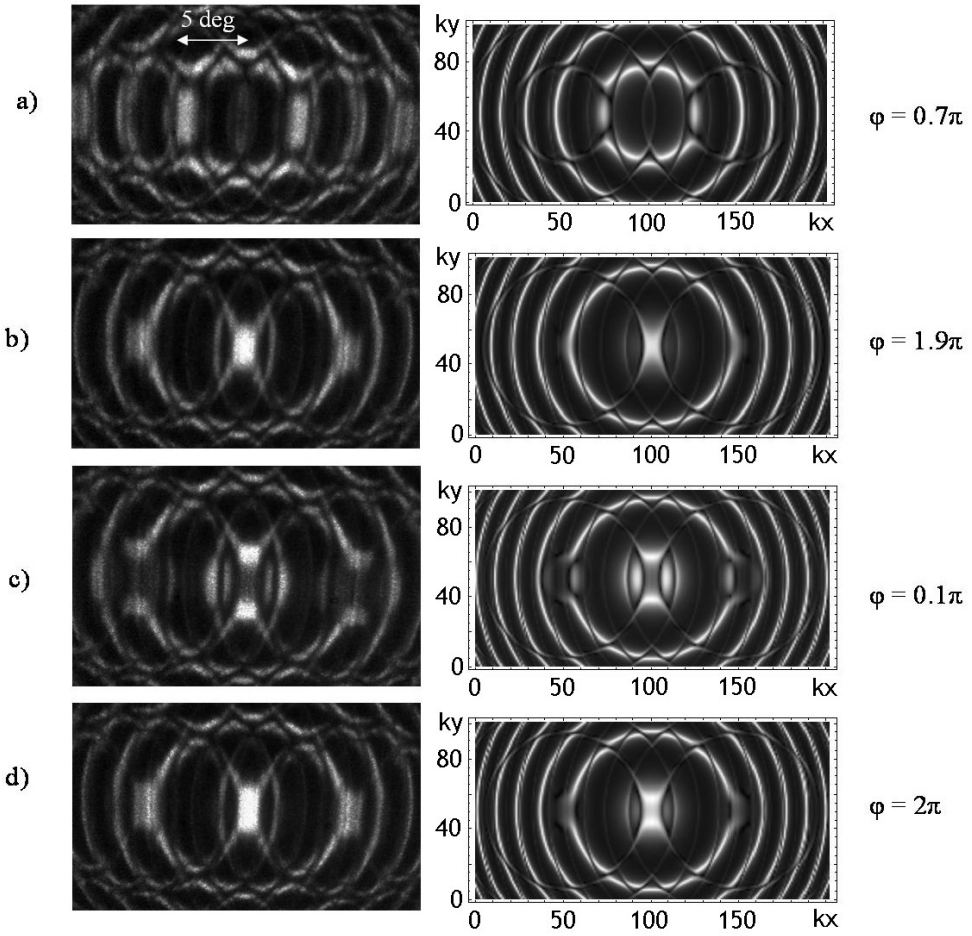


Fig. 3.26. Far field of the radiation transmitted through the resonator with 1D single modulated mirror as recorded experimentally, and calculated numerically. Parameters: $s = 0.4$, $t = 0.2$; physical ant theoretical resonator length $l = 35$ μm (a, b) and $l = 38$ μm (c, d).

### 3.5. PhC resonators with 3D intracavity modulation

In chapter 3.1 2D intracavity modulation resonators were analyzed. In this chapter we extend 2D case into 3D. Principal idea of resonator filling media construction is in Fig. 3.27. Two crossed phase gratings were fabricated on a mirrors and laterally tilted in bought directions by half of a period with respect to another grating.

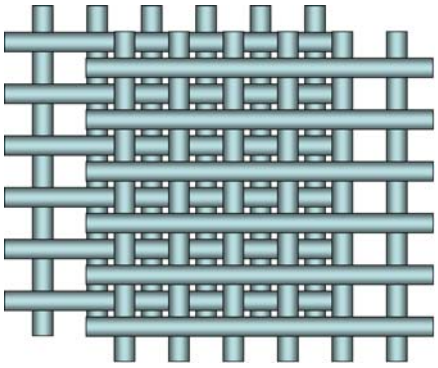

Fig. 3.27. Two 2D modulated gratings shifted by half of a period in *x* and *y* direction

For fabrication of a samples we used *contact UV photolithography technology*. All technological approach is presented in chapter 3.2. The only difference - photoresist is exposed twice after crossing of a photo-mask. AFM image of a fabricated 4 μm period 2D mirror surface modulation is in Fig. 3.28. Diffraction efficiency of a fabricated gratings was 26 % at zero order and ~13 % at four first order maxima. Diffraction efficiency to second order maxima was ~1 %, transmission ~2 %. Other 16 % seams to be scattered to higher order maximas and adds high losses to a cavity.

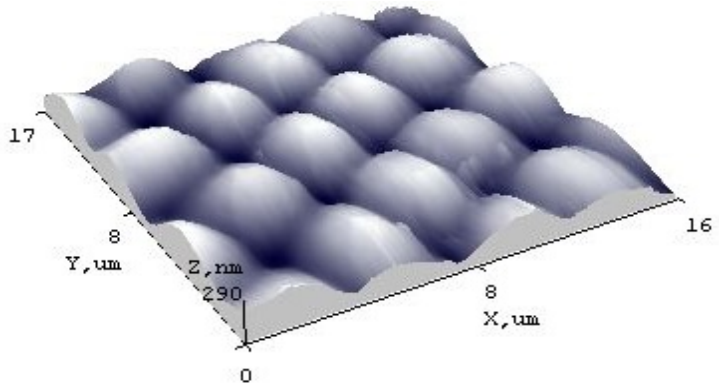


Fig. 3.28. AFM image of a 2D modulated mirror surface

*Theoretical model of 3D PhC resonators*

For the theoretical-numerical analysis of the resonator modes we developed an approach, based on the multiple scattering matrix technique. We analyze a round trip propagation of light along the resonator, and calculate the transformation of the field on each of the elements consecutively: i) the diffraction on the modulated surface of the mirror; ii) the free space propagation between the mirrors (diffraction in homogeneous material); iii) the lateral shift of the periodic structure of the mirrors one with respect to another, iv) the partial reflections from the mirrors. After calculating the field transformation in a resonator roundtrip (by applying the transformation operators, i.e. by multiplying by corresponding transformation matrices), we calculate the resonator transmission matrix by the standard techniques: by adding the entering plane wave to the resonators, and by searching for a stationary state. This is essentially a classical approach to calculate the mode structure of the homogeneously filled Fabry-Perrot resonator, with the difference that the field transformations on each of the element in the resonator now are not the scalars but operators (represented by matrices).

The periodic modulation of the mirror surface results in a set of diffraction components in reflected light with transverse the components of the wavevectors $\vec{k}_\perp + \vec{q}_{m,n}$, here $\vec{k}_\perp = \left(k_x, k_y\right)$ is the transverse wavevector of the incident light, and $\vec{q}_{m,n} = \left(mq_x, nq_y\right)$ are the multiples of the modulation wavevector. Strictly speaking one should consider all the possible field harmonics, however it comes out that the consideration of the central component plus the first order sidebands is sufficient [A5]. For 1D modulation of the mirrors this results in three components (as considered in [A5], for 2D square modulation of the mirrors) in five components [86]. We approximate, therefore, the optical field in the following way:

$$A(\mathbf{r}) = e^{i(k_x x + k_y y)}\left(a_{0,0} + a_{-1,0}e^{-iq_x x} + a_{+1,0}e^{iq_x x} + a_{0,-1}e^{-iq_y y} + a_{0,+1}e^{iq_y y}\right) \qquad (3.5.1)$$

The field is, for convenience, represented by the column-vector of plane wave components:

$$\vec{A} = \left(a_{0,-1}, a_{-1,0}, a_{0,0}, a_{+1,0}, a_{0,+1}\right)^T \qquad (3.5.2)$$

The $q_\perp = (q_x, q_y)$ are the wavevectors of the index modulation in the transverse direction (the field is expanded in its harmonics). In general $q_x$ and $q_y$ can be different one from another, but throughout the article we will consider the square lattice $q_x = q_y = q_\perp$ in the 2D modulation case. The plane-wave set (3.5.2) is tilted with respect to the optical axis, as represented by the factor in (3.5.1) with nonzero $\vec{k}_\perp = (k_x, k_y)$.

Next we list separately all the field transformations in the resonator roundtrip.

**Scattering by the phase grating.** The periodically modulated phase of the field on the reflection of the surface of the mirror couples the components of the field vectors. For the harmonic modulation the coupling occurs between the central component $a_{0,0}$ and the sidebands in this five harmonic model. We introduce the phenomenological scattering coefficients $s_x$ and $s_y$ into the both transverse directions respectively. In the square grating (2D) case $s_x = s_y = s$, and the 1D modulation case by: $s_x = s$, $s_y = 0$. The scattering *s* can be linked to microscopic parameters of the coating, as the depth of the modulation, and the refraction index of the photoresist. However it is more convenient to keep the macroscopic scattering parameter, as it is directly linked with the experimentally accessible diffraction efficiency of the grating (*s* is the square root of the scattering intensity into the sidebands). The scattering matrix is:

$$\hat{S} = Exp\begin{pmatrix} 0 & 0 & is_y & 0 & 0 \\ 0 & 0 & is_x & 0 & 0 \\ is_y & is_x & 0 & is_x & is_y \\ 0 & 0 & is_x & 0 & 0 \\ 0 & 0 & is_y & 0 & 0 \end{pmatrix} \tag{3.5.3}$$

More convenient (for numerical purposes) is however to simplify the scattering operator, which in (3.5.3) is the matrix exponent. The simplification is being done by series expansion of (3.5.3), which truncated to three expansion terms reads:

$$\hat{S} = \begin{pmatrix} 1-s_y^2/2 & -s_x s_y/2 & is_y & -s_x s_y/2 & -s_y^2/2 \\ -s_x s_y/2 & 1-s_x^2/2 & is_x & -s_x^2/2 & -s_x s_y/2 \\ is_y & is_x & 1-s_x^2-s_y^2 & is_x & is_y \\ -s_x s_y/2 & -s_x^2/2 & is_x & 1-s_x^2/2 & -s_x s_y/2 \\ -s_y^2/2 & -s_x s_y/2 & is_y & -s_x s_y/2 & 1-s_y^2/2 \end{pmatrix} \tag{3.5.4}$$

The simplified scattering matrix (3.5.4) is an approximate expression, and therefore does not preserve the energy precisely during the scattering process. The absolute values of eigenvalues of the matrix (3.5.4) are not equal to unity as the truncation introduces errors in the absolute values of eigenvalues of the order of $O(s^4)$. For the experimental values used $s \approx 0.2 \div 0.3$ the nonconservation of the energy is therefore negligible.

**Free propagation.** The free propagation over the linear length of the resonator is considered by the paraxial propagation equation:

$$\partial_z A(\mathbf{r}) = \frac{i}{2k_0} \nabla_\perp^2 A(\mathbf{r}) \tag{3.5.5}$$

where $\nabla_\perp^2 = \partial^2/\partial x^2 + \partial^2/\partial y^2$ is the Laplace operator acting in the transverse plane. Substitution of expansion (3.5.1) into (3.5.5) yields the equation system:

$$\partial_z a_{m,n} = -\frac{i}{2k_0}\left[(mq_x + k_x)^2 + (nq_y + k_y)^2\right] a_{m,n}, \tag{3.5.6}$$

The integration of (3.5.6) over one linear resonator length results to the diagonal transformation matrix:

$$\vec{P} = e^{ilk_0} \cdot Diagonal\left(e^{-iL(k_y+q_y)^2 - iLk_x^2}, e^{-iL(k_x+q_x)^2 - iLk_y^2}, e^{-iLk_x^2 - iLk_y^2}, e^{-iL(k_x-q_x)^2 - iLk_y^2}, e^{-iL(k_y-q_y)^2 - iLk_x^2}\right)$$
, (3.5.7)

Here $L = l/(2k_0)$ is the normalized length of the resonator, representing its diffraction.

**Lateral shift of the mirror.** We account for the lateral shift of the grating (determined by $\vec{m} = (m_x, m_y)$) using the following trick. We fix the reference frame with the position of the first mirror. Then, for the calculation of the scattering from the laterally shifted second mirror we change the reference frame, by applying the operator:

$$\vec{M} = Diagonal\left(e^{+im_y q_y}, e^{+im_x q_x}, 1, e^{-im_x q_x}, e^{-im_y q_y}\right) \quad (3.5.8)$$

Then, after calculation the scattering on the second mirror (by using (3.5.3) or (3.5.4)) in the new reference frame), we restore the original reference frame, by applying $\vec{M}^{-1}$.

**Resonator mirrors.** Since the reflectivity is the same for all harmonic components of the wave, it is accounted in a standard way – by multiplication by a scalar $r$. Without losing generality in theory, and in accordance to our experiment, we consider the both mirrors of the same reflectivity.

**Resonator roundtrip.** The variation of the field in a resonator roundtrip is calculated by applying consecutively all the operators discussed above:

$$\hat{R} = r^2 \hat{P}\hat{M}^{-1}\hat{S}\hat{M}\hat{P}\hat{S} \quad (3.5.9)$$

**Resonator transfer function.** The plane wave entering into the resonator is denoted in this vector form by $\vec{A}_0 = (0,0,B_0,0,0)^T$. Then we calculate the

radiation balance in one resonator roundtrip, and analogously to the homogeneous Fabry-Perot case, we obtain:

$$\vec{A} = t\left(\hat{1} - \hat{R}\right)^{-1} \vec{A}_0 \qquad (3.5.10)$$

for the radiation at the entrance mirror. The only difference from the homogeneous Fabry-Perot case is that here we deal with the vectors of the wave components and transformation matrices, instead of complex scalar factors. Finally the resonator transmission matrix is:

$$\hat{T} = t^2\left(\hat{1} - \hat{R}\right)^{-1} = t^2\left(\hat{1} - r^2\hat{M}^{-1}\hat{P}\hat{S}\hat{M}\hat{P}\hat{S}\right)^{-1} \qquad (3.5.11)$$

The transmission for the homogeneous component is given by the element $T_{0,0}$ of the transfer matrix (3.5.11). The scattering of the resonator into the sidebands harmonics is described by the corresponding off-diagonal column elements of the matrix: by $T_{-1,0}$ and $T_{+1,0}$ into the diffraction components in x direction, and by $T_{0,-1}$ and $T_{0,+1}$ into the diffraction components in y direction.

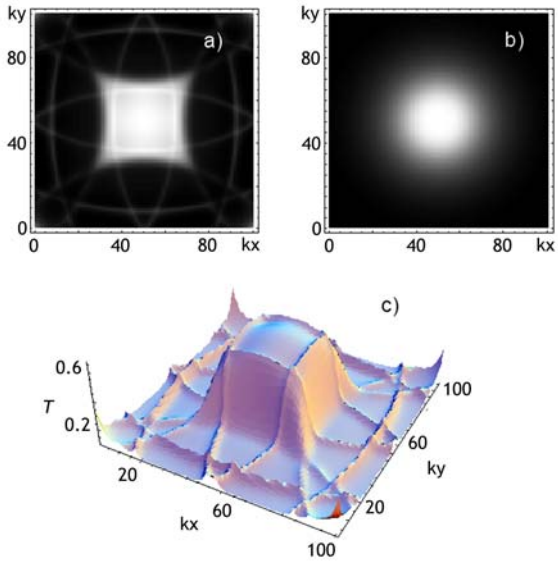


Fig. 3.29. Rectangular transmission profile of a 3D modulated PhC resonator (a, c) Parameters: $s = 0.4$, $t = 0.2$, $d = 4.5$, $m_x = \pi$, $m_y = \pi$; $\varphi(a,c) = -0.78$. Homogeneous resonator transmission (b).

Typical calculated 3D resonator transmission profile is shown in Fig. 3.29(a, c). Parameter analysis shows basic 2D modulated resonator properties. By changing the length of cavity and tuning the phase we can obtain subdiffraction or superdiffraction regime (Fig. 3.30(a)) Maximum transmission for cavity length $d = 4.6$ can reach 90 %. Fig. 3.30(b) shows near flat top transmission profiles for $s = 0.35$ and $s = 0.25$ diffraction efficiency. For a higher and lower diffraction efficiency flat top

can't be evaluated for Fig 3.3(b) parameters set. Analogically to 2D single modulated mirror case (chapter 3.4) 3D resonator can also be calculated for single mirror approach. Fig. 3.30(b) also shows calculated case of single modulated mirror transmission.

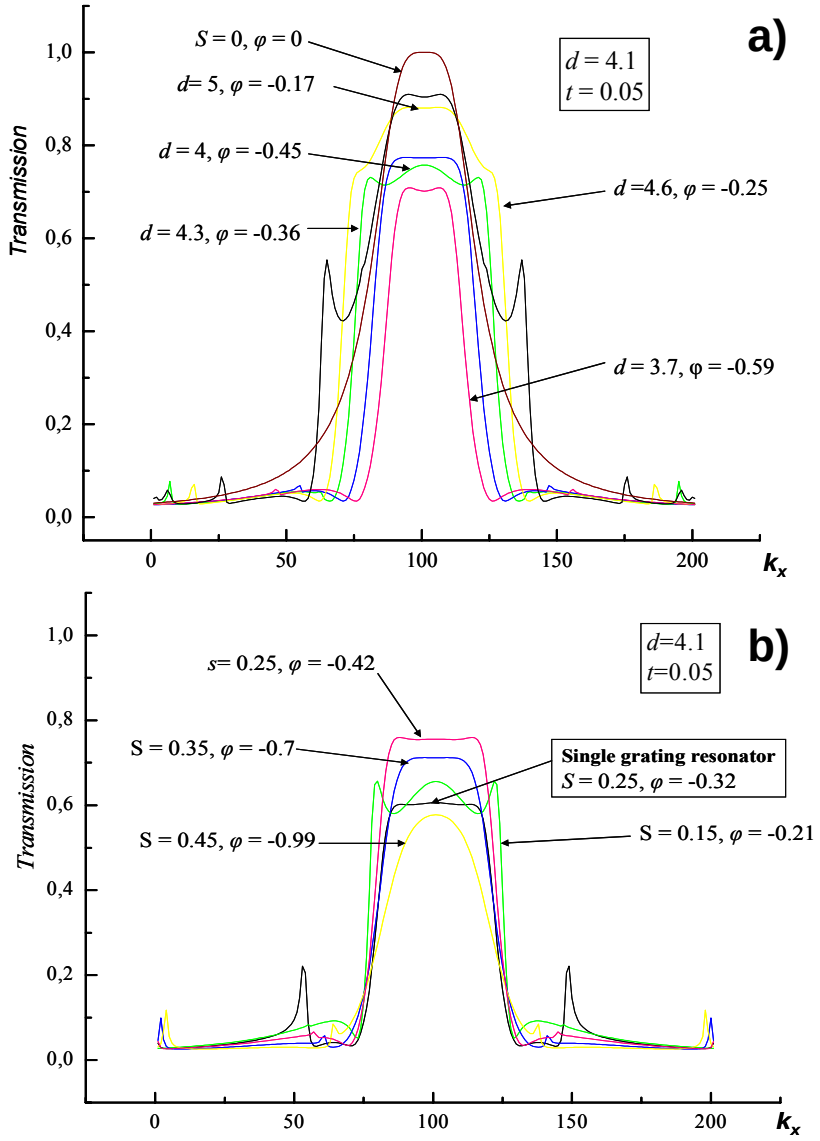


Fig. 3.30. 3D resonator parameter analysis. (a) – transmission cross section dependence on a cavity length. (b) transmission cross section dependence on a diffraction efficiency. Phase is turned for maximum transmission and flat top.

### 3.6. Experimental analysis of 3D PhC resonators

In 3D experiments the periods of the modulation of mirror surface was ($d_x = 4$ μm, $d_y = 4$ μm ), (quadratic structure Fig. 3.28), which implies the critical cavity length of $l_{cr} = d^2/\lambda = 30\mu m$. Fig. 3.31 shows the resonator transmission function obtained at around the critical length of the resonator, and by varying the fine tuning condition. Also in 2D modulation case a good qualitative correspondence with numerically obtained results was observed. Here again, the resonant case was obtained, characterized by relatively flat (homogeneous) and broad resonator transmission function. This case is analogous to the case in Fig. 3.6(c), however here obtained as a simultaneous resonance of the five waves. Also in analogy to 2D cases the typical off-resonance transmission distribution were obtained, and shown in Fig. 3.31(b, c).

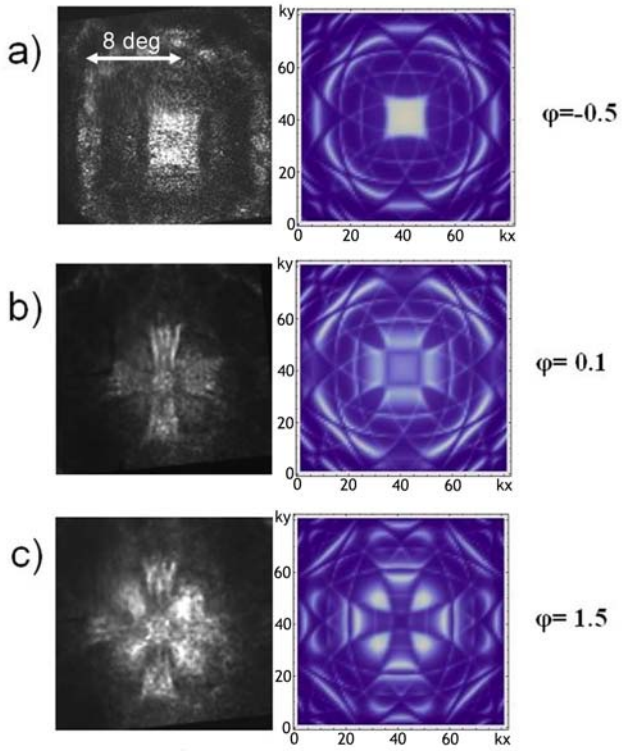


Fig. 3.31. Far field of the radiation transmitted through the resonator with 2D modulated mirrors as recorded experimentally, and calculated numerically (3.5.9). The lateral shift of the mirrors is a half of modulation period in both directions ($m_x = m_y = \pi$). Parameters: $S = 0.4$, $T = 0.2$, $d = 4.5$.

The multiple resonance condition, and the appearance of plateau can be also interpreted in a geometric way, like in 2D modulation case. Differently from 2D case, here it seems that the most homogeneous plateau appears under participation of the two resonant rings from the diffraction maxima, as indicated in Fig. 3.32. This means, that also the longitudinal $n - 2$ modes participate in formation of sub-diffractive pattern.

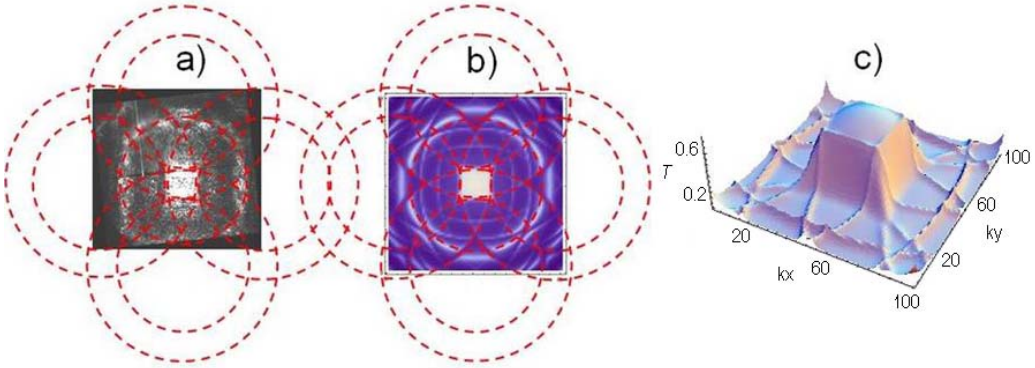


Fig. 3.32. Ring structure of 2D modulated mirrors cavity. Experimental results (a) and numerical simulation (b) as taken from Fig.5. Dashed red rings indicate imaginary place of transmission rings around diffraction maxima. (c) shows 3D resonator transmission structure, showing the role of two resonance rings, as obtained from numerics of Eq. (3.5.11).

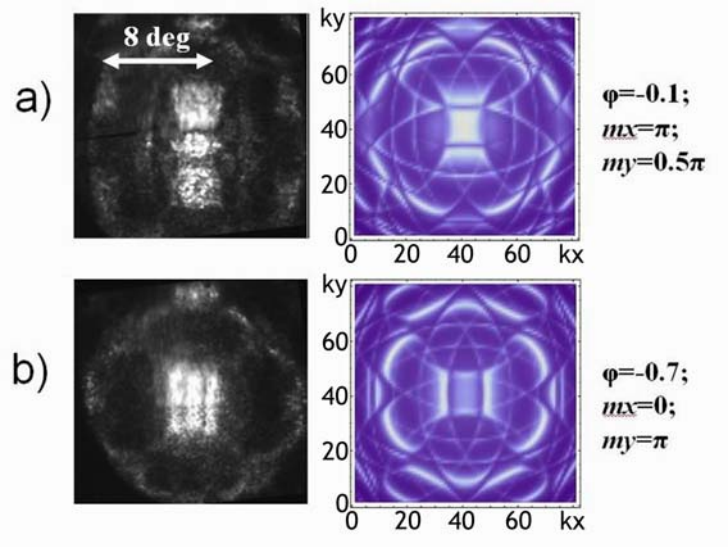


Fig. 3.33. Far field of the radiation transmitted through the resonator with 2D modulated mirrors and different lateral shift as recorded experimentally, and calculated numerically (3.5.11). Parameters: $s = 0.4$, $t = 0.2$, $d = 4.5$.

The resonator transmission pattern was sensible with respect to the lateral shift of the resonator mirrors one with respect to another. Fig. 3.33 reports the result of study of the lateral shift. As expected, the lateral shift by the value different than $m_{x,y} = \pi, 0.5\pi$ results in asymmetric pattern with respect to the direction with broken symmetry (Fig. 3.33(a). The lateral shifts of $m_{x,y} = 0$ and $m_y = \pi$ results in different patterns, as shown in Fig. 3.33(b).

### 3.7 Conclusions

Concluding, we build the PhC resonator with the intracavity modulation of refraction index, i.e. the resonator containing one longitudinal period of the PhC for the first time. We develop the method of the calculation of such resonator, based on the scattering matrix theory, and we reproduce the experimentally observed transmission patterns by numerical integration of the developed model. We demonstrate experimentally the basic properties expected, i.e. the hyperbolic shape transmission patterns in case of 1D modulation of the mirror surfaces, and square shape patterns in case of 2D modulation of the mirror surfaces.

The PhC resonator shows basic properties expected – the relatively flat angular transmission profile. The maximum transmission area is of quadratic shape, due to a quadratic symmetry of the modulation of the mirror surfaces. The more symmetric modulation patterns (hexagonal, or octagonal) are expected to result in a more isotropic transmission spot.

Finally, the resonators investigated here can be used to observe the nonlinear subdiffractive effects. The investigation of the nonlinear effects in diffraction manipulated systems already have been started investigated (hyperbolic patterns in optics [88], hyperbolic patterns in Bose-Einstein Condensate [89]). Also the nonlinear effects (modification of instabilities) in the resonators with the refraction index modulated in one transverse direction were investigated (in 1D PCs in resonators with $\chi^{(2)}$ [90] and $\chi^{(3)}$ [91]

nonlinearities). The nonlinear resonators with “true” photonic crystals, the 2D as in the present chapter, or also 3D, however, never been investigated up to now. In particular the significant narrowing of nonlinear structures (solitons) in subdiffractive regimes, and significant enhancement of spatial stability of the structures in filtering regimes, can be expected.

## List of results and conclusions

1. Optical parametrical oscillation (OPO) in a large Fresnel number monolithic BBO type I phase matching crystal mini-cavity was demonstrated experimentally. It was shown, that OPO emission is conical and multiconical and depends on the cavity optical axes orientation with respect to the pump beam and on cavity detuning to laser frequency. In case of increasing angle between cavity optical axes and pump beam in phase matching direction conical emission angle increases abruptly at values $0{,}68^0 \pm 0{,}01^0$; $0{,}75^0 \pm 0{,}01^0$ and two pairs of signal and idler waves are emitted. In case of changing angle between cavity optical axes and pump beam in not phase matching direction $\pm 1^0$ signal and idler waver rotates around pump beam near $180^0$. OPO threshold rises up to 15 mJ (36 MW/cm$^2$) if angle between cavity optical axes and pump beam exceeds $0.5^0$ in not phase matching direction. Developed theoretical model can explain and reproduce behavior of OPO emission.
2. Stabilization of the stripes (rolls) pattern in large Fresnel number ($N > 100$) BBO type I degenerate OPO was achieved by a week injection at subharmonic frequency. Measured temporal spectra of roll pattern shows 1/f like power spectra
3. Adding periodical refraction index modulation on a resonator plane mirror surfaces is a convenient method for PhC resonators fabrication.
4. Diffraction properties of photonic crystal resonators depends on cavity length, diffraction efficiency of a gratings, gratings tilt and cavity mirrors reflection coefficient. In case cavity length is near critical $l_{cr} = d^2/\lambda$ the PhC resonator shows basic properties expected - sub and superdiffractive dynamics of light in the resonator, and in hyperbolic angular transmission profiles in case of 1D modulation of the mirror

surfaces, and square shape angular transmission profiles in case of 2D modulation of the mirror surfaces.

5. The developed calculation method, based on the scattering matrix theory is capable to qualitatively reproduce transmission profiles of all PhC resonator types, including PhC resonators with single modulated mirror and it is suitable method for studying and predicting diffraction properties of photonic crystal resonators.

## References


[1] S. Ducci, N. Treps, A. Maitre and C. Fabre, Pattern formation in optical parametric oscillators, Physical Review A **64**(2), 023803 (2001).

[2] M. Vaupel, A. Maotre and C. Fabre, Observation of Pattern Formation in Optical Parametric Oscillators, Physical Review Letters **83**(25), 5278 LP - 5281 (1999).

[3] V. Sirutkaitis, R. Grigonis, G. Slekys and K. Staliunas, Spatial structures in synchronously pumped optical parametric oscillators, Journal of Optics B: Quantum and Semiclassical Optics **1**(1), 139 (1999).

[4] K. Staliunas and M. Tlidi, Hyperbolic transverse patterns in nonlinear optical resonators, Physical Review Letters **94**(13), 133902 (2005).

[5] M. C. Cross and P. C. Hohenberg, Pattern formation outside of equilibrium, Reviews of Modern Physics **65**(3), 851 LP - 1112 (1993).

[6] L. Rayleigh, On the dynamics of rotating fluid., Proc. Roy. Soc. **93** 148 (1916).

[7] L.V.Belousov, *Self-organization, autowaves and structures far from equilibrium* (Springer-Verlag, Berlin, 1984).

[8] A.Turing, Philos. Trans. R. Soc. London B **237**(37), (1952).

[9] G. F. Oster, Lateral inhibition models of developmental processes, Mathematical Biosciences **90**(1-2), 265 (1988).

[10] M. Faraday, On a peculiar class of acoustical figures; and on certain forms assumed by groups of particles upon vibrating elastic surfaces, Philosophical Transactions of the Royal Society of London (1776-1886) **121**(1831), 299 (1831).

[11] P. Coullet, T. Frisch and G. Sonnino, Dispersion-induced patterns, Physical Review E **49**(3), 2087 LP - 2090 (1994).

[12] A. C. Newell and J. A. Whitehead, Finite bandwidth, finite amplitude convection, Journal of Fluid Mechanics **38**(02), 279 (1969).

[13] K. Staliunas and V. J. Sanchez-Morcillo, *Transverse Patterns in Nonlinear Optical Resonators* (Springer, Berlin 2003).

[14] K. Staliunas, Laser Ginzburg-Landau equation and laser hydrodynamics, Physical Review A **48**(2), 1573 (1993).

[15] K. Staliunas and C. O. Weiss, Tilted and standing waves and vortex lattices in class-A lasers, Physica D: Nonlinear Phenomena **81**(1-2), 79 (1995).

[16] K.Staliunas, Transverse pattern formation in optical parametric oscillators, Journal of Modern Optics **42** 1261 (1995).

[17] K. Staliunas, M. F. H. Tarroja, G. Slekys, C. O. Weiss and L. Dambly, Analogy between photorefractive oscillators and class-A lasers, Physical Review A **51**(5), 4140 (1995).

[18] J. Malos, M. Vaupel, K. Staliunas and C. O. Weiss, Dynamical structures of a photorefractive oscillator, Physical Review A **53**(5), 3559 (1996).

[19] G. J. de Valcarcel, K. Staliunas, E. Roldan and V. J. Sanchez-Morcillo, Transverse patterns in degenerate optical parametric oscillation and degenerate four-wave mixing, Physical Review A **54**(2), 1609 (1996).
[20] V. J. Sanchez-Morcillo, E. Roldan, G. J. de Valcarcel and K. Staliunas, Generalized complex Swift-Hohenberg equation for optical parametric oscillators, Physical Review A **56**(4), 3237 (1997).
[21] K.Staliunas, Localized structures in degenerate optical parametric oscillators, Optics Communications **139**(4-6), 306 (1997).
[22] K. Staliunas, Stabilization of spatial solitons by gain diffusion, Physical Review A **61**(5), 053813 (2000).
[23] G.J.de Valcarcel, E.Roldan and K.Staliunas, Cavity solitons in nondegenerate optical parametric oscillators, Optics Communications **181**(1-3), 207 (2000).
[24] C.O. Weiss, M. Vaupel, K. Staliunas, G. Slekys and V. B. Taranenko, Solitons and vortices in lasers, Applied Physics B **68**(2), 151-168 (1999).
[25] J. A. Arnaud, Degenerate optical cavities, Applied Optics **8**(1), 189 (1969).
[26] V. B. Taranenko, K. Staliunas and C. O. Weiss, Spatial soliton laser: Localized structures in a laser with a saturable absorber in a self-imaging resonator, Physical Review A **56**(2), 1582 (1997).
[27] K. Staliunas, V. B. Taranenko, G. Slekys, R. Viselga and C. O. Weiss, Moving spatial solitons in active nonlinear-optical resonators, Physical Review A **57**(1), 599 (1998).
[28] G. Slekys, K. Staliunas and C. O. Weiss, Spatial localized structures in resonators with saturable absorber, Optics Communications **149** 113 (1998).
[29] J. Lega, J. V. Moloney and A. C. Newell, Swift-Hohenberg Equation for lasers, Physical Review Letters **73**(22), 2978 (1994).
[30] K. Staliunas, A. Berzanskis and V. Jarutis, Vortex statistics in optical speckle fields, Optics Communications **120**(1-2), 23 (1995).
[31] P. Coullet, T. Frisch and F. Plaza, Sources and sinks of wave patterns, Physica D: Nonlinear Phenomena **62**(1-2), 75 (1993).
[32] K. Staliunas, G. Slekys and C. O. Weiss, Nonlinear pattern formation in active optical systems: shocks, domains of tilted waves, and cross-roll patterns, Physical Review Letters **79**(14), 2658 (1997).
[33] K. Staliunas and V. J. Sanchez-Morcillo, Spatial-localized structures in degenerate optical parametric oscillators, Physical Review A **57**(2), 1454 (1998).
[34] K. Staliunas and V. J. Sanchez-Morcillo, Dynamics of phase domains in the Swift-Hohenberg equation, Physics Letters A **241**(1-2), 28 (1998).
[35] W. V. Saarloos and P. C. Hohenberg, Fronts, pulses, sources and sinks in generalized complex Ginzburg-Landau equations, Physica D: Nonlinear Phenomena **56**(4), 303 (1992).

[36] S. Trillo, M. Haelterman and A. Sheppard, Stable topological spatial solitons in optical parametric oscillators, Optics Letters **22**(13), 970 (1997).
[37] V. B. Taranenko, K. Staliunas and C. O. Weiss, Pattern Formation and Localized Structures in Degenerate Optical Parametric Mixing, Physical Review Letters **81**(11), 2236 (1998).
[38] E. Yablonovitch, Inhibited Spontaneous Emission in Solid-State Physics and Electronics, Physical Review Letters **58**(20), 2059 (1987).
[39] E. Yablonovitch and T. J. Gmitter, Photonic band structure: The face-centered-cubic case, Physical Review Letters **63**(18), 1950 (1989).
[40] E. Yablonovitch, T. J. Gmitter and K. M. Leung, Photonic band structure: The face-centered-cubic case employing nonspherical atoms, Physical Review Letters **67**(17), 2295 (1991).
[41] E. Yablonovitch, T. J. Gmitter, R. D. Meade, A. M. Rappe, K. D. Brommer and J. D. Joannopoulos, Donor and acceptor modes in photonic band structure, Physical Review Letters **67**(24), 3380 (1991).
[42] E. Yablonovitch, Photonic band-gap structures, J. Opt. Soc. Am. B **10**(2), 283 (1993).
[43] E. Yablonovitch, Photonic band-gap crystals, Condens. Matter **5** 2443 (1993).
[44] J. D. Joannopoulos, R. D. Meade and J. N. Winn, *Photonic Crystals: Molding the Flow of Light* (Princeton University Press, Princeton, NJ, 1995).
[45] J. D. Joannopoulos, Pierre R. Villeneuve and S. Fan, Photonic crystals: putting a new twist on light, Nature **386** 143 (1997).
[46] C.Kittel, *Introduction to Solid State Physics*, 8 edn. (John Wiley & Sons, 2005).
[47] V. Mizeikis, S. Juodkazis, A. Marcinkevicius, S. Matsuo and H. Misawa, Tailoring and characterization of photonic crystals, Journal of Photochemistry and Photobiology C: Photochemistry Reviews **2** 35 (2001).
[48] H. S. Eisenberg, Y. Silberberg, R. Morandotti and J. S. Aitchison, Diffraction Management, Physical Review Letters **85**(9), 1863 (2000).
[49] R. Morandotti, H. S. Eisenberg, Y. Silberberg, M. Sorel and J. S. Aitchison, Self-focusing and defocusing in waveguide arrays, Physical Review Letters **86**(15), 3296 (2001).
[50] H. Kosaka, T. Kawashima, A. Tomita, M. Notomi, T. Tamamura, T. Sato and S. Kawakami, Self-collimating phenomena in photonic crystals, Applied Physics Letters **74**(9), 1212 (1999).
[51]T. Pertsch, T. Zentgraf, U. Peschel, A. Brauer and F. Lederer, Anomalous refraction and diffraction in discrete optical systems, Physical Review Letters **88**(9), 093901 (2002).
[52] D. Chigrin, S. Enoch, Sotomayor and G. R. Tayeb, Self-guiding in two-dimensional photonic crystals, Opt. Express **11**(10), 1203 (2003).

[53] R. Iliew, C. Etrich, U. Peschel, F. Lederer, M. Augustin, H. J. Fuchs, D. Schelle, E. B. Kley, S. Nolte and A. Tunnermann, Diffractionless propagation of light in a low-index photonic-crystal film, Applied Physics Letters **85**(24), 5854 (2004).
[54] K. Staliunas and R.Herrero, Nondiffractive propagation of light in photonic crystals, Physical Review E **73** 016601 (2006).
[55] H. Kosaka, T. Kawashima, A. Tomita, M. Notomi, T. Tamamura, T. Sato and S. Kawakami, Superprism phenomena in photonic crystals, Physical Review B **58**(16), R10096 (1998).
[56] S. Johnson and J. Joannopoulos, Block-iterative frequency-domain methods for Maxwell's equations in a planewave basis, Opt. Express **8**(3), 173 (2001).
[57] K. Staliunas, Dynamics of optical vortices in a laser beam, Optics Communications **90**(1-3), 123 (1992).
[58] G.-L. Oppo, M. Brambilla, D. Camesasca, A. Gatti and L. A. Lugiato, Spatiotemporal dynamics of optical parametric oscillators, Journal of Modern Optics **41**(6), 1151 (1994).
[59] S. Longhi and A. Geraci, Swift-Hohenberg equation for optical parametric oscillators, Physical Review A **54**(5), 4581 (1996).
[60] M. Tlidi, P. Mandel and M. Haelterman, Spatiotemporal patterns and localized structures in nonlinear optics, Physical Review E **56**(6), 6524 (1997).
[61] C. Etrich, U. Peschel and F. Lederer, Pattern formation in intracavity second-harmonic generation, Physical Review E **56**(4), 4803 LP - 4808 (1997).
[62] C. Etrich, U. Peschel and F. Lederer, Solitary waves in quadratically nonlinear resonators, Physical Review Letters **79**(13), 2454 (1997).
[63] P. Lodahl and M. Saffman, Pattern formation in singly resonant second-harmonic generation with competing parametric oscillation, Physical Review A **60**(4), 3251 (1999).
[64] M. Tlidi, P. Mandel and R. Lefever, Kinetics of localized pattern formation in optical systems, Physical Review Letters **81**(5), 979 (1998).
[65] A. V. Mamaev, P. Lodahl and M. Saffman, Observation of spatial modulation instability in intracavity second-harmonic generation, Opt. Lett. **28**(1), 31 (2003).
[66] S. Longhi, Spatio-temporal instabilities and threshold condition in a broad-area optical parametric oscillator, Optics Communications **153** 90 (1998).
[67] L. Lugiato, C. Oldano, C. Fabre, E. Giacobino and R. Horowicz, Bistability, self-pulsing and chaos in optical parametric oscillators, Il Nuovo Cimento D **10**(8), 959 (1988).
[68] P. K. Jakobsen, J. V. Moloney, A. C. Newell and R. Indik, Space-time dynamics of wide-gain-section lasers, Physical Review A **45**(11), 8129 (1992).

[69] K. Staliunas, Opticalk vortices during three-wave nonlinear coupling, Optics Communications **91**(1-2), 82 (1992).
[70] A. V. Mamaev and M. Saffman, Pattern formation in a linear photorefractive oscillator, Optics Communications **128**(4-6), 281 (1996).
[71] L. Rayleigh, On the dynamics of rotating fluid, Proc. R Soc. London Ser A **93** 148 (1916).
[72] R. C. DiPrima and H. L. Swinney, *in Hydrodynamical instabilities and the Transition to Turbulence* (Springer-Verlag, New York, 1981).
[73] G.-L. Oppo, M. Brambilla and L. A. Lugiato, Formation and evolution of roll patterns in optical parametric oscillators, Physical Review A **49**(3), 2028 (1994).
[74] J. Swift and P. C. Hohenberg, Hydrodynamic fluctuations at the convective instability, Physical Review A **15**(1), 319 (1977).
[75] A. C. Newell and J. A. Whitehead, Finite bandwidth, finite amplitude convection, Journal of Fluid Mechanics **38**(2), 279 (1969).
[76] L. A. Segel, Distant side-walls cause slow amplitude modulation of cellular convection, Journal of Fluid Mechanics **38,** 203 (1969).
[77] P. Dutta and P. M. Horn, Low-frequency fluctuations in solids: 1f noise, Reviews of Modern Physics **53**(3), 497 (1981).
[78] Sh. M. Kogan, Low-frequency fluctuations in solids: 1/f noise, Sov.Phys.Usp. **28**(2), 170 (1985).
[79] M. B. Weissman, 1/f noise and other slow, nonexponential kinetics in condensed matter, Reviews of Modern Physics **60**(2), 537 (1988).
[80] K. Staliunas, Spatial and temporal noise spectra of spatially extended systems with order-disorder phase transitions, Int. Journal of Bifurcation and Chaos **11**, 2845 (2001).
[81] K. Staliunas, Spatial and temporal spectra of noise driven stripe patterns, Physical Review E **64**(6), 066129 (2001).
[82] S. John, Strong localization of photons in certain disordered dielectric superlattices, Physical Review Letters **58**(23), 2486 (1987).
[83] M. J. Ablowitz and Z. H. Musslimani, Discrete diffraction managed spatial solitons, Physical Review Letters **87**(25), 254102 (2001).
[84] K. Staliunas, R. Herrero and G. J. d. Valcarcel, Subdiffractive band-edge solitons in Bose-Einstein condensates in periodic potentials, physical Review E **73** 065603(R) (2006).
[85] K. Staliunas, Y. Loiko, R. Herrero, C. Cojocaru and J. Trull, Efficient parametric amplification of narrow beams in photonic crystals, Optics. Letters. **32**(14), 1992 (2007).
[86] K. Staliunas, R. Herrero and G. J. de Valcarcel, Arresting soliton collapse in two-dimensional nonlinear Schrodinger systems via spatiotemporal modulation of the external potential, Physical Review A (Atomic, Molecular, and Optical Physics) **75**(1), 011604 (2007).

[87] M. Andrulevicius, T. Tamulevicius, V. Kopustinskas, A. Guobiene, A. Sileikaite, A. Gudonyte, L. Puodziukynas and S. Tamulevicius, Application of plasma chemical etching in control of optical properties of multilayered dielectric gratings, Materials Science (Medziagotyra) **14**(3), 198 (2008).
[88] K. Staliunas and M. Tlidi, Hyperbolic transverse patterns in nonlinear optical resonators, Physical Review Letters **94**(13), 133902 (2005).
[89] C. Conti and S. Trillo, Nonspreading wave packets in three dimensions formed by an ultracold Bose gas in an optical lattice, Physical Review Letters **92**(12), 120404 (2004).
[90] D. Gomila, R. Zambrini and G.-L. Oppo, Photonic band-gap inhibition of modulational instabilities, Physical Review Letters **92**(25), 253904 (2004).
[91] D. Gomila and G.-L. Oppo, Coupled-mode theory for photonic band-gap inhibition of spatial instabilities, Physical Review E (Statistical, Nonlinear, and Soft Matter Physics) **72**(1), 016614(2005).

**Summary**

This Ph.D. thesis contains experimental and theoretical analysis of nonlinear optical pattern formation in monolithic mini-cavity optical parametrical oscillators and spatial properties of linear photonic crystal resonators. The thesis consists of introduction, literature review and two chapters. In the first chapter experimental investigation of optical parametrical oscillation (OPO) in broad aperture monolithic (5x5x1.5 mm) BBO type I crystal mini-cavity is described. OPO was pumped by second harmonic (532 nm) 13 ns duration, 7-15 mJ energy pulses, of Nd:YAG laser. Optical patterns were registered in a near and far field of OPO emission. Experiments and theoretical interpretation revealed that emission of such resonator can be conical and multiconical and direction of signal and idler waves can be controlled by changing the mini-cavity orientation with respect to pump beam. It was also showed, that the stabilization of stripes (or roll) pattern can be achieved by a weak seed injection at subharmonic frequency and temporal spectrum of the stripe pattern degenerate OPO emission is 1/f – like noise spectrum . In the second chapter plane-mirror Fabry-Pérot resonators filled with a single period of photonic crystal (PhC) are introduced and analyzed. PhC resonators are realized by adding periodical 2 μm, 4 μm and 15 μm refraction index modulation on a resonator mirror surfaces (i.e. fabricating 1D or 2D phase diffraction grating). PhC resonator angular transmission measured by using broad spatial spectrum of 532 nm wavelength CW laser. Mode expansion and scattering matrix methods were used for the theoretical analysis of PhC resonator. The results show that diffraction properties of PhC resonators can be manipulated, resulting in sub- and superdiffractive dynamics of light in the resonator.

**Summary in Lithuanian**

Šioje disertacijoje teoriškai ir eksperimentiškai tiriamas erdvinių šviesos darinių formavimasis didelės apertūros monolitiniuose parametriniuose šviesos generatoriuose (PŠG), nagrinėjamos fotoninių kristalų (FK) rezonatorių erdvinės dispersijos savybės. Darbas susideda iš įvado, literatūros apžvalgos ir dviejų pagrindinių dalių. Pirmoje dalyje aprašomas PŠG tyrimas didelės apertūros (5x5x1,5 mm) BBO I fazinio sinchronizmo tipo kristalo monolitiniame mini rezonatoriuje. Generatoriui kaupinti naudojami antros Nd:IAG lazerio harmonikos (532 nm) 13 ns trukmės ir 7-15 mJ energijos impulsai. Erdviniai šviesos dariniai registruojami artimajame ir tolimajame laukuose. Eksperimentiškai parodoma ir teoriškai interpretuojama, kad tokio rezonatoriaus emisija gali būti kūginė ir daugiakūgė, o signalinės ir skirtuminės bangų kryptys gali būti valdomos keičiant kampą tarp rezonatoriaus optinės ašies ir kaupinimo pluošto. Taip pat parodoma, kad dryžių erdvinio šviesos darinio formavimasis gali būti pasiekiamas injektuojant pagrindinio dažnio užkrato signalą. Antrojoje disertacijos dalyje pristatomi ir tiriami plokščiųjų veidrodžių Fabri ir Pero tipo rezonatoriai su vidine lūžio rodiklio moduliacija, atitinkančia vieną fotoninio kristalo (FK) išilginį periodą. FK rezonatoriai sukurti veidrodžių paviršiuje suformuojant 2 μm, 4 μm ir 15 μm periodinę lūžio rodiklio moduliaciją (t.y. suformuojant vienmatę arba dvimatę fazinę difrakcinę gardelę). FK rezonatorių kampinis pralaidumas matuotas naudojant plataus erdvinio spektro 532 nm bangos ilgio, nuolatinės veikos lazerio pluoštą. Rezonatorių difrakcinės savybės tiriamos naudojantis skleidimo modomis ir sklaidos matricų teorija paremtais modeliais. Tyrimo rezultatai parodė, kad FK rezonatoriaus difrakcinės savybės gali būti valdomos. Išskirti du režimai: subdifrakcinis ir superdifrakcinis.